Application of the PFEM to the study of blood flows and their interactions with artery walls

Master's thesis submitted by

Jeanne Delhez

in order to obtain the degree of
Master of Science in Biomedical Engineering

Supervisor: Jean-Philippe Ponthot

Academic year 2023–2024

University of Liège

School of Engineering and Computer Science

ABSTRACT

Keywords: cardiovascular diseases, biomechanics, aneurysm, aortic valve, wall shear stress, atherosclerosis, hemodynamics, flexible artery wall, Casson fluid, Mooney-Rivlin material, fluid-structure interaction, PFEM, numerical modeling.

Cardiovascular diseases are a leading cause of mortality in Belgium and worldwide, with projections indicating a concerning rise in related deaths. Understanding the hemodynamics and biomechanical mechanisms underlying vascular failure is essential for advancing diagnostic and therapeutic strategies. In this context, computational models offer a promising tool that can really improve patient care. In particular, fluid-structure interaction algorithms have found significant applications in cardiovascular engineering, in coupling simulations of blood flows with the mechanical responses of blood vessels.

This thesis focuses on the computational modeling of the fluid-structure interaction of artery walls and blood flows as a means of assessing different biomechanical aspects. For this, the flow-structure interaction problem is addressed using a partitioned approach with a strong coupling of PFEM (for the fluid) and FEM (for the solid) models. This work relies on the PFEM3D and Metafor codes and exploits the synchronization and communication framework FSPC, all developed in the LTAS-MN2L lab of ULiège. This marks the first application of the PFEM to such biomechanical simulations.

Axisymmetric models of arteries are developed by incorporating both the Newtonian and Casson fluid models, as well as linear elastic, Neo-Hookean, and Mooney-Rivlin hyperelastic models for the deformation of blood vessels. The numerical simulations successfully describe a wide range of situations and problems, from the ejection of blood from the left ventricle and the blood flow in the healthy aortic artery to the dynamics of an abdominal aortic aneurysm and, ultimately, its rupture. The different models provide valuable insights into the corresponding dynamics and help to identify the different aspects that still need to be improved. In particular, the results explain why local defects of the artery wall must be compensated by biological remodeling processes, with the replacement of elastin by stiffer collagen, to avoid further development and rupture of an aneurysm.

Overall, this work underscores the potential of PFEM3D, Metafor, and their coupling within the FSPC framework to advance our understanding of hemodynamics and biomechanical processes, and to contribute to the improved handling of cardiovascular diseases.

RÉSUMÉ

Mots-clés : maladies cardiovasculaires, biomécanique, anévrisme, valve aortique, contrainte de cisaillement, athérosclérose, hémodynamique, paroi artérielle déformable, fluide de Casson, loi de Mooney-Rivlin, interaction fluide-structure, PFEM, modélisation numérique.

Les maladies cardiovasculaires sont l'une des principales causes de mortalité en Belgique et dans le monde, avec des projections indiquant une augmentation préoccupante des décès associés. Une bonne compréhension de l'hémodynamique et des mécanismes biomécaniques sous-jacents à l'insuffisance vasculaire est essentielle pour améliorer les stratégies de diagnostic et de traitement. Dans ce contexte, les modèles numériques offrent un outil prometteur qui peut réellement améliorer les soins apportés aux patients. En particulier, les algorithmes d'interaction fluide-structure sont largement utilisés en ingénierie cardiovasculaire, en couplant des simulations de flux sanguins avec les réponses mécaniques des vaisseaux sanguins.

Ce travail de fin d'études se concentre sur la modélisation numérique de l'interaction fluide-structure des parois des artères et des écoulements sanguins afin d'évaluer différents aspects biomécaniques. Pour ce faire, le problème d'interaction fluide-structure est abordé en utilisant une approche partitionnée avec un couplage fort des modèles PFEM (pour le fluide) et FEM (pour le solide). L'implémentation pratique est basée sur les codes PFEM3D et Metafor et exploite le cadre de synchronisation et de communication FSPC, tous développés dans le laboratoire LTAS-MN2L de l'ULiège. Ceci marque la première application de la méthode PFEM à de telles simulations biomécaniques.

Des modèles axisymétriques d'artères sont développés en incorporant à la fois les modèles de fluide newtonien et de Casson, ainsi que des modèles linéaires, Néo-Hookéen et Mooney-Rivlin hyperélastiques pour la déformation des vaisseaux sanguins. Les simulations numériques décrivent avec succès une large gamme de situations et de problèmes, depuis l'éjection du sang du ventricule gauche et l'écoulement sanguin dans l'artère aortique saine jusqu'à la dynamique d'un anévrisme de l'aorte abdominale et, finalement, sa rupture. Les différents modèles fournissent des informations précieuses sur les dynamiques correspondantes et aident à identifier les différents aspects qui doivent encore être améliorés. En particulier, les résultats expliquent pourquoi tout défaut local de la paroi artérielle doit être compensé par des processus de remodelage biologique, avec le remplacement de l'élastine par du collagène plus rigide, pour éviter le développement ultérieur et la rupture d'un anévrisme.

Dans l'ensemble, ce travail souligne le potentiel de PFEM3D, de Metafor et de leur couplage via FSPC pour faire progresser notre compréhension de l'hémodynamique et des processus biomécaniques, et ainsi contribuer à l'amélioration de la prise en charge des maladies cardiovasculaires.

ACKNOWLEDGMENTS

First of all, I would like to express my deep gratitude to Professor Jean-Philippe Ponthot, my supervisor, for giving me the opportunity to work on this project, and for his guidance and constructive feedback on my work.

I am also deeply grateful to Martin Lacroix for his availability at all times, his invaluable advice, and his detailed explanations that helped me to find my way in the simulation environment. This work would not have been possible without his patience and continuous support.

I also thank Luc Papeleux and Arnaud Radermecker, from the LTAS-MN2L lab, for their precious and highly competent inputs.

Finally, I take this opportunity to extend my thanks to my family and friends. Their help, encouragement, and love have been invaluable throughout my studies.

CONTENTS

LIST OF ACRONYMS

AAA	Abdominal aortic aneurysm
ALE	Arbitrary Lagrangian-Eulerian
CA	Cerebral aneurysm
CFD	Computational fluid dynamics
CFL	Courant-Friedrich-Levy
CGAL	Computational Geometry Algorithm Library
CT	Computed tomography
FEA	Finite element analysis
FEM	Finite element method
FSG	Fluid-solid growth
FSI	Fluid-structure interaction
FSPC	Fluid-structure partitioned coupler
IBM	Immersed boundary method
IVC	Inferior vena cava
LEP	Linear element projection
LES	Large eddy simulation
MRI	Magnetic resonance imaging
OSI	Oscillatory shear index
PFEM	Particle finite element method
PWRI	Peak wall rupture index
RBC	Red blood cell
RBF	Radial basis functions
SPH	Smoothed particle hydrodynamics
SWIG	Simplified wrapper and interface generator
T-WSS	Time-averaged wall shear stress
VHD	Valvular heart disease
WSS	Wall shear stress

INTRODUCTION

General context.

Cardiovascular diseases are a significant threat to human health. Annually, they account for 31,000 deaths in Belgium, making them the leading cause of mortality in the country. Today, nearly 754,000 Belgians suffer from a cardiovascular disease [87]. These statistics mirror global trends: in 2021, cardiovascular conditions claimed the lives of 20.5 million people worldwide, representing one-third of all deaths. Ischemic heart disease is the primary cause of premature death in 146 countries for men and 98 countries for women. The upward trend is also alarming, with projections suggesting that by 2030, cardiovascular diseases will cause over 23 million deaths globally per year [199].

Improving our understanding of the hemodynamics and biomechanical mechanisms of vascular failure is crucial to support the development of better diagnostic and therapeutic techniques for cardiovascular diseases [172]. In this context, the use of computational models holds great promise for advancing our knowledge and ultimately improving patient care [77]. Numerical models give indeed access to parameters, such as Wall Shear Stress (WSS), strain, and pulse wave velocity, that are difficult to measure directly but are critical for the assessment of the progression and diagnosis of diseases. For instance, the wall shear stress is not directly measurable in a blood vessel but is a well-known factor for the initiation and advancement of atherosclerosis and is also associated to the risk of arterial complications such as rupture [103].

In addition to enabling in silico studies that provide greater insight into underlying mechanisms, numerical models can also be used to perform patient-specific analyses with important clinical implications. When combined with advanced imaging techniques such as Computed Tomography (including CT angiography), Magnetic Resonance Imaging (MRI), three-dimensional ultrasound imaging, and 3D rotational angiography [150, 206], numerical models can be used to generate detailed three-dimensional representations of patient-specific blood vessels and their function [77, 113]. Such simulations can facilitate pre-operative planning, allowing surgeons to assess the impact of interventions on blood flow patterns and vessel mechanics. The ability to simulate patient-specific geometries and conditions has paved the way for personalized medicine, allowing clinicians to gain insight into disease progression and to develop tailored treatments for cardiovascular pathologies [17, 90].

Simulations can also guide the development and optimization of cardiovascular devices, leading to improved designs and better patient outcomes [182]. By evaluating device performance under realistic physiological conditions, simulations help refine designs and improve efficacy and safety.

Objectives.

Considering the potential of numerical simulations to shed new light on cardiovascular diseases, the current study appears as a proof-of-concept to demonstrate the relevance of the Particle Finite Element Method (PFEM) and of Fluid-Structure Interaction (FSI) modeling in this context. While the PFEM has been developed and is generally applied to hydraulic engineering or additive manufacturing, this study seeks to explore its potential application in the field of biomedical engineering. To the best of the author's knowledge, it is the first time that the PFEM is applied to the simulation of blood flows and their interactions with artery walls.

As a proof-of-concept, the following study intends not only to examine the numerical aspects of the PFEM and its use in coupled fluid-structure interaction models, but also and above all to analyze the results from a biomechanical point of view. In particular, we will address various hemodynamic problems associated with the functioning of heart valves and blood flows in arteries and veins, as well as the development and rupture of aneurysms. It is through such an analysis, based on the actual questions posed by biomechanics and medicine, that potential and limitations of the method really become apparent. In this sense, this work is intended to explore the need for new developments to make real use of the enormous potential of the method.

Outline.

Chapter 1 describes the cardiovascular system and its modeling. After an overview of two prevalent cardiovascular diseases - aneurysms and Valvular Heart Diseases (VHDs) - it explores traditional major approaches for modeling the mechanical behavior of blood vessels, blood flows, and their interactions. The chapter covers structural modeling of blood vessels using Finite Element Analysis (FEA), Computational Fluid Dynamics (CFD), and combined approaches such as fluid-structure interaction and Fluid-Solid Growth (FSG).

An overview of the fluid-structure interaction strategy followed in this study is provided in chapter 2. It includes a general introduction to the PFEM, the PFEM3D code, and the finite element code Metafor used in this work. Additionally, the chapter outlines the key features of the fluid-structure interaction algorithm FSPC (Fluid-Structure Partitioned Coupler) used to couple the fluid and solid models.

Chapter 3 encompasses a thorough discussion on blood flow modeling, including the verification of the Casson fluid model implemented as part of this work. Similarly, the chapter delves into the modeling of the arterial wall and commonly utilized constitutive laws. The initial focus lies on examining the propagation of a pressure pulse within a deformable straight artery. Subsequently, the analysis progresses to simulate realistic pulsatile flow within a deformable straight artery. This investigation considers the influence of constitutive models, fluid assumptions, and arterial stiffness on blood flow dynamics, with a particular emphasis on the critical physiological parameter of wall shear stress. A short study of the flow in the Inferior Vena Cava (IVC) demonstrates the relevance of the the Casson model in this context.

In chapter 4, a two-dimensional model of the aortic valve is presented. Following a review of state-of-the-art techniques in aortic valve modeling, the chapter extensively analyzes the flow through the aortic valve. Additionally, the impact of calcification, one of the most prevalent diseases affecting the aortic valve, is also investigated.

The simulation of an axisymmetric Abdominal Aortic Aneurysm (AAA) is considered in chapter 5. Various modeling aspects are discussed, among which the choice of the constitutive law of the aortic wall and its structure. The influence of the initial size of a fully developed aneurysm and the heterogeneity of the aneurysm wall on flow and stresses are also investigated, in partic-

ular in relation with the risk of rupture. Furthermore, the initiation and stability of developing aneurysms are investigated. Lastly, results of the explicit simulation of the rupture of aneurysms with two different geometries (a 2D Cerebral Aneurysm (CA) and an axisymmetric abdominal aortic aneurysm) are reported.

The final section presents a summary of the main achievements of this work: the implementation and verification of the Casson model in PFEM3D and the first use of the PFEM in coupled models to describe blood flows around the aortic valve, in the aortic artery, in an abdominal aortic aneurysm, and the rupture of blood vessels. The discussion ends with a description of the prospects and future work needed to progress more firmly towards the application of PFEM3D to real biomedical problems and to reap the scientific results that the PFEM has to offer.

CHAPTER 1

THE CARDIOVASCULAR SYSTEM AND ITS MODELING

1.1 The circulatory system: the basics.

The cardiovascular system comprises the heart and a complex network of blood vessels. The heart serves as a muscular pumping organ responsible for circulating blood throughout the body. Its function is crucial since the body's tissues require a constant supply of oxygen, nutrients, hormones, and other essential substances, and a continuous removal of metabolic waste products to survive. It thus plays an essential role in maintaining homeostasis and ensuring the proper functioning of various organ systems [178].

The circulatory system consists of different types of vessels with different sizes and functions: arteries, capillaries, and veins (Figure 1.1). Heart contractions drive blood flow into the major arteries emerging from the ventricles. The arteries carry oxygenated blood from the heart to different body parts. They have thick elastic walls composed of smooth muscle and connective tissue. This structural integrity enables them to withstand high blood pressure and pulsatile flow. Arteries progressively divide into smaller vessels, arterioles, which then branch into capillaries. Arterioles regulate blood flow and control blood pressure by constricting or dilating their smooth muscle walls. Capillaries are the smallest blood vessels within the circulatory system. They connect arterioles and venules. They form a network which facilitates the exchange of oxygen, nutrients, waste products, and hormones between the blood and surrounding tissues. Their small thickness makes it possible to have an efficient diffusion of substances. Venules then receive deoxygenated blood from capillaries. They also contribute to the immune response by facilitating the migration of white blood cells from the bloodstream to infected or injured tissues. Venules then merge to form larger veins, which carry deoxygenated blood from tissues and organs back to the heart. Veins have thinner walls and lower blood pressure than arteries. Veins progressively merge to form larger vessels, returning blood to the heart through the superior and inferior venae cavae, and entering the right atrium.

The heart, of course, plays a very important role in the circulatory system. It consists of four chambers (Figure 1.2): two atria and two ventricles (left and right). The rhythmic contraction (systole) and relaxation (diastole) of the heart generate the pumping action responsible for propelling blood throughout the circulatory system. Blood always flows in one direction within the heart. Deoxygenated blood enters the right atrium via the vena cava, moves to the right ventricle and is then pumped to the lungs for oxygenation via the pulmonary arteries. It circulates through the lungs where gas exchange occurs. Oxygenated blood then returns to the left atrium via the pulmonary veins, passes to the left ventricle, and is finally pumped into the systemic circulation

to feed the body's tissues. Pulmonary circulation is supplied by the right heart. It refers to the pathway of blood from the heart to the lungs and back. Systemic circulation is supplied by the left heart. It includes the vessels that transport blood to the tissues and return it to the heart.

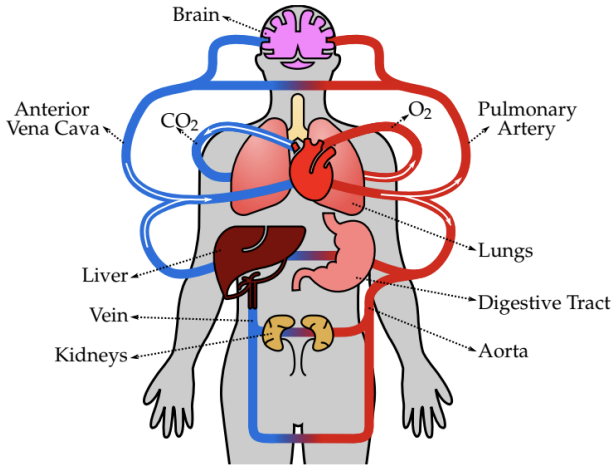

FIGURE 1.1 – Human circulatory system (reproduced from Syed et al. [173]).

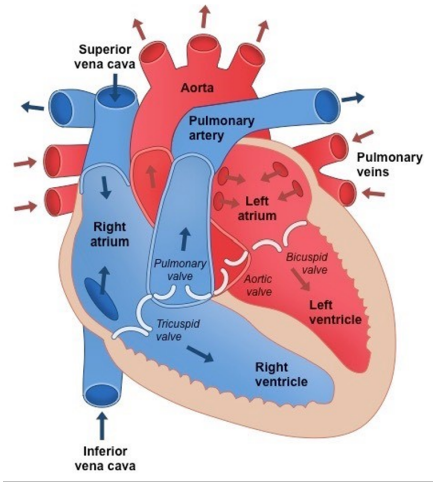

FIGURE 1.2 – Structure of the heart [15].

This unidirectional flow of blood depends on the presence of four valves that open and close according to the difference in pressure on each side of their surface. The atrioventricular valves (tricuspid and bicuspid/mitral) ensure blood flows from respectively the left and right atria to the ventricles, while the semilunar valves (aortic and pulmonary) are located at the base of the arteries leaving the ventricles. The aortic valve controls the flow from the left ventricle to the aorta (the largest artery in the body), while the pulmonary valve regulates the flow from the right ventricle to the pulmonary artery. Their function is to prevent blood from flowing back from the arteries into the ventricles. Indeed, these valves open when the ventricles contract, as the intraventricular pressure exceeds arterial pressure, and close when the ventricles relax, as the intraventricular pressure drops, thereby preventing the backward flow of blood into the heart.

1.2 Cardiovascular diseases.

Cardiovascular diseases form a group of disorders affecting the heart and blood vessels [87]. It includes

- arrhythmia: abnormal heart rhythms or heart rates,
- coronary heart diseases: affecting the blood vessels that supply the heart muscle, such as blockages,
- cerebrovascular diseases: affecting the blood vessels that supply the brain, such as blockages or narrowing,
- peripheral arterial diseases: affecting the blood vessels supplying the arms and legs, such as blockages or narrowing,
- rheumatic heart disease: affecting the heart muscle and valves and resulting from rheumatic fever caused by streptococcus bacteria,
- aortic diseases: affecting the aorta, such as aneurysms,

- congenital heart defects: malformations of the structure of the heart already present at birth,
- valvular heart diseases: affecting the heart valves,
- deep vein thrombosis and pulmonary embolism: obstruction of the veins in the legs by a blood clot that can break free and migrate to the heart or lungs,
- pericardial diseases: affecting the pericardium, the tissue surrounding the heart, such as pericarditis (inflammation) or pericardial effusion (fluid buildup within the pericardium).

These problems frequently lead to heart attacks and strokes, in which blood no longer reaches the heart or brain, with sometimes fatal results for the patient. In the following, we will concentrate on two problems that will be tackled more specifically, namely Valvular Heart Diseases (VHDs) and aneurysm rupture.

1.2.1 Valvular heart diseases.

Failure of the heart valve to open and close properly can seriously impair the heart's ability to effectively pump blood through the body. The heart will need to work harder to accomplish its vital task.

Valvular heart diseases, *i.e.,* diseases involving one or more of the heart valves, may be congenital or develop later in life. Left untreated, they can lead to stroke, heart failure, and death due to sudden cardiac arrest [147]. The aortic valve is the most susceptible to disease as it sustains the largest pressure difference. About 61% of VHD-related deaths are due to aortic valve diseases [57]. The most common congenital one is the bicuspid aortic valve disease, which occurs in 1–2% of the general population [165]. This is a common congenital heart defect in which the bicuspid aortic valve contains two leaflets instead of the usual three. This can lead to degenerative changes of the valve and is associated with dilatation of the aorta. Apart from congenital diseases, two main acquired complications can occur. Regurgitation (valve leakage) occurs when a valve loses its ability to close completely, leading to the backflow of blood. As a result, the heart's chambers have to work harder to pump the extra blood back through the valve. Aortic stenosis (valve narrowing) happens due to inadequate aortic valve opening, probably due to underlying processes such as calcification, thereby making the leaflets thicker and stiffer and obstructing blood flow out from the left ventricle. Calcium deposition changes the material properties and geometry of the leaflets, and affects their functionality during the cardiac cycle which leads to heart failure over time [97, 111].

After treatment failure with heart-healthy lifestyle changes and medicine, there are mainly two options available for solving the problem with the diseased valve: heart valve repair and heart valve replacement. Heart valve repair is often the preferred treatment when there is enough healthy tissue for reconstruction. Procedures may include fixing valve flaps, replacing cords that support the valve helping it to close properly, inserting prosthetic rings to narrow a dilated valve, ... However, in many cases of VHDs (70%), valve replacement is necessary [204]. Each year, over 290,000 patients undergo valve replacement surgeries worldwide. This number is expected to reach 850,000 by the year 2050 due to the rising average age of the population [161].

1.2.2 Aneurysms.

Arterial aneurysms are abnormal and irreversible focal dilations of arteries, typically of 50% of the physiological diameter or more [121]. This condition involves inflammation and thickening of the arterial walls, potentially leading to life-threatening complications [189]. Aneurysm complications

include rupture, hypovolemic shock (*i.e.,* a major blood loss), tissue compression, thromboembolism (*i.e.,* a blood clot causing obstruction), and ischemia (*i.e.,* a condition in which blood flow is reduced in a part of the body) [107].

In 2020, ruptured aneurysms resulted in approximately 25,000 deaths annually in the UK, Germany, and the USA combined [198]. Aneurysms can develop in different locations within the arterial system, including intracranial, aortic, abdominal, visceral, and peripheral arteries. The two most common types of aneurysms are the Abdominal Aortic Aneurysm (AAA) and the Cerebral Aneurysm (CA) [120]. AAAs and CAs combined account for over 80% of fatal aneurysm incidences.

While AAAs typically develop in the infrarenal aorta, CAs are situated in and around the circle of Willis, which provides blood to the brain and its surrounding structures. The rupture of a CA results in subarachnoid hemorrhage (a fatal condition in the circle of Willis) with a mortality rate of 45% [80]. Conversely, an AAA rupture leads to internal bleeding with mortality rates ranging from 65% to 80% [86]. Additionally, apart from their distinct locations, most AAAs exhibit a fusiform shape, while over 90% of CAs present a saccular (spherical or berry-like) morphology (Figure 1.3).

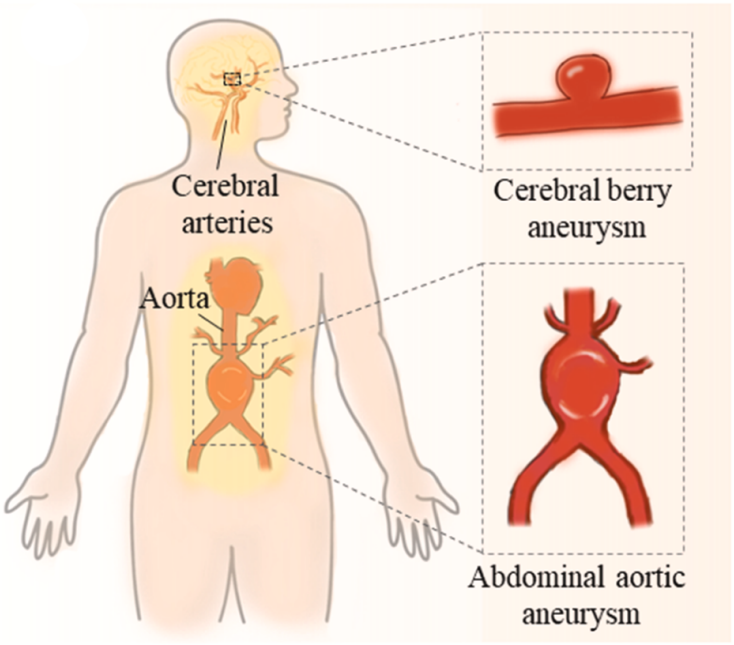

FIGURE 1.3 – Two most common aneurysms (reproduced from Sun et al. [172]).

The formation and growth of an aneurysm is a long-term process, sometimes taking years. An aneurysm is often detected by medical imaging and is usually asymptomatic until it ruptures [80]. An aneurysm occurs because of weakness of the vessel wall, an abnormality in the artery wall, or an acquired disease. Few aneurysms are the direct result of specific causes such as trauma, acute infection, inflammatory diseases, and connective tissue disorders (*e.g.,* Marfan syndrome). Therefore, the majority of aneurysms are considered non-specific [149]. Aneurysms are traditionally considered as a consequence of atherosclerosis [142, 149]. Indeed, sediments such as fatty deposits can cause blockage of the arteries and create an abnormality in the artery wall.

While surgical or endovascular procedures are available for patient treatment, they are invasive and carry inherent risks [107]. These risks must therefore be compared with the risk of rupture. To date, aneurysm diameter and expansion rates have served as the primary metrics for

evaluating the risk of rupture [57, 121]. However, this approach is clearly insufficient: many small aneurysms rupture and some large or rapidly growing ones may not require surgical intervention [38]. Computational models assessing aneurysm hemodynamics may aid in identifying more accurate predictors of vessel rupture or thrombosis formation, facilitating better determination of when clinical intervention is required.

1.3 The different modeling components.

Due to the multitude of processes involved, realistic modeling of blood flows and their interactions with vessels is a complex task that usually requires a combination of different approaches adapted from different scientific and technical fields [57]. Modeling the mechanical behavior of veins and arteries is based on techniques developed in the field of structural engineering. Blood flow modeling uses Computational Fluid Dynamics (CFD) approaches. These two aspects must then be combined to describe the interplay between the vessels and the flow, using appropriate Fluid-Structure Interaction (FSI) methods. Taking into account biomechanical processes also requires the development of original approaches that integrate the specific behavior of living materials by means of appropriate constitutive laws and empirical models.

1.3.1 Structural modeling of blood vessels.

Finite Element Analysis (FEA) is, by far, the most popular way for simulating the mechanical deformation of the walls of blood vessels and the corresponding internal stresses [162, 167, 200].

Based on the geometric reconstructions and equations describing the wall stress-strain relationship, FEA calculations can be used, for instance, to determine the circumferential stress across an aneurysm wall at peak systolic pressure and determine the risk of aneurysm rupture. Studies have shown that this peak wall stress has a higher sensitivity and specificity in predicting rupture risk than other parameters [52]. The Finite Element Method (FEM) can also be used to simulate the interaction between an inflated balloon catheter and a plaque deposit on a blood vessel wall [78].

The deformation of blood vessel walls plays an important role in the dynamics of the circulatory system. The opening and closing of heart valves involve large deformations of the corresponding tissues. During systole, the aorta also deforms elastically to provide a temporary reservoir for about 70% of the blood injected with the heartbeat [20]. The development and rupture of aneurysms are also characterized by large deformations of the vessels in which they develop. The accurate modeling of these phenomena requires therefore appropriate numerical techniques accounting for such large deformations and the associated geometrical nonlinearities. In this context, purely Lagrangian implementations of the finite element method, in which the nodes of the calculation mesh follow the movement of the underlying material, are inappropriate. The rapid deterioration of the mesh must be compensated for by frequent and costly remeshing operations.

Due to their large deformations, the Arbitrary Lagrangian-Eulerian (ALE) formulation is often presented as the most suitable approach for the modeling of biological soft tissues [159]. This approach involves either moving the nodes of the computational mesh with the continuum in a normal Lagrangian fashion, keeping them fixed in an Eulerian fashion, or moving them in an arbitrarily specified fashion to provide a continuous rezoning capability. Because of this freedom, greater distortions of the continuum can be handled than would be allowed by a purely Lagrangian method, with greater resolution than that afforded by a purely Eulerian approach [44].

1.3.2 Computational fluid dynamics.

The mechanical models of blood vessel walls can be used, with an appropriate constitutive law, to estimate their deformation and the risk of rupture. However, the pressure and Wall Shear Stress (WSS) are determined by the flow in the artery [57]. In recent years, CFD has therefore emerged as a complementary tool to describe and understand the biomechanical behavior of blood flows in both normal and diseased vessels [129]. In particular, CFD models are commonly used to compute the wall shear stress, which is an important indicator for aneurysm rupture, thrombus formation, and prediction of disease progress [203].

The finite difference method is not suitable for describing the complex geometries encountered in hemodynamics, so most studies of the flow in the arterial system use a finite volume or finite element approach [108]. Commercial and open-source CFD software using one or the other approach are available and have been extensively used for various research projects [42, 91, 109, 152, 187, 207].

Eulerian formalism is widely used in CFD. In such a formulation, the nodes remain fixed in space and the continuum is allowed to flow through the mesh, leading to convective effects. While such algorithms simplify the treatment of complex material motion, they present numerical challenges due to the non-symmetric nature of the convection operators and cannot easily cope with the moving boundaries typical of problems with fluid-structure interactions, hence the preference for Lagrangian/ALE approaches and Immersed Boundary Methods (IBMs) [104] that allow interfaces (and free surfaces) to be easily tracked.

More recently, meshless methods have emerged as a valuable alternative. Instead of relying on a grid, these methods use a set of scattered data points or particles to represent the geometry and solve the governing equations [77]. Meshless methods have many advantages in that they can handle large deformations and complex geometries without remeshing [106]. They also have the ability to model damage to blood vessels (compared to mesh-based models which struggle to simulate arterial damage) [77].

In the Smoothed Particle Hydrodynamics (SPH) method, all the properties of the fluid (velocity, density, ...) are attached to particles distributed throughout the domain [7]. The interaction between the particles is described using a smoothing kernel to solve the fluid equations. Due to its ability to model large deformations, SPH finds applications not only in arterial hemodynamics but also in more complex flows [18, 184]. For instance, this approach has been successively applied to study the flow in the heart cavity [157] and around the heart valves [158].

The SPH method appears attractive and versatile but suffers from consistency and stability problems [12, 124]. Therefore, in this work, we explore the application of the Particle Finite Element Method (PFEM) as an alternative method. To the best of our knowledge, the PFEM has never been applied to the modeling of blood flows, although very promising results have been reported for the simulation of free surface flows [35, 56, 102], geotechnical applications [208], and fluid-structure interaction [88]. In essence, the PFEM is a particle method because all the properties of the flow are attached to the particles. However, the governing equations are integrated on a mesh using the classical FEM in a purely Lagrangian manner. This provides both the flexibility of meshless methods and the robustness of the finite element method. A detailed description is left to section 2.1.

1.3.3 Fluid-structure interaction.

Mechanical models of the vessel walls and CFD models of the flow naturally provide complementary views of the dynamics of the arterial system. In reality, these two aspects are intimately

linked and must be considered simultaneously using appropriate fluid-structure interaction algorithms. These algorithms allow the simulation of blood flows to be coupled with the mechanical behavior of blood vessels, taking into account the interactions between fluid dynamics and the structural integrity and elasticity of the modeled vessel walls, heart walls, or valves [77]. Such interactions are crucial, for example, for the realistic modeling of the propagation of pressure waves through the cardiovascular system, since the speed of propagation depends critically on the dilatation of the vessels. The interaction between the hemodynamics of the blood flow and the stress and deformation of the solid structure is also of great importance for the prediction of rupture of aneurysms [21].

FSI simulations involve solving a set of coupled partial differential equations describing both the fluid flow and the structural mechanics equations [104]. Different approaches are available.

On the one hand, the monolithic approach involves the simultaneous solution of the equations for both media within a single computational framework [28]. The structural and fluid domains are meshed and generic equations describing both dynamics are solved within the same mathematical framework. This approach provides accurate and robust predictions, but can be computationally intensive because the mathematical and numerical framework must be generic enough to describe the dynamics of both the elastic solid and the fluid. On the other hand, partitioned approaches treat the fluid and structural domains as independent, each with its own mesh, set of governing equations, and dedicated solver. Each solver operates independently, exchanging information through an interface at each time step. This approach requires an efficient communication and synchronization interface, but is interesting because the dedicated solvers can exploit the specificities of the fluid and structural problems and implement detailed physics [197].

A further distinction of partitioned approaches can be made between one-way and two-way coupling strategies. In one-way coupling, also referred to as loose coupling, the results of the CFD simulations are used to estimate the loading to be applied to the solid (through the boundary conditions) and to calculate its deformation. The exchange of information between the fluid and structural domains is one-way, with the fluid driving the structural response. In cardiovascular models, vessel compliance and distension are often investigated using one-way FSI. The fluid flow is first solved using CFD to determine the pressure and shear stress at the vessel wall, and these results are then used to calculate the wall deformation. While this approach is computationally efficient, it assumes that structural deformation has a negligible effect on the fluid flow [98].

Two-way FSI, or fully coupled models, treat the fluid and structure as coupled systems that interact in both directions, allowing the full mutual influence between the two domains to be taken into account. Fluid forces affect the deformation of the structure, and the resulting deformation changes the fluid flow patterns. FSI simulations require appropriate conditions at the interface between the simulated blood flow and the solid structure, ensuring compatibility of fluid and wall displacement and equilibrium of traction [57]. The bidirectional exchange of information allows a more accurate representation of the fluid-structure interaction [5]. Fully coupled FSI simulations are typically unsteady. They are also computationally more demanding than loosely coupled studies as an iterative procedure between the fluid and solid solvers is often required to reach an equilibrium at each time step. Given the significant dynamic and elastic behavior of the cardiovascular system, particularly in the heart, two-way studies are more appropriate when a transient solution is clinically relevant.

When dealing with two-way coupled models, it is often necessary to consider the so-called *added mass effect*. This phenomenon occurs when the fluid and the structure have comparable inertia or densities. When the structure deforms, its apparent inertia is greater than that of the solid itself because the deformation of the latter displaces the fluid, increasing the mass that must

be accelerated or decelerated [83]. This phenomenon is relevant to cardiovascular biomechanics when elastic arteries interact with blood [77]. The added mass effect is challenging as it adversely affects the convergence of fluid and solid variables at their common boundary [183] and may lead to non-convergence of the iterative solution.

Most CFD and structural models used in FSI simulations rely on a Lagrangian or Arbitrary Lagrangian-Eulerian approach to ensure that the meshes of the two models follow the displacement of the common boundary between the solid and fluid subdomains.

The Lagrangian and ALE approaches use body-fitted meshes of flow and structure where the boundaries and interfaces are explicitly represented by element edges (in 2D) or faces (in 3D). The IBM provides a completely different approach with overlapping fluid and structure components whose (moving) interface does not coincide with the mesh [96]. The interface is not explicitly modeled, but is introduced by an additional force term in the momentum budget. A major advantage of the immersed boundary method is the representation of the equations on a fixed Cartesian grid, which allows easy grid generation [92, 182]. The IBM was first introduced to study flow patterns around heart valves [134] and is still used to simulate fluid-structure interactions involving flexible structures such as heart valves or blood vessel walls [92]. However, the highly localized forces that account for the presence of interfaces are very difficult to define and to express in an appropriate mathematical formulation.

1.3.4 Fluid-solid growth.

The flow and solid models describe the mechanical behavior of blood and arteries in much the same way that coupled simulations can address the dynamics of a rotor blade or a glider. However, when dealing with living material, there is more to be done to account for the effects of flow and mechanical stresses on the tissue. In their multiscale modeling of intracranial saccular and abdominal aortic aneurysms, Humphrey and Taylor [86] paved the way for such an extended approach by integrating not only the interaction between global hemodynamics and local wall stress through FSI, but also the effects of molecular biochemical reactions through growth and remodeling. They coined the term Fluid-Solid Growth (FSG) model, where "growth" refers to changes in the size of the aneurysm and "remodeling" refers to changes in its structure [85]. While FSI calculations capture the state of the aneurysm over a cardiac cycle, the growth and remodeling components operate on a longer timescale, ranging from weeks to years, to simulate the evolution of the aneurysm. In an iterative process, wall stress values obtained from FSI calculations serve as input to the growth and remodeling simulation, which links them to long-term wall deformations through mechanobiological processes [85]. The resulting long-term wall deformation influences fluid flow and structural behavior, which is then fed back into the FSI simulation for the next iteration. By incorporating the influence of hemodynamics, structural properties, and biochemical behavior of the aneurysm wall, FSG models represent a highly realistic and sophisticated deterministic modeling approach. They could theoretically simulate the individual evolution of an aneurysm from its initial imaging stage to a final state and predict whether it will remain stable or lead to rupture.

Mechanobiological models aim at understanding how biological cells respond to mechanical stimuli. When studying the response of arterial wall tissue, wall shear stress and wall pressure are critical because they play a key role in driving elastin degradation and collagen synthesis. Low WSS drives elastin degradation, resulting in reduced wall distensibility and increased wall pressure. To counteract this effect, collagen is synthesized to stabilize the aneurysm, ultimately driving aneurysm growth [196].

While the concept of fluid-solid growth models and their potential implications are very promising, their practical use as a tool for predicting rupture risk in a clinical setting remains distant. Current FSG models rely on a wide range of assumptions, and their experimental validation is challenging and currently rather limited [57]. A major limitation of this approach is related to the lack of appropriate modeling of the influence of smooth muscle cell behavior [66]. The biochemical mechanisms involved in these processes are also not fully understood, which hinders the development of reliable models. To date, no FSG model accounts for the possibility of rupture.

1.3.5 Challenges in computational modeling.

Despite their potential, FSI computational algorithms face several challenges and limitations. A realistic representation of both the fluid and structural domains, which requires high-fidelity imaging data and detailed constitutive models for vessel walls, is necessary for accurate and efficient modeling of fluid-structure interactions. Solving the coupled equations is also computationally demanding, especially for large-scale simulations and real-time clinical applications. In addition, it is crucial to validate FSI models against in vitro experiments or clinical data to ensure their reliability and to adapt them accordingly to better reflect physiological processes [77].

The intricate nature of the circulatory system, characterized by its pulsatile dynamics, multiscale interactions, and interplay with other organs, introduces additional challenges to accurately model physiological behavior [48].

Blood and blood vessels exhibit rather complex mechanical behaviors [58], requiring elaborate constitutive material models that can be challenging to formulate and validate. On the one hand, blood is typically a non-Newtonian fluid. Its non-Newtonian properties are influenced by numerous factors, including blood composition (especially red blood cell content), ambient temperature, and vessel size. On the other hand, the mechanical behavior of blood vessels is even more complex, in part due to their hierarchical structures spanning multiple scales, from microscale fiber-reinforced configurations to macroscale multilayered arrangements. The anisotropy and nonlinear behavior of biological tissues can also depend on the patient's physiology, the location and type of vasculature, and the disease state. The interactions between biological, chemical, mechanical, and physical factors further complicate the modeling of blood vessels [171]. As a result, accurate representation of blood flows, vascular mechanical responses, and their interactions poses significant challenges.

CHAPTER 2

FLUID-STRUCTURE INTERACTION

While the previous chapter provides a review of the usual approaches for modeling blood flows and their interactions with blood vessels, this master's thesis focuses on one of these methods, namely the Particle Finite Element Method (PFEM). A detailed description of the method and of its particular implementation PFEM3D used in this study can be found in, respectively, Cremonesi et al. [34] and Cerquaglia's PhD thesis [27]. Here, we only offer a general introduction to the method. Additionally, this chapter presents a brief introduction to the finite element code Metafor, along with an outline of the fluid-structure algorithm FSPC utilized to couple the fluid and solid models. All the different codes have been developed in the LTAS-MN2L lab of the University of Liège.

2.1 The Particle Finite Element Method (PFEM).

The PFEM can be applied to a wide variety of multiphysics problems. Here we consider its application to the solution of the Navier-Stokes equations, written as

$$\frac{D\rho}{Dt} + \rho\nabla \cdot \mathbf{v} = 0 \qquad \text{in } \Omega_f(t)\times]0,T] \tag{2.1}$$

$$\rho\frac{D\mathbf{v}}{Dt} = \rho\mathbf{b} - \nabla p + \nabla \cdot \boldsymbol{\tau} \qquad \text{in } \Omega_f(t)\times]0,T] \tag{2.2}$$

where ρ and $\mathbf{v}$ are the fluid density and its velocity, respectively, p is the pressure, $\boldsymbol{\tau}$ is the viscous stress tensor (deviatoric part of the Cauchy stress tensor), and $\mathbf{b}$ is the body force per unit mass. The above equations must be solved in the fluid domain $\Omega_f(t)$, which can change with time t due to elastic deformation of the vessel walls or, in another context, due to motion of the free surface of the fluid.

The above equations (2.1)-(2.2) are applicable to compressible flows. Since blood is generally considered to be incompressible, the mass conservation simplifies into

$$\nabla \cdot \mathbf{v} = 0 \tag{2.3}$$

Note however that the compressible form of the continuity equation is sometimes used even if the fluid is assumed incompressible. This allows for the efficient numerical modeling of the flow using the so-called weakly compressible approximation. A popular approach in this context is to resort to the Tait-Murnaghan state equation

$$p = \frac{K_0}{K_0'}\left[\left(\frac{\rho}{\rho_0}\right)^{K_0'} - 1\right] \tag{2.4}$$

where ρ_0 is a reference density and where K_0 and K_0' are appropriate constants describing a linear dependency of the bulk modulus with pressure [110].

For a generalized Newtonian fluid, the viscous stress tensor is related to the deviatoric strain rate tensor

$$\mathbf{D} = \frac{1}{2}(\nabla \mathbf{v} + \nabla^{\mathrm{T}} \mathbf{v}) \tag{2.5}$$

by means of

$$\boldsymbol{\tau} = 2\mu(\mathbf{D})\mathbf{D} \tag{2.6}$$

where the viscosity μ is allowed to depend on the strain rate. The viscosity is a constant if the fluid is truly Newtonian.

2.1.1 Spatial discretization of the fluid domain and boundaries identification.

In the PFEM, the continuum is initially discretized using a set of points, referred to as particles, which carry all the mathematical and physical information about the fluid. In that sense, the PFEM can be considered as a particle method [89].

Unlike Smoothed Particle Hydrodynamics (SPH), where the interaction between particles is modeled without reference to any underlying mesh [7], the PFEM relies on a finite element mesh to evaluate the forces acting on each particle and to discretize and solve the differential problem. While the classical Finite Element Method (FEM) makes use of different element types, the PFEM mesh is composed only of triangles (in 2D) or tetrahedra (in 3D) built on the set of particles. Such a mesh can be generated in an efficient way using any Delaunay triangulation algorithm [62].

The resulting mesh produced by the Delaunay triangulation suffers from an important shortcoming as it covers the entire convex hull of the particle cloud and only this region (Figure 2.1). The method must therefore be adapted to deal with non-convex fluid domains or fluid domains that are not connected. This issue is particularly significant for free-surface flows in which patches and droplets of fluid detach from the main fluid body. Enhancements are therefore required both to delete the non-physical elements produced by the triangulation algorithm and to identify the actual boundary of the fluid domain.

This problem of identifying the fluid domain boundary is typical of the PFEM approach. It does not exist in conventional finite element modeling, as the procedure is reversed here. In finite element discretization, the domain contour is provided by the geometric modeling and the domain is decomposed into finite elements using different strategies. The set of mesh nodes is then the product of the discretization. In the PFEM approach, on the other hand, everything starts with the particles. The mesh, the current fluid domain $\Omega(t)$, and its boundaries $\Gamma(t) = \partial\Omega(t)$ must be derived from the spatial distribution of the particles.

The identification of the boundary of the fluid domain is typically done using the α-shape technique [47]. This approach can be implemented in different ways but the basic idea is to discard those elements that are too distorted or too large. This strategy is motivated by the observation that spurious elements are usually much more elongated than those that are inside the fluid domain. In the PFEM code used in this project (PFEM3D), the application of the α-shape technique relies on the particular implementation available through the Computational Geometry Algorithm Library (CGAL) [177]. A given element is removed from the mesh if the radius r_{circum} of its circumcircle or circumsphere exceeds some multiple α of the characteristic mesh size h, *i.e.,* if

$$r_{circum} > \alpha h \tag{2.7}$$

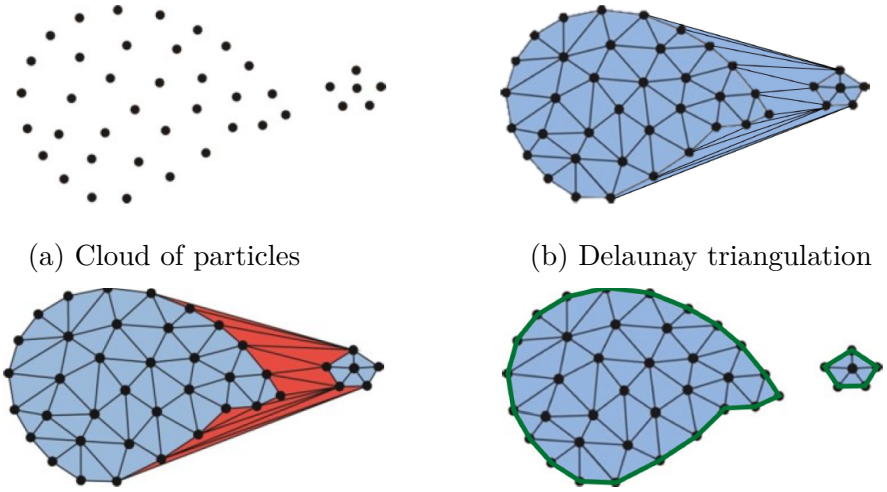

(a) Cloud of particles

(b) Delaunay triangulation

(c) Wrong (excessively distorded) triangles are detected (in red)

(d) Boundaries are identified (in green)

FIGURE 2.1 – Spatial discretization of a disconnected 2D domain (adapted from Cerquaglia's PhD thesis [27]).

The value of the α parameter must be determined empirically. A value that is too small will artificially create holes in the fluid domain, whereas a large value will artificially link separate subdomains.

Figure 2.1, reproduced from Cerquaglia's PhD thesis [27], shows the whole procedure of discretization of a 2D fluid domain by a cloud of particles (a), the Delaunay triangulation (b), the application of the α-shape algorithm to discard non-physical elements (c), and the identification of the boundaries (d).

2.1.2 Galerkin weak solution.

The adapted Delaunay tessellation defines the mesh on which a standard Galerkin approach can be applied to solve the differential problem (2.1)-(2.2).

The different steps are identical to the classical finite element approach. First, weak forms of (2.1) and (2.2) equations are obtained by multiplying the Navier-Stokes equations by appropriate test functions and integrating over the fluid domain. Then, linear isoparametric finite element discretizations are introduced for both velocity and pressure so that the state variables of the discretized problems are the vectors v and p of the velocity and pressure at the nodes of the mesh, *i.e.,* of the particles. This leads to semi-discrete equations of the form (see Fevrier's thesis [60] for the detailed derivation of these equations)

$$\mathsf{D}_{op}\mathsf{v} = \mathsf{0} \tag{2.8}$$

$$\mathsf{M}\dot{\mathsf{v}} + \mathsf{K}\mathsf{v} + \mathsf{D}_{op}^{\mathrm{T}}\mathsf{p} = \mathsf{f}_{ext} \tag{2.9}$$

where M is the mass matrix, K accounts for the viscosity of the fluid, D_{op} is the discretized divergence operator, and f_{ext} is the vector of body forces and boundary conditions.

The use of linear interpolation for both velocity and pressure is known to be prone to instabilities as it violates the Ladyzhenskaya-Babuška-Brezzi condition [43]. The above approach

must therefore be supplemented with appropriate stabilization procedures. To this end, a Petrov-Galerkin pressure stabilization procedure is introduced [84]: some multiple of the residual of the momentum equation is introduced into the mass conservation equation [176].

2.1.3 Mesh update.

The above semi-discrete equations (2.8)-(2.9) can be integrated forward in time using either an explicit or an implicit method. Usually, an implicit first-order backward Euler scheme is used to avoid the stability constraint set by the Courant-Friedrich-Levy (CFL) condition. In the weakly compressible case, efficient explicit integration schemes are allowed, which can be very appealing for fast dynamics problems and nonlinear problems that may suffer from numerical issues of convergence [34]. This approach is not feasible in the incompressible case since the continuity equation does not contain any time derivative in (2.8).

Equations (2.8) and (2.9) are expressed in a Lagrangian form, which explains why the convective terms do not appear. This approach provides a great simplification since the complex nonlinear nature of these terms does not need to be handled. This, however, relies on the understanding that the nodal variables v and p are attached to the particles moving with the flow. To advance the solution forward in time, it is therefore necessary to update the position of the nodes (or particles) according to

$$\mathsf{x}_{n+1} = \mathsf{x}_n + \Delta t\, \mathsf{v}_{n+1} \tag{2.10}$$

where x_n and v_n denote the vectors of position and velocity of the different particles at the n-th time step and Δt is the length of the time step.

The Lagrangian nature of the semi-discrete equations and the simplification of the convective terms come however at the expense of some nonlinear difficulties. Since the various matrices involved in the semi-discrete equations depend on the position of the particles, and since these positions are part of the unknowns of the problem, the evaluation of these matrices at time $n+1$ within the framework of an implicit discretization leads to a system of nonlinear equations that must be solved by an iterative method. A few Picard iterations are usually enough to reach convergence and advance the solution. Alternatively, a Newton-Raphson algorithm can be used.

The movement of nodes from one time step to the next naturally leads to mesh distortions. Remeshing may therefore be necessary to ensure the quality of the solution. While the continuous deterioration of the mesh cannot be avoided when the fluid starts to flow, the PFEM method offers however two advantages in this respect. The first is that a complete new mesh does not need to be introduced: the nodes of the old mesh are retained and it is therefore sufficient to implement a new Delaunay triangulation procedure starting from these nodes. The second advantage comes from the use of linear basis functions. With this type of interpolation, the complete solution is entirely determined by the nodal values, *i.e.*, the velocity, pressure, and density of the particles located at the mesh nodes. Since the nodes are preserved in the case of remeshing, the solution does not need to be projected onto the new mesh. A simple application of Delaunay triangulation algorithm (with α-shape) therefore enables fast and efficient remeshing. It should be noted, however, that remeshing may involve more complex operations if the PFEM is used to solve solid problems and element information stored at Gauss points must be transferred from the old mesh to the new one [34].

The application of Delaunay triangulation, enhanced by the α-shape technique, allows to account for the detachment and reattachment of fluid patches in a completely natural and transparent way. When the movement of a fluid particle or a group of fluid particles causes them to move significantly apart from the main body, the triangular elements connecting them to the main body of the fluid become highly deformed and are automatically removed by the α-shape

technique. As a result, the particles are separated from the main body. Conversely, when fluid patches initially separated from each other move closer, the elements created by Delaunay triangulation appear between them and, if the particles are close enough, are maintained in the system after the α-shape algorithm has been applied. In this way, the connectivity of the different parts of the fluid domain is automatically adapted to the physics of the flow.

It should be noted, however, that this procedure does not preserve the total mass of the fluid, since fluid elements are added or removed without any real control of the mass balance. It is however not an issue in the open system considered in this work.

Even if it can be performed efficiently, remeshing can significantly increase the computation time, especially in 3D simulations. Rather than implementing a mesh update at each time step, it may therefore be advisable to implement a strategy that leads to updating the mesh only when a certain measure of mesh distortion is exceeded.

From time to time, the simple call to a new Delaunay triangulation is not sufficient to ensure the quality of the mesh. It can indeed happen that, as a result of the flow, the particles concentrate too much in some regions while other regions are described by too few particles. In these cases, it is necessary to remove particles or add new ones to get an accurate solution. This local remeshing is controlled with two empirical parameters γ and ω that are, respectively, associated with the suppression of particles in regions where they are too close to each other and with the addition of new particles where the mesh is too coarse [50].

2.2 Metafor.

The accurate modeling of the large deformations of blood vessels and tissues ask for appropriate numerical techniques accounting for the corresponding nonlinear processes. Metafor, the finite element code developed at the LTAS-MN2L laboratory of the University of Liège, meets this requirement and is used in this project [135]. It is an object-oriented finite element code for the simulation of solids submitted to large deformations using an Updated Lagrangian or an Arbitrary Lagrangian-Eulerian (ALE) formalism [135, 136]. Different material laws are implemented to describe different physics (elasticity, elasto-plasticity, elasto-visco-plasticity, ...).

At any given time t, Metafor solves discrete versions of the momentum and mass conservation equations (the Cauchy momentum equations)

$$\rho \frac{D^2\mathbf{x}}{Dt^2} - \nabla \cdot \boldsymbol{\sigma} = \rho \mathbf{b} \qquad \text{in } \Omega_s(t) \times]0, T] \tag{2.11}$$

$$\rho J = \rho_0 \qquad \text{in } \Omega_s(t) \times]0, T] \tag{2.12}$$

where $\Omega_s(t)$ is the volume occupied by the solid in the current configuration, $\mathbf{x}$ is the current position of the material particles, $\rho(\mathbf{x}, t)$ and $\rho_0(\mathbf{X}, t)$ are the densities in the current and reference configurations respectively, J is the Jacobian of the transformation (*i.e.,* the determinant of the deformation gradient tensor), $\boldsymbol{\sigma}(\mathbf{x}, t)$ is the Cauchy stress tensor, and $\rho\mathbf{b}(\mathbf{x}, t)$ are the body forces.

Metafor uses a discretization of the Principle of Virtual Work on the deformed configuration. This leads to the semi-discrete equations

$$\mathsf{M}_s \mathsf{a} + \mathsf{f}_{int} = \mathsf{f}_{ext} \tag{2.13}$$

$$\mathsf{M}_s = \mathsf{M}_s^0 \tag{2.14}$$

where a is the nodal accelerations vector, M_s is the mass matrix, and f_{int} and f_{ext} are the vectors of internal and external forces, respectively. The discretized mass conservation equation (2.14) is automatically satisfied since the mass matrix remains constant during the simulation.

On account of the dependency of both the internal forces f_{int} and external forces f_{ext} on the displacement field, the system (2.13)-(2.14) is nonlinear. It is solved using a Newton-Raphson strategy as

$$\mathsf{M}_s\mathsf{a} + \mathsf{K}_t(\mathsf{x}^k)\Delta\mathsf{x}^k = \mathsf{f}_{ext} - \mathsf{f}_{int}(\mathsf{x}^k) \tag{2.15}$$

$$\mathsf{x}^{k+1} = \mathsf{x}^k + \Delta\mathsf{x}^k \tag{2.16}$$

where

$$\mathsf{K}_t(\mathsf{x}^k) = \frac{\partial \mathsf{f}_{int}}{\partial \mathsf{x}}(\mathsf{x}^k) \tag{2.17}$$

is the (consistent) tangent stiffness matrix.

Time integration is performed with the Generalized-α method. The system of equations is treated implicitly and solved using a predictor/corrector scheme based on the Newton-Raphson algorithm.

2.3 FSI coupling through FSPC.

In this project, the flow-structure interaction problem is addressed through a partitioned approach with the strong coupling of the PFEM and FEM models described in the previous section. The practical implementation uses the synchronization and communication framework FSPC based on CUPyDO, a flexible and versatile tool for coupling independent fluid and solid solvers [179]. FSPC stands for Fluid-Structure Partitioned Coupler.

A subdomain partitioned coupling strategy is used in which the governing equations of the fluid and solid are solved separately in the corresponding domains $\Omega_f(t)$ and $\Omega_s(t)$. The two domains are considered as separate entities but share a common interface, $\Gamma(t)$, at which the interaction occurs. FSPC exploits the Dirichlet-Neumann paradigm: the displacements/velocities at the solid-fluid interface resulting from the solution over the solid domain are used as Dirichlet boundary conditions for the fluid domain while the surface tractions on $\Gamma(t)$ computed by solving the fluid problem are prescribed, as Neumann boundary conditions, to the solid. Mathematically, the coupling conditions at the fluid-solid interface are defined by the continuity of the displacements and surface tractions at the interface, *i.e.,*

$$\mathbf{u}_f^\Gamma = \mathbf{u}_s^\Gamma \tag{2.18}$$

$$\mathbf{t}_f^\Gamma = -\mathbf{t}_s^\Gamma \tag{2.19}$$

where $\mathbf{u}_f^\Gamma$ and $\mathbf{u}_s^\Gamma$ are the displacement field at the interface between the fluid and solid domains, respectively, where the surface tractions on the fluid side are given by $\mathbf{t}_f^\Gamma = (-p\mathbf{I} + \boldsymbol{\tau}) \cdot \mathbf{n}_f$, and where $\mathbf{t}_s^\Gamma = \boldsymbol{\sigma} \cdot \mathbf{n}_s$ denotes the corresponding surface tractions on the solid. The normal unit vectors $\mathbf{n}_f$ and $\mathbf{n}_s$ are both pointing outwards from their respective domains so that, for a smooth interface, $\mathbf{n}_f = -\mathbf{n}_s$.

In practice, since the PFEM and FEM solvers are independent, the fluid and solid problems are solved in a staggered way and iterations are required to meet the coupling conditions (2.18)-(2.19). Also, the different fields are not exchanged as continuous functions of space but only through the nodal values of their finite element discretization. Therefore, the fluid and solid fields must be interpolated from nodal values. The whole process can then be decomposed into four steps as follows.

- The nodal positions of the solid at the interface u_s^Γ are interpolated in space to compute the corresponding positions at the nodes of the fluid domain,

$$\mathsf{u}_f^\Gamma = \mathsf{H}_{SF}\mathsf{u}_s^\Gamma \tag{2.20}$$

where H_{SF} is the solid-to-fluid interpolation matrix. When the solid and fluid meshes are conformal at the fluid-structure interface, each interface node viewed by the solid solver has its equivalent on the fluid side and the meshes are said to be matching. In this case, H_{SF} is the identity matrix (or a permutation matrix if the interface nodes are not ordered in the same way on the solid and fluid sides). However, in many situations, one may want to use different levels of mesh refinement and an interpolation technique is required to transfer the nodal data from one solver to another. For instance, the so-called Radial Basis Functions (RBF) and K-Nearest Neighbours are commonly found in the literature [101].

- The surface traction on the interface are obtained from the solution of the fluid problem under the prescribed displacement field (2.20), *i.e.,*

$$\mathsf{t}_f^\Gamma = \mathcal{F}(\mathsf{u}_f^\Gamma) \tag{2.21}$$

  where $\mathcal{F}$ denotes the general nonlinear Dirichlet operator associated to the fluid solver.

- These results are then projected on the solid discretization using an appropriate fluid-to-solid interpolation matrix nodal H_{FS}, which can be expressed as

$$\mathsf{t}_s^\Gamma = \mathsf{H}_{FS}\mathsf{t}_f^\Gamma \tag{2.22}$$

- The solution of the solid problem under this loading provides the new estimate of the position of the interface

$$\mathsf{u}_s^\Gamma = \mathcal{S}(\mathsf{t}_s^\Gamma) \tag{2.23}$$

  where $\mathcal{S}$ is the general nonlinear Neumann operator associated to the solid solver.

Combining the above four steps, the coupling conditions (2.18)-(2.19) can be reformulated as a fixed-point problem

$$\mathsf{u}_s^\Gamma = \mathcal{S}\left(\mathsf{H}_{FS}\mathcal{F}(\mathsf{H}_{SF}\mathsf{u}_s^\Gamma)\right) \tag{2.24}$$

or

$$\mathsf{u}_s^\Gamma = \mathcal{T}(\mathsf{u}_s^\Gamma) \tag{2.25}$$

where $\mathcal{T}$ is a global nonlinear transfer operator combining the interpolation matrices and the fluid and solid solver operators.

Alternatively, the interaction problem could be expressed in terms of any of the fluid or solid variables. In practice, the fixed-point problem is condensed on the solid side, since the number of degrees of freedom of the solid interface is usually much smaller than the number of degrees of freedom of the fluid interface.

In practice, the fixed-point problem (2.25) is solved iteratively, *i.e.*, a first guess of u_s^Γ is used to compute the fluid solution, which allows the computation of surface tractions to be prescribed to the solid. When injected in the solid problem, these provide a new estimate $\hat{\mathsf{u}}_s^\Gamma$ of the nodal displacements. The procedure is repeated until $\mathsf{u}_s^\Gamma = \hat{\mathsf{u}}_s^\Gamma$.

Many different iterative algorithms are available to solve the nonlinear fixed-point problem (2.25). A block Gauss-Seidel method with dynamic under-relaxation, a Quasi-Newton algorithm with inverse least-square, and a multi-vector Jacobian approach are for instance available in FSPC, as detailed in Appendix A.

In terms of computer implementation, FSPC uses a high-level approach in which the fluid and solid solvers are considered as abstract black boxes. The flexibility of the coupling environment is achieved by wrapping the solvers in a Python layer that provides a driving and communicating

channel. The wrapping procedure is implemented using the Simplified Wrapper and Interface Generator (SWIG) tool [179]. The Python wrapper does not interfere with the libraries and executables of the two solvers but provides all the necessary additional functionalities required to synchronize them and exchange the information required to implement their interaction.

CHAPTER 3

STRAIGHT ARTERY MODELING

3.1 Blood rheology.

Whole blood is a two-phase liquid, composed of cellular elements suspended in plasma, an aqueous solution containing organic molecules, proteins, and salts. The cellular phase of blood includes erythrocytes, leukocytes, and platelets. Erythrocytes, or Red Blood Cells (RBCs), are responsible for the transport of oxygen. Platelets are cell fragments involved in coagulation. Leukocytes (white blood cells) are part of the body's defense mechanism. Normally, the volume of a blood sample consists of less than 1% leukocytes and platelets, 55% plasma, and approximately 45% erythrocytes. Blood is generally assumed to behave like an incompressible fluid with a density of 1050 kg/m^3 [166].

Plasma itself is a Newtonian fluid but the presence of other cells induces a non-Newtonian behavior. While white blood cells and platelets can impact blood rheology, under normal conditions, red blood cells have the most significant influence [138]. The non-Newtonian characteristics of blood is influenced by other factors including the ambient temperature and size of the blood vessels [172]. Hematocrit, defined as the volume of RBCs compared to total blood volume (normal range: 35–45%), is the primary determinant of blood viscosity, especially at the lowest shear rates: doubling of hematocrit results in a 3-to-4-fold increase in blood viscosity at high shear rates, while it prompts an almost 10-fold increase within the lowest shear rate range [33]. The reason for this is that, at low shear rates, the erythrocytes have the ability to form a primary aggregate structure of rod-shaped stacks of individual cells called rouleaux [153]. The viscosity of whole blood demonstrates a nonlinear decrease with increasing shear rate. Blood is therefore a non-Newtonian, shear thinning fluid. Viscoelastic properties are also reported [166]. Beyond a certain shear rate threshold however, the viscosity is nearly constant and blood can be considered to behave as a Newtonian fluid.

The shear thinning behavior of whole blood and its viscoelastic properties can be described using a variety of non-Newtonian models [125]. One of the most well-known approaches is the Casson model [65]. It is commonly used for modeling blood flow in narrow vessels and at low shear rates. In addition to the shear thinning properties, the Casson model also introduces a minimum shear stress τ_y that must be applied for blood to flow [13]. The nonlinear relation between shear stress τ and shear rate $\dot{\gamma}$ is described mathematically by

$$\begin{cases} \tau = \mu(\dot{\gamma})\dot{\gamma} & \text{if } |\tau| \geqslant \tau_y \\ \dot{\gamma} = 0 & \text{if } |\tau| < \tau_y \end{cases} \tag{3.1}$$

with

$$\mu = \left(\sqrt{\mu_\infty} + \sqrt{\frac{\tau_y}{|\dot{\gamma}|}} \right)^2 \tag{3.2}$$

The behavior is therefore described by two constants, the yield stress τ_y and the asymptotic dynamic viscosity μ_∞.

Both the yield stress τ_y and the dynamic viscosity at infinitely large shear rate μ_∞ vary with the hematocrit H_t [49]. As the hematocrit increases, the propensity of RBCs to form aggregates increases, thereby making the fluid more viscous. One can write

$$\begin{aligned} \tau_y &= A(H_t - H_{tc})^3 \\ \mu_\infty &= \mu_p \left(1 + 0.025 H_t + 7.35 \cdot 10^{-4} H_t^2 \right) \end{aligned} \tag{3.3}$$

where $\mu_p = 1.2\ 10^{-3}$ Pa $\cdot$ s, $A = 0.9\ 10^{-7}$ Pa, $H_t \in [0, 100]$ is expressed as a percentage, and $H_{tc} = 6$ [65]. Below H_{tc}, there is no yield stress since the RBCs are too far apart to form rouleaux. At a physiological hematocrit of 40 %, the yield stress is equal to 0.0035 Pa and the viscosity at infinite shear rate is 0.0038 Pa $\cdot$ s. These values will be considered in the following once a Casson fluid is employed.

Figure 3.1 shows the resulting variation of the apparent dynamic viscosity μ as a function of the shear rate and the hematocrit. Both the strong influence of the hematocrit and the shear thinning behavior of blood are clearly apparent.

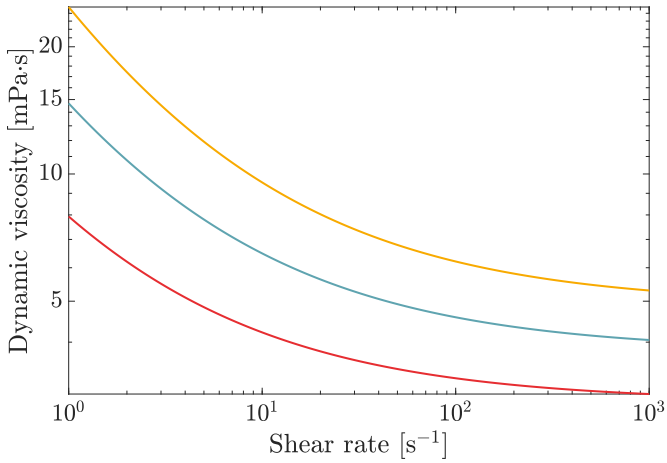

FIGURE 3.1 – Influence of shear rate on effective blood viscosity for hematocrit values of 30% (—), 40% (—) and 50% (—).

3.1.1 Implementation of the Casson model.

Two adaptations of (3.1) are required for the practical implementation of the Casson model in the PFEM3D code.

The discontinuous nature of the Casson model associated with the yield stress makes it challenging to implement in a numerical code. To circumvent this problem, the strategy proposed by Shahzad et al. [159] is implemented. The discontinuous constitutive law is replaced by the continuous approximation

$$\mu(\dot{\gamma}) = \left[\sqrt{\mu_\infty} + \sqrt{\frac{\tau_y}{|\dot{\gamma}|}} \left(1 - \mathrm{e}^{-\sqrt{m|\dot{\gamma}|}} \right) \right]^2 \tag{3.4}$$

where m is a regularization coefficient. This viscosity is thus used without explicitly considering any yield stress. If the shear rate $\dot{\gamma}$ is large with respect to $1/m$ (where m has the dimension of a time), then (3.4) is equivalent to the initial formulation (3.2). For $\dot{\gamma} \to 0$, (3.4) introduces a bounded finite viscosity

$$\mu_0 = \left(\sqrt{\mu_\infty} + \sqrt{m\tau_y}\right)^2 \tag{3.5}$$

while the effective viscosity is infinite in the discontinuous formulation (3.1). In practice, the two models are however expected to produce similar results since the effective viscosity at low strain rate μ_0 can be made arbitrarily large by adjusting the regularization coefficient m. The actual shear rate can therefore be forced to be arbitrarily small, hence mimicking the effect of the yield stress.

As a result, the Casson theoretical model can be approximated with arbitrary accuracy by adjusting the regularization coefficient m. The value of m must be sufficiently large compared to the characteristic value of $1/\dot{\gamma}$ encountered in the flow to reduce the discrepancy between the two models, but small enough to avoid numerical problems associated with excessive nonlinearities at low shear rate.

The 1D formulation of the Casson model considered so far must also be extended to a general 3D flow. This is easily done by applying (3.4) separately to each component of the viscous stress tensor and assessing the total shear strain rate from the norm of the tensor. The final formulation reads therefore

$$\boldsymbol{\tau} = 2\mu(\dot{\gamma})\,\mathbf{D} \tag{3.6}$$

where $\mathbf{D}$ is the strain rate tensor, $\dot{\gamma} = \sqrt{2\,\mathbf{D} : \mathbf{D}}$, and the continuous formulation (3.4) of the effective viscosity is used.

3.1.2 Verification of the implementation of the Casson model.

In order to verify the implementation of the Casson fluid, we consider a simple 2D Poiseuille flow between two rigid parallel plates. The flow is driven by a constant pressure difference $\Delta p = 2$ Pa applied between the inlet and outlet sections. The model is run until a steady fully developed flow is obtained in the outlet section. The numerical data of the test case are listed in Table 3.1. Results are also compared with that obtained with a Newtonian fluid. Note that the fluid parameters used here are not the physiological values of blood discussed in the previous section but are merely selected to verify the implementation of the Casson model.

Parameters	*Values*	*Units*
Height $2w$	0.005	m
Length L	0.06	m
Longitudinal pressure gradient K	33.333	Pa/m
Asymptotic dynamic viscosity μ_∞ (Casson)	0.0035	Pa · s
Yield stress τ_y (Casson)	0.03	Pa
Dynamic viscosity μ (Newton)	0.0035	Pa · s

TABLE 3.1 – Parameters of the case study used to verify the implementation of the Casson fluid model.

For a Newtonian fluid, the analytical solution of this problem is the classical parabolic velocity profile

$$u = \frac{K}{2\mu}(w^2 - y^2), \qquad \text{with} \qquad K = -\frac{\partial p}{\partial x} \tag{3.7}$$

where $y \in [-w, w]$ is the coordinate perpendicular to the two plates and w is the half-distance between them [65]. The corresponding flow rate (per unit thickness) is given by

$$q = \frac{2Kw^3}{3\mu} \tag{3.8}$$

The corresponding solution for a Casson fluid can be derived by considering the linear variation

$$\tau(y) = -Ky \tag{3.9}$$

of the shear stress between the two plates and, accordingly, a small region in the center of flow where the shear stress is below the yield stress and the adjacent fluid filaments flow at the same velocity. The full velocity profile is therefore described by

$$u(y) = \begin{cases} \dfrac{K}{2\mu_\infty}(w^2 - y^2) + \dfrac{K}{\mu_\infty}\left[y_0(w-y) - \frac{4}{3}\sqrt{y_0}\left(w^{3/2} - y^{3/2}\right)\right] & \text{for} \quad |y| \geqslant y_0 \\ u(y_0) & \text{for} \quad |y| < y_0 \end{cases} \tag{3.10}$$

where $y_0 = \tau_y/K$ is the half-width of the central core moving as a solid body. Note that the Newtonian parabolic profile is recovered if $\tau_y = 0$. The corresponding flow rate is given by

$$q = \frac{2Kw^3}{3\mu_\infty} - \frac{K}{15\mu_\infty}\left[y_0^3 - 15w^2 y_0 + 24w^{5/2} y_0^{1/2}\right] \tag{3.11}$$

The regularization parameter m controls the size of the fillet between the two parts of the theoretical curve. As shown in Figure 3.2, a value of 200 s for the regularization coefficient m provides an accurate approximation of the theoretical constitutive law in the whole range of shear rate anticipated in the considered flow.

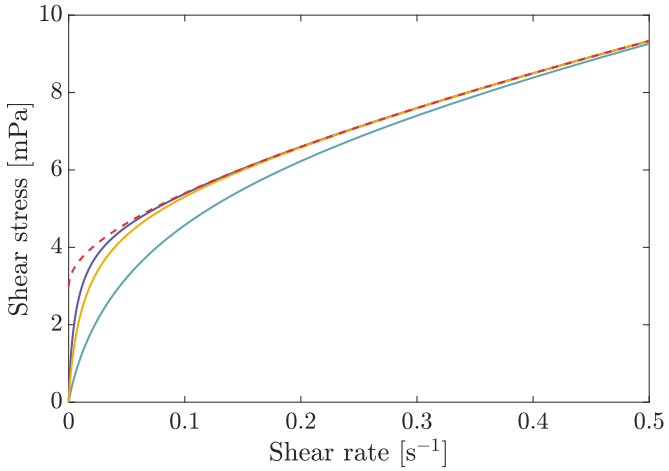

FIGURE 3.2 – Comparison between theoretical (- - -) and numerical Casson laws. Numerical laws are for different values of the regularization parameter: $m = 100$ s (—), $m = 200$ s (—) and $m = 400$ s (—).

The numerical results of the Poiseuille flow are shown in Figure 3.3 where they are compared with the analytical solutions (3.7) and (3.10). The model results nicely fit the analytical solutions, which provides a sound verification of the implementation of the Casson model in PFEM3D.

Note that both models use 20 equidistant grid points across the section and the tiny differences between the numerical and analytical results can be further decreased with a refined mesh. It is

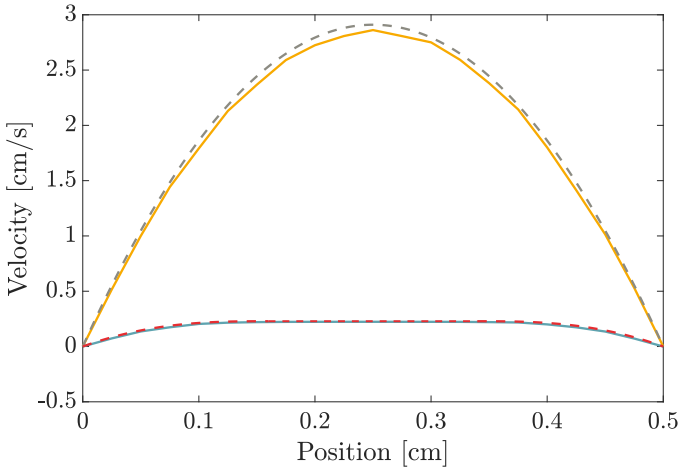

FIGURE 3.3 – Poiseuille profiles with Newtonian fluid model (theoretical (- - -) and numerical (——)) and Casson fluid model (theoretical (- - -) and numerical (——)).

also worth noting that the theoretical profiles are computed using the actual pressure gradient computed in the final section of the numerical model to compensate for the significant entry length.

From a qualitative point of view, Figure 3.3 also illustrates the two effects of the Casson model. First of all, the increased effective viscosity leads to a sharp reduction of the maximum velocity with respect to the corresponding Newtonian model: the velocity maximum decreases from 2.91 cm/s (Newton) to 0.23 cm/s (Casson). Second, while the typical parabolic profile of a Newtonian fluid shows a distinct maximum at its center, the velocity profile for Casson remains flat in a large central part. This is expected since, with the simulation parameters, the ratio y_0/w of the width of the no-shear zone to the channel width reaches 36%.

This sharp reduction of the velocity magnitude translates into a corresponding drop of the flow rate across the model domain. The numerical estimates of the flow rates per unit length of transverse direction for the two models are 94 mL/(s · mm) and 9 mL/(s · mm), respectively for the Newtonian fluid and the Casson fluid: the flow rate is decreased by a factor of 10 when the Newtonian model is replaced by a Casson one. Note that these numerical estimates are both within 5% of the corresponding theoretical values.

3.1.3 On the relevance of the Casson model.

While the previous sections suggest that the use of a Casson model has a strong influence on both the velocity profile and the flow rate, one must take into account the fact that the material parameters that were selected to verify the implementation of the Casson model have little in common with the actual physiological values defined by (3.3). To assess the influence of the constitutive model on blood flow, we consider now these physiological values and realistic geometries of blood vessels.

It is widely known that the effective viscosity of blood changes with the hemodynamic conditions. The apparent blood viscosity differs between the microcirculation and the large arteries, where shear rate can vary from a few s^{-1} to more than 1000 s^{-1} [125]. At the high shear rates encountered in large arteries, non-Newtonian models asymptote to the Newtonian limit, justifying the Newtonian assumption [31].

In this section, we investigate the relevance of the Newtonian assumption in vessels of different sizes using the analytical velocity profiles of the steady, fully developed, viscous, axisymmetric flow in a rigid straight artery of radius a.

The so-called Hagen-Poiseuille solution

$$v(r) = \frac{a^2}{4\mu} K \left(1 - \frac{r^2}{a^2}\right) \tag{3.12}$$

(where K is the longitudinal pressure gradient and r is the radial coordinate) describes the parabolic profile obtained with a Newtonian fluid [65].

The corresponding solution for the Casson fluid can be shown to be described by

$$v(r) = \begin{cases} \dfrac{K}{2\mu_\infty}\left[r_0\left(a-r\right) - \dfrac{4\sqrt{r_0}}{3}\left(a^{3/2} - r^{3/2}\right) + \dfrac{1}{2}\left(a^2 - r^2\right)\right] & \text{for} \quad r \geqslant r_0 \\ v(r_0) & \text{for} \quad r < r_0 \end{cases} \tag{3.13}$$

where $r_0 = 2\tau_y/K$ is the radius of the central core moving as a solid body.

We consider two situations with two different radii: a radius of 3 mm, typical of the middle cerebral artery, and a radius of 2 cm, which is typical of the largest artery in the abdomen, namely the abdominal aorta [20]. These two types of vessels are the most common locations of aneurysms. Some researchers employed the Newtonian model for the blood in cerebral and abdominal aneurysms [95, 163] and some others applied the non-Newtonian model in the same situations [147, 169]. Our motivation here is to use the analytical results to determine when significant differences can be anticipated.

Figure 3.4a shows the relation between the flow rate and the pressure gradient in the two types of blood vessels. The pressure gradient is proportional to the flow rate for a Newtonian fluid (This linear relation does not appear in Figure 3.4a because of the log scale.), but the existence of a yield radial position r_0 introduces a nonlinear relationship between the two parameters with a Casson fluid. For a given pressure gradient, the flow rate is decreased in case of a Casson assumption as the effective viscosity of the fluid is always greater than that of the Newtonian fluid. This effect decreases however as the pressure gradient increases. The difference between the Newtonian and non-Newtonian curves is also much more significant for the smallest artery.

The results for the narrow middle cerebral artery show also the effect of the yield stress. A pressure gradient of 2.3 Pa/m is necessary to push the flow through the blood vessel. If the pressure difference is lower than that, the fluid remains at rest.

Literature suggests that the abdominal artery of a healthy subject carries a flow rate of about 2000 mL/min [174]. A pressure gradient of 1.9 Pa/m is then required to drive such a steady flow under the Newtonian assumption, while it reaches 4.2 Pa/m with the Casson model. This difference in pressure drop is not that significant considering the pressure waves of thousands of Pa traveling through the aorta. When the flow drops to 100 mL/min, the corresponding estimates are of 0.9 Pa/m and 0.1 Pa/m, respectively for the Casson model and the Newtonian model, which is of course much more significant in relative terms but is negligible in absolute figures. For the middle cerebral artery, flow rates of 100 mL/min are typically reported [170]. An absolute difference of 35 Pa/m between the pressure drops can then be anticipated, which is much more significant.

The negligible difference between the results obtained for the Newtonian and non-Newtonian models suggests that the assumption of Newtonian blood is acceptable for the abdominal aorta.

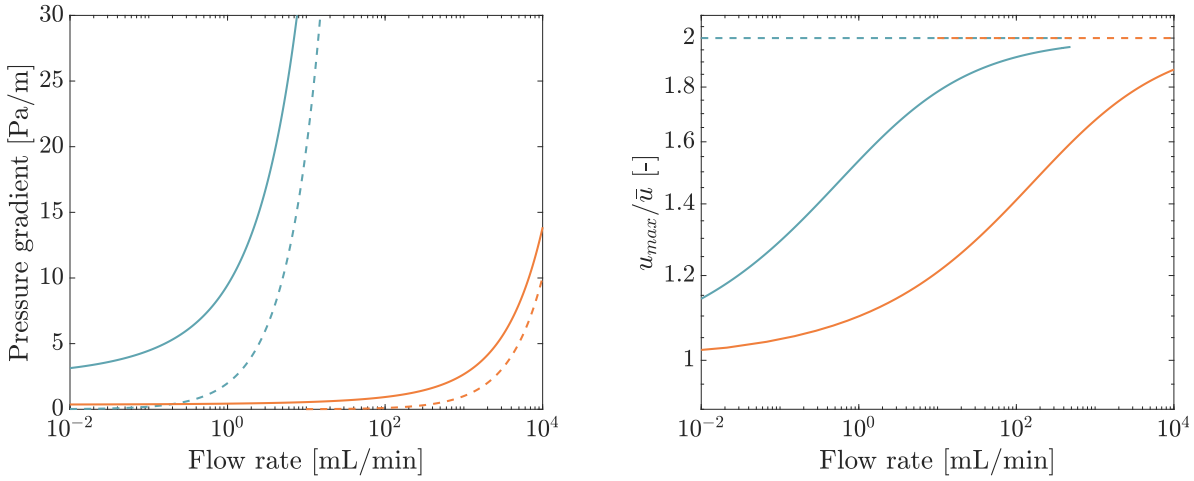

(a) (b)

FIGURE 3.4 – Pressure gradient (a) and ratio between the peak and average velocity (b) as a function of the flow rate for vessels radii of 3 mm (——) and 20 mm (——) with Newtonian (- - -) and Casson (——) fluid models.

The model assumption must however be considered with more care when studying the blood flow in the smallest blood vessels.

As shown in the previous section, the type of fluid also influences the shape of the velocity profile. To document this aspect, Figure 3.4b shows the ratio of the maximum velocity to its average value over the section of the blood vessel. For the Newtonian fluid, the maximum velocity is always twice the average value. This ratio is independent of the pressure gradient driving the flow and size of the blood vessel. For the Casson model however, the ratio is smaller since the velocity profile is flat in the central region. At the smaller flow rates, a Newtonian assumption may therefore overestimate the maximum velocity with respect to the Casson model. With the physiological flow rates reported in the previous paragraph, the difference between the two models is moderate. In pathological conditions (*e.g.,* stenosis, where the artery becomes blocked due to cholesterol deposits), the flow is reduced and the model assumption may however have more influence on the predicted hemodynamics.

Note that the above conclusions apply to the steady fully developed profile. As it will be shown later, the pulsatile nature of the flow in the blood vessels also play an important role.

3.2 Constitutive equations of biological tissues of the cardiovascular system.

3.2.1 Properties of the arterial wall.

The mechanical behaviors of blood vessels are very complicated [58]. This complexity arises mainly from the hierarchical structures across different scales, ranging from fiber-reinforced structures at the microscale to multilayered structures at the macroscale [172]. Collagen fibers, in particular, contribute significantly to the arterial wall strength and stability and, more generally, to the mechanical behavior of the vascular wall.

The pressure-diameter relationship of an artery is highly nonlinear [20]. The compliance, which plays a key role in propagating the pulsatile blood flow, is therefore not constant. The

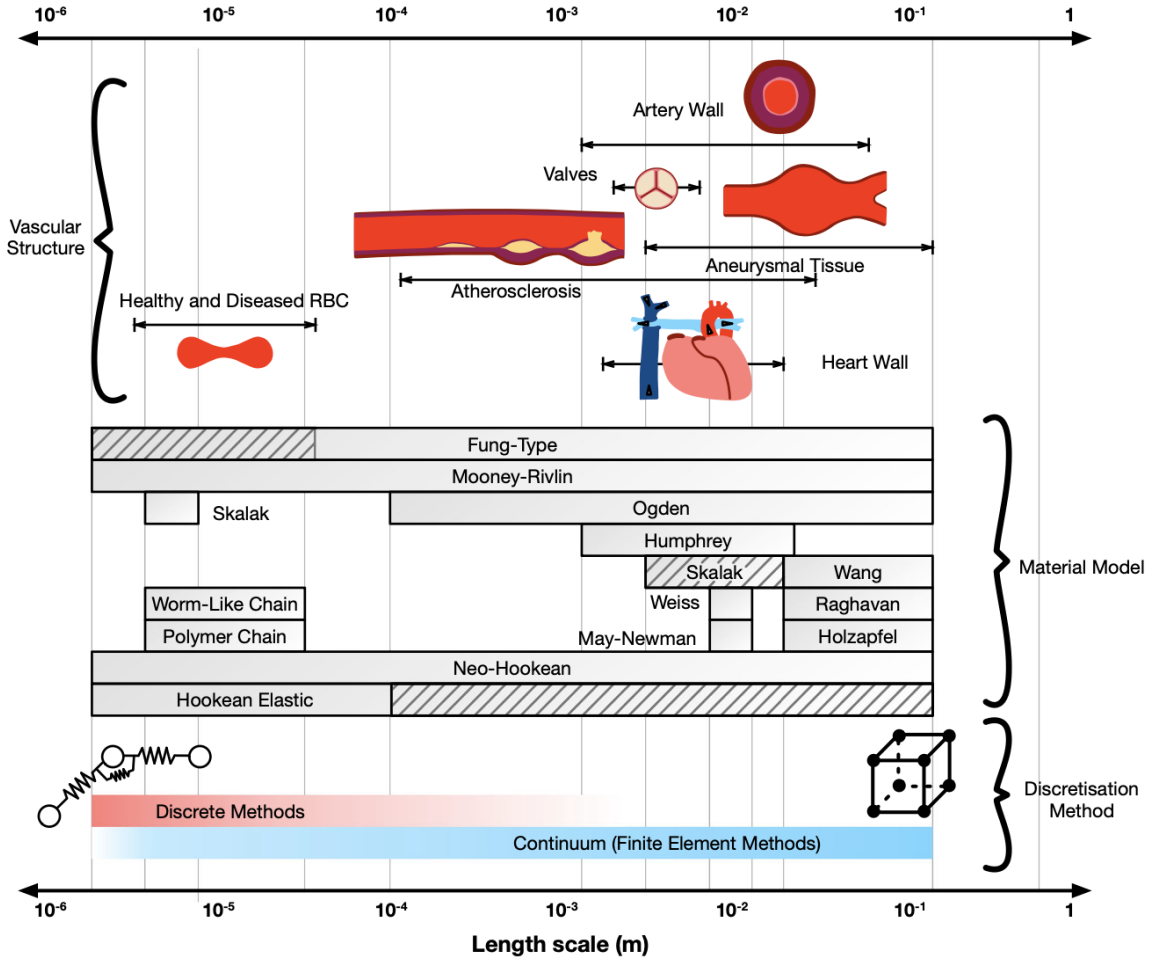

FIGURE 3.5 – Comparison of the different constitutive equations used in modeling biological tissues of the cardiovascular system (reproduced from Owen et al. [131]).

nonlinear behavior is largely explained by the disorganized arrangement of elastin and collagen fibers in the unpressurized state. With increasing pressure, these fibers progressively align. At the lower end of physiological pressure (80 mmHg), elastin fibers are almost straight. Further pressure increase leads to the elongation of elastin fibers and the ongoing alignment of collagen fibers until the higher physiological limit (120 mmHg) is reached, where both fiber types are fully extended. Thus, at lower pressures, the artery mechanical response is primarily determined by the less rigid elastin. At higher pressures, the more rigid collagen fibers become predominant, demanding greater force for any change in diameter and thereby safeguarding the blood vessels from damage or rupture. Large arteries undergo significant deformations, necessitating the use of nonlinear strain measures to accurately describe their behavior.

The wall of arteries and veins are made of three layers called the intima (inner layer), the media (middle layer), and the adventitia (outer layer). This structure will be discussed in more detail in chapter 5. The geometric arrangement of fibrous components in the circumferential direction, especially in the media layer, results in anisotropic behavior. Blood vessels are generally stronger along the fiber direction than perpendicular to it [20]. In the media layer, fibers are aligned circumferentially, while in the adventitia layer, fibers are sparser and less organized.

Research has also shown that certain cardiovascular components, such as the myocardium, exhibit viscoelastic properties. However, the importance of this characteristic is subject to debate

because the added complexity to the model is hard to justify given the uncertainties about how much viscous effects impact structural deformation [131]. It was already concluded that the influence of viscoelasticity on quantities of interest such as the Wall Shear Stress (WSS) is rather small [8].

Furthermore, the interplay between biological, chemical, mechanical, and physical factors contributes to the complexity of blood vessel modeling [171]. Consequently, simulating blood flow and the mechanical behavior of blood vessels, along with their interactions, presents significant challenges. Additionally, the material properties vary depending on the patient, the specific vasculature location/type, and the state of the disease. Therefore, it is necessary to develop and tailor material models to the particular issue under investigation, which can be a complex task [77].

Figure 3.5, taken from Owen et al. [131], provides a general summary of the many different wall models used in the literature to address the deformation of biological tissues. The deformation of biomaterials is represented predominantly by models with reversible behavior to reflect the elastic nature of the material. These include the linear or Hookean elasticity used in early cardiovascular structural models, and a couple of hyperelastic models, like the simplest nonlinear or Neo-Hookean elasticity, and a number of tailored nonlinear elasticity models, such as Mooney–Rivlin or Fung elasticity models [131]. Comparing the dynamics of atherosclerosis using rigid, linear elastic, Neo-Hookean, Mooney-Rivlin, and Holzapfel material models under both steady state and pulsatile conditions, Kallekar et al. [93] have demonstrated that selecting an appropriate wall model is crucial.

Before delving into the details of the various models, the following section will provide the fundamental concepts of large deformation in continuum mechanics essential for understanding these models [16].

3.2.2 Elements of continuum mechanics.

During its deformation, a body $\mathcal{B}$ occupies different configurations. Figure 3.6 illustrates the transition of body $\mathcal{B}$ from a reference configuration at time t_0 to a deformed state at time $t = t_0 + \Delta t$.

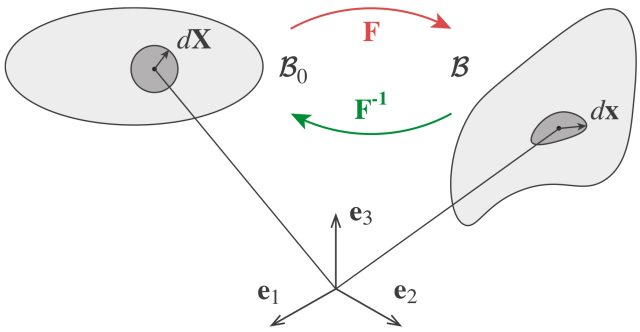

FIGURE 3.6 – Reference and current deformed configurations of a body $\mathcal{B}$ [14].

The transformation can be described by the mapping

$$\mathbf{x} = \mathbf{x}(\mathbf{X}, t) \tag{3.14}$$

where $\mathbf{X}$ denotes the reference position of a particle and $\mathbf{x}$ is the current position at time t. The deformation of a material vector $d\mathbf{x}$ is given by

$$d\mathbf{x} = \mathbf{F} d\mathbf{X} \tag{3.15}$$

where

$$\mathbf{F} = \frac{\partial \mathbf{x}}{\partial \mathbf{X}} \tag{3.16}$$

is the deformation gradient tensor or Jacobian matrix of the deformation. $\mathbf{F}$ is a second order and non-symmetrical tensor that varies through the deformation process. The determinant of the deformation gradient tensor is called the Jacobian and is denoted by J. It describes the change of volume of an infinitesimal volume of material from the reference $\mathbb{V}_0$ to the current configuration $\mathbb{V}(t)$.

By differentiating (3.15) with respect to time, a similar expression for the deformation velocity field can be obtained as

$$d\dot{\mathbf{x}} = \dot{\mathbf{F}} d\mathbf{X} = \dot{\mathbf{F}}\mathbf{F}^{-1} d\mathbf{x} = \mathbf{L} d\mathbf{x} \tag{3.17}$$

where $\mathbf{L}$ is the velocity gradient tensor. This tensor can be decomposed into a symmetric part $\mathbf{D}$ and an antisymmetric part $\mathbf{W}$ which respectively represent the strain rate and the spin.

The deformation gradient tensor describes both the rigid rotation of the body and its stretching. The latter can be extracted from $\mathbf{F}$ using either the right or left Cauchy-Green deformation tensors, respectively defined as

$$\mathbf{C} = \mathbf{F}^{\mathrm{T}}\mathbf{F} \qquad \text{and} \qquad \mathbf{B} = \mathbf{F}\mathbf{F}^{\mathrm{T}} \tag{3.18}$$

By construction, both $\mathbf{C}$ and $\mathbf{B}$ are symmetric tensors. The left Cauchy-Green deformation tensor $\mathbf{B}$ is used in Metafor.

As any other tensor, the left Cauchy-Green deformation tensor can be expressed in various coordinate systems and is then represented by a 3×3 squared matrix $\mathbf{B}$. The mechanical behavior and properties of an isotropic deformable solid must be independent of any particular direction in space and must therefore depend on the invariants of $\mathbf{B}$ given by

$$I_1 = tr(\mathbf{B}) \tag{3.19}$$

$$I_2 = \frac{1}{2}\left[tr(\mathbf{B})^2 - tr(\mathbf{B}^2)\right] \tag{3.20}$$

$$I_3 = \det(\mathbf{B}) = J^2 \tag{3.21}$$

The purpose of the constitutive equation is to define the strain-stress curve or, more specifically when large deformations are considered, to relate the elements of the Cauchy stress tensor $\boldsymbol{\sigma}$ (the true stress tensor in the current configuration) to those of the left Cauchy-Green deformation tensor $\mathbf{B}$. Of specific interest are the so-called hyperelastic materials, *i.e.,* materials for which the work done by the stresses during a deformation process depends only on the initial and final configurations (with no dissipation during the deformation process). This property allows the definition of a strain energy density function W that identifies with the elastic energy per unit volume stored during the deformation process. In the following, we will only consider isotropic models (Metafor is currently limited to isotropic hyperelastic materials.). A thermodynamically consistent formulation of the strain-stress relations for such hyperelastic isotropic materials can be derived as

$$\boldsymbol{\sigma} = \frac{2}{J}\mathbf{B}\frac{\partial W}{\partial \mathbf{B}} \tag{3.22}$$

The hyperelastic formulation gives a linear or nonlinear relation between stress and strain. This material model is mainly used to model the rubbery behavior of polymeric materials and polymeric foams.

The strain energy density function can be expressed in terms of the invariants of the left Cauchy-Green tensor,

$$W = W(I_1, I_2, I_3) \tag{3.23}$$

which leads to some interesting simplifications for the implementation of the models.

The quasi-incompressibility of hyperelastic materials can be enforced by introducing the modified version of the deformation gradient tensor $\bar{\mathbf{F}}$ defined by

$$\bar{\mathbf{F}} = J^{-1/3}\mathbf{F} \tag{3.24}$$

This adjusted deformation gradient is such that

$$\det \bar{\mathbf{F}} = 1 \tag{3.25}$$

and captures therefore the isochoric deformations. Using this volume preserving part of $\mathbf{F}$, a new left Cauchy-Green tensor can be defined by

$$\bar{\mathbf{B}} = \bar{\mathbf{F}}\bar{\mathbf{F}}^{\mathbf{T}} = J^{-2/3}\mathbf{B} \tag{3.26}$$

with the reduced invariants of $\bar{\mathbf{B}}$

$$\bar{I_1} = J^{-2/3}I_1 \tag{3.27}$$
$$\bar{I_2} = J^{-4/3}I_2 \tag{3.28}$$
$$\bar{I_3} = 1 \tag{3.29}$$

Finally, the strain energy function W is assumed to be the sum of two independent contributions: an isochoric deformation $\bar{W}$ and a volume change deformation $Kf(J)$, *i.e.,*

$$W(\bar{I_1}, \bar{I_2}, J) = \bar{W}(\bar{I_1}, \bar{I_2}) + Kf(J) \tag{3.30}$$

where K is the bulk modulus or any penalty parameter and f is an appropriate function such that $f(1) = 0$. For isotropic materials, the Cauchy stresses can then be expressed as

$$\boldsymbol{\sigma} = p\mathbf{I} + \frac{2}{J}dev\left[\frac{\partial \bar{W}}{\partial \bar{I_1}}\bar{\mathbf{B}} - \frac{\partial \bar{W}}{\partial \bar{I_2}}\bar{\mathbf{B}}^{-1}\right] \tag{3.31}$$

where *dev* denotes the deviatoric part of the tensor.

Fortunately, by an appropriate choice of $f(J)$, this approach also avoids the *Rivlin effect* associated with hyperelastic materials, *i.e.*, the fact that a non-zero pressure is created even if no change of volume occurs.

There exists many possibilities regarding the choice of the strain energy density function. Some can describe complex material behaviors, but require many material parameters that have to be experimentally identified: a trade-off between accuracy and complexity of the material model is required. Some of them will be presented in the next section.

3.2.3 Constitutive equations of the arterial wall.

Because of their structural component supported by collagen, blood vessel walls exhibit a soft and flexible structure, and the blood flow through the arteries can significantly modify the vessel radius. Therefore, it is appropriate to use a hyperelastic model for simulating vessel walls [147]. Note that this approach allows for nonlinear stress-strain relationships but is inappropriate to

describe irreversible processes, restricting the modeling capability to pre-growth and rupture phenomena [131].

One of the simplest hyperelastic material models is the Saint Venant–Kirchhoff model, which is just an extension of the geometrically linear elastic material model to the geometrically nonlinear regime. The Saint Venant-Kirchoff model has been used in some biomechanical studies, for example for the modeling of certain types of prosthetic (polymeric) valves, but is superseded by the models below for realistic applications [81, 94].

Many more numerical studies rely on the Neo-Hookean model. This model can be fully defined by its strain energy density function

$$W(\bar{I}_1, J) = C_1(\bar{I}_1 - 3) + \frac{1}{2}K\left[(J-1)^2 + \ln^2 J\right] \tag{3.32}$$

where, for consistency with linear elasticity, the constant C_1 must be taken as half the shear modulus. This approach has been widely used to model the deformation of the aortic artery [8], but also to describe atherosclerotic vessels and in aneurysms development study [144, 191]. For small strains, the Neo-Hookean model yields similar stresses than the simple linear Hookean elasticity. For large strains however, it provides a refined, nonlinear description of deformations. A study by Parshin et al. [133] claims that it is the optimal approach for modeling the mechanics of cerebral aneurysm wall and addressing fluid-structure interaction problems. More generally, however, it is considered to be suitable for stretches up to 20% [131].

To model biological tissues at high strains, the one-parameter Neo-Hookean model is generally replaced by more general models, such as the Mooney-Rivlin model. The two-parameter strain energy function of this model can be expressed in terms of the reduced invariants as

$$W(\bar{I}_1, \bar{I}_2, J) = C_1(\bar{I}_1 - 3) + C_2(\bar{I}_2 - 3) + \frac{1}{2}K\left[(J-1)^2 + \ln^2 J\right] \tag{3.33}$$

where, for consistency with linear elasticity, it requires that

$$2(C_1 + C_2) = G = \frac{E}{2(1+\nu)} \tag{3.34}$$

In the following, the penalty coefficient K will always be taken as the bulk modulus, *i.e.*,

$$K = \frac{E}{3(1-2\nu)} \tag{3.35}$$

The formulation (3.33) shows that the Mooney-Rivlin model can be considered as a natural extension of the Neo-Hookean model including a dependency on the second reduced invariant of the left Cauchy-Green deformation tensor.

The Mooney-Rivlin model has been originally developed for rubber-like materials. It is suitable for materials that undergo large strains and exhibit isotropic, homogeneous, and nearly incompressible properties. It is often employed in soft tissue mechanics and biomechanics. In particular, it appears in the study of many cardiovascular structures across a number of scales and in models of the deformation of the blood vessel, especially in scenarios where healthy tissues are not a primary concern [99, 131].

In some studies of the deformation of blood vessels, the two-parameter formulation (3.33) is extended into a 5-parameter hyperelastic Mooney-Rivlin model including quadratic terms of the reduced invariants [147].

A few biomechanical studies resort to the Ogden hyperelastic model to describe the nonlinear stress–strain behavior of complex biological tissues [32]. The Ogden model differs from the above Neo-Hookean and Mooney-Rivlin models in that it is expressed in terms of the principal stretches. Note that for specific choices of its parameters, the Ogden model recovers both the Neo-Hookean model as well as the Mooney–Rivlin model.

Raghavan and Vorp [139] developed one of the first models specific to abdominal aortic aneurysmal tissue. The isochoric deformation function can be written as

$$\bar{W} = C_{10}(\bar{I}_1 - 3) + C_{20}(\bar{I}_1 - 3)^2 \tag{3.36}$$

and reduces therefore to the Neo-Hookean model if $C_{10} = G/2$ and $C_{20} = 0$. Using experimental data of the aortic aneurysm, they evaluated these coefficients to be equal to $C_{10} = 17.4$ N/cm^2 and $C_{20} = 188.1$ N/cm^2. These values are used in many studies where the specific behavior of abdominal aortic aneurysms can therefore be taken into account [95, 163, 172]. Formulation (3.36) can also be seen as a particular case of the more general Yeoh model

$$\bar{W} = C_1(\bar{I}_1 - 3) + C_2(\bar{I}_1 - 3)^2 + C_3(\bar{I}_1 - 3)^3 \tag{3.37}$$

with $C_3 = 0$.

Fung investigated the mechanics of biological soft tissues, including blood vessels, and introduced numerous phenomenological models [59]. The Fung's hyperelastic constitutive relation has been used extensively. Different mathematical formulations are available in the literature. Sun et al. [172] for instance use

$$\bar{W} = \frac{G}{2b}\Big[\exp\{b(\bar{I}_1 - 3)\} - 1\Big] \tag{3.38}$$

where b is a material parameter. The exponential function of strain accounts for the steep stiffening of the material thanks to the alignment of stretched collagen fibers.

Figure 3.7 shows the stretch-stress curves for different hyperelastic models of the aortic material. Of course, the different models contain adjustable parameters that add to the variability associated with the different models. Among the different hyperelastic models, the ones by Raghavan and Fung exhibit however the most pronounced nonlinear behavior [131].

The above models describe blood vessels as homogeneous and isotropic continuum and pay therefore little attention to their multiscale hierarchical structure. Although isotropic models such as the Neo-Hookean and Mooney–Rivlin have been shown to give reasonable representations and are capable of capturing the large nonlinear elastic response of the artery, improvements can be achieved by considering histological details of the artery wall. The walls of the human artery are known to consist of two distinct symmetrical bands of collagen fibers that are helically wound around the artery axis [93]. This arrangement, combined with the soft tissue nature of collagen and the intervening non-collagenous matrix, results in an anisotropic nonlinear response of arteries when subject to loading.

The Holzapfel model is the most accurate nonlinear elastic model leading to an anisotropic response under loading. The model considers two layers, *i.e.,* a thick-walled elastic circular cylindrical tube and fiber-reinforcements. Anisotropic models such as those proposed by Holzapfel et al. require details of the arrangement of fibers within the wall which has traditionally been obtained in vitro with varying degrees of difficulty depending on the artery location [131]. Holzapfel et al. [79] also extended their multilayer arterial wall model for coronary arteries (including an exponential isotropic term as proposed by Fung and an anisotropic term relating to the angle

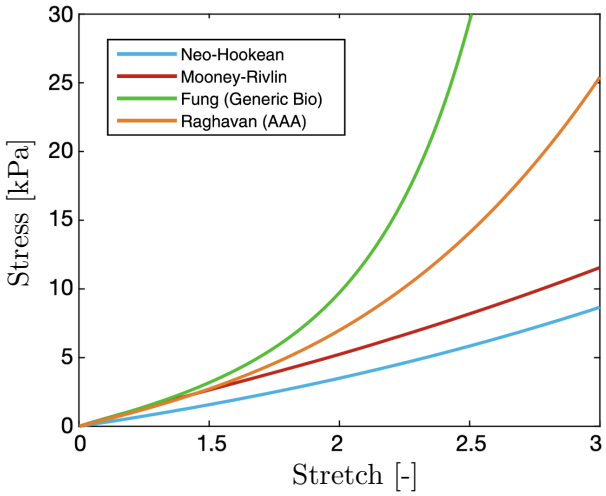

FIGURE 3.7 – Stretch-stress curves (shear mode) for some commonly used models of the aortic material. Reproduced from Owen et al. [131].

between fiber reinforcement and circumferential direction in each layer). Only few studies have however incorporated such representative models of arteries in Fluid-Structure Interaction (FSI) simulations.

3.3 Modeling of a straight artery.

Besides the rheology of blood studied in the previous section, one of the most important aspects of the flow in many blood vessels is the deformability of the wall, which motivates the use of numerical models able to describe the corresponding flow-structure interactions. As a first example of these processes, we consider here the blood flow in the segment of a straight artery.

An axisymmetric model is considered because it is the minimal configuration that accounts for the typical balance of forces encountered in blood vessels. The vessel wall structure is designed

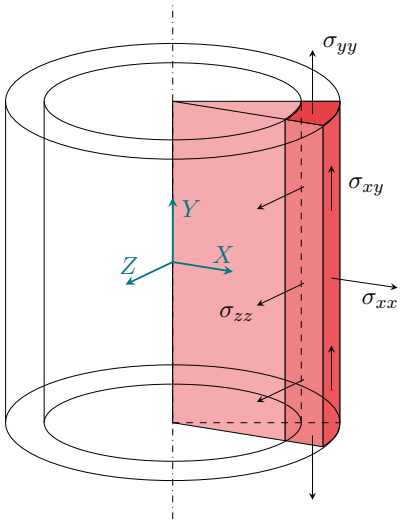

FIGURE 3.8 – Stresses generated in the vascular wall from the physiological forces: hoop stress σ_{zz}, longitudinal stress σ_{yy}, radial stress σ_{xx}, and shear stress σ_{xy}.

to resist and propagate the forces exerted by the blood flow that act radially and longitudinally: the internal pressure produces a radial stress and an internal circumferential (or hoop) stress in the vessel wall, the longitudinal distending force produces an internal longitudinal stress, and the blood flow also induces a shear stress parallel to the vessel lumen (tangential to the flow axis). A simple 2D plane strain model would not be appropriate to capture these different stresses [20]. The axes and notations used in the model of the straight artery and the other axisymmetric models are shown in Figure 3.8.

3.3.1 Propagation of a pressure pulse.

A first numerical experiment is performed to study the propagation of a pressure wave in the deformable artery. For this simulation, the parameters are chosen according to the previous studies of Sun et al. [172] and Formaggia et al. [55]. The geometrical data reported in Table 3.2 are typical of all medium arteries in the human body [20]. Table 3.3 lists the different parameters describing the fluid and solid domains. The geometry is schematized in Figure 3.9.

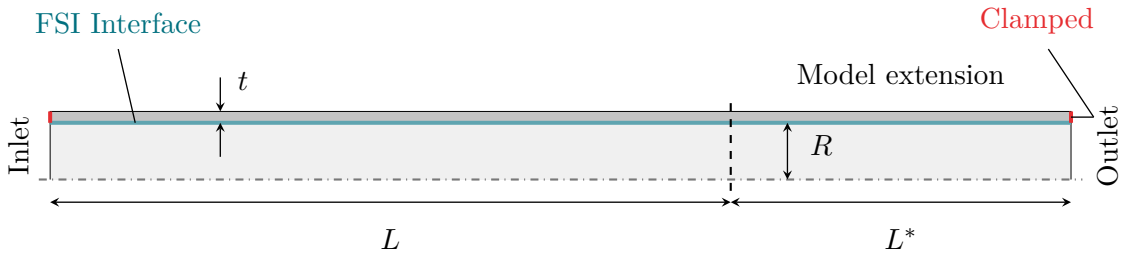

FIGURE 3.9 – Geometry of the axisymmetric straight artery with fluid domain ( ), solid domain ( ), and boundary conditions (clamped (—) and FSI interface (—)).

Parameters	*Values*	*Units*
Length L	6	cm
Length extension L^*	3	cm
Radius R	0.5	cm
Thickness of artery wall t	0.1	cm

TABLE 3.2 – Geometrical parameters for the straight artery simulations used to study the propagation of a pressure pulse.

Parameters	*Values*	*Units*
Fluid density ρ^f	1050	kg/m^3
Arterial wall density ρ^s	1100	kg/m^3
Dynamic viscosity μ	0.0038	Pa · s
Arterial wall Young's modulus E	0.1	MPa
Arterial wall Poisson's ratio ν	0.49	-

TABLE 3.3 – Material parameters for the straight artery simulations used to study the propagation of a pressure pulse.

In line with the previous studies by Sun et al. [172] and Formaggia et al. [55], a pressure pulse of 2000 Pa with a duration of 0.005 s is applied at the inlet (Fig. 3.10). A constant zero pressure is prescribed at the outlet. Both the left and right ends of the artery are fixed. The fluid is Newtonian. A simple Hookean law is used to describe the deformability of the solid material. Although such a constitutive law cannot capture the complex physiological behavior of the arterial

wall (see section 3.2.1), it is sufficient for the present purpose of demonstrating the ability of the model to describe the propagation of pressure waves along blood vessels. More physiologically realistic approaches will be considered later. Note however that the linear elasticity approach used in this work relies on a hypoelastic formulation, which allows the appropriate consideration of large rotations by resorting to the Jaumann (objective) rate of the Cauchy stress.

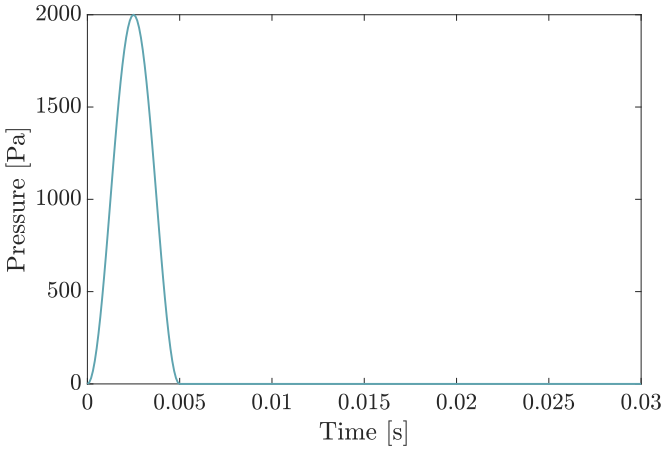

FIGURE 3.10 – Pressure pulse prescribed at the inlet of the straight artery.

The fluid domain is discretized with an initially uniform distribution of PFEM particles spaced 0.05 cm apart, while the solid domain is described by a transfinite mesh with 4 linear elements across the artery wall and 40 elements along the axis. The flow-structure interaction occurs along the common boundary of the two subdomains. The model is integrated forward in time for 30 ms with a time step of 0.1 ms starting with zero pressure and velocity.

The results plotted in Figure 3.11 show the propagation of the pressure pulse with time. The figure also depicts the artificial downstream extension of the fluid domain introduced to avoid spoiling the solution by the reflection of the wave on the downstream boundary. Unless appropriate absorbing or radiation boundary conditions are implemented, the incoming wave is reflected on the downstream boundary where the pressure is kept at a constant value. Such a reflection is clearly a numerical artifact that must be avoided. To delay this reflection and get meaningful results about the forward motion of the pressure wave, an additional segment of blood vessel of 3 cm long is introduced (called model extension in Figure 3.11), which is long enough to delay the arrival of the reflected pressure wave in the domain of interest beyond the simulation time limit.

Figure 3.11 shows how a pressure wave is generated upstream and induces the deformation of the artery wall. The local increase of pressure accelerates the flow from the high pressure region to the downstream lower pressure region. The blood vessel is also locally distended and temporarily stores blood until the fluid pressure decreases. The balance of these two effects causes a deformation wave to propagate along the artery wall. The pressure and deformation waves propagate along the vessel at the same velocity. These results are similar to those presented by Sun et al. [172][1]. Figure 3.12a and 3.12b show the time series of the pressure and velocity at two particular locations on the symmetry axis of the artery. Both variables vary in phase and reach their peak value at the same moment in time, which is characteristic of a propagating wave component.

[1]Note that Sun et al. [172] do not introduce any extension of their model domain and erroneously analyze their results for times much longer than the time required for the reflected wave to affect the domain of interest. Their conclusions clearly do not make sense for such longer times.

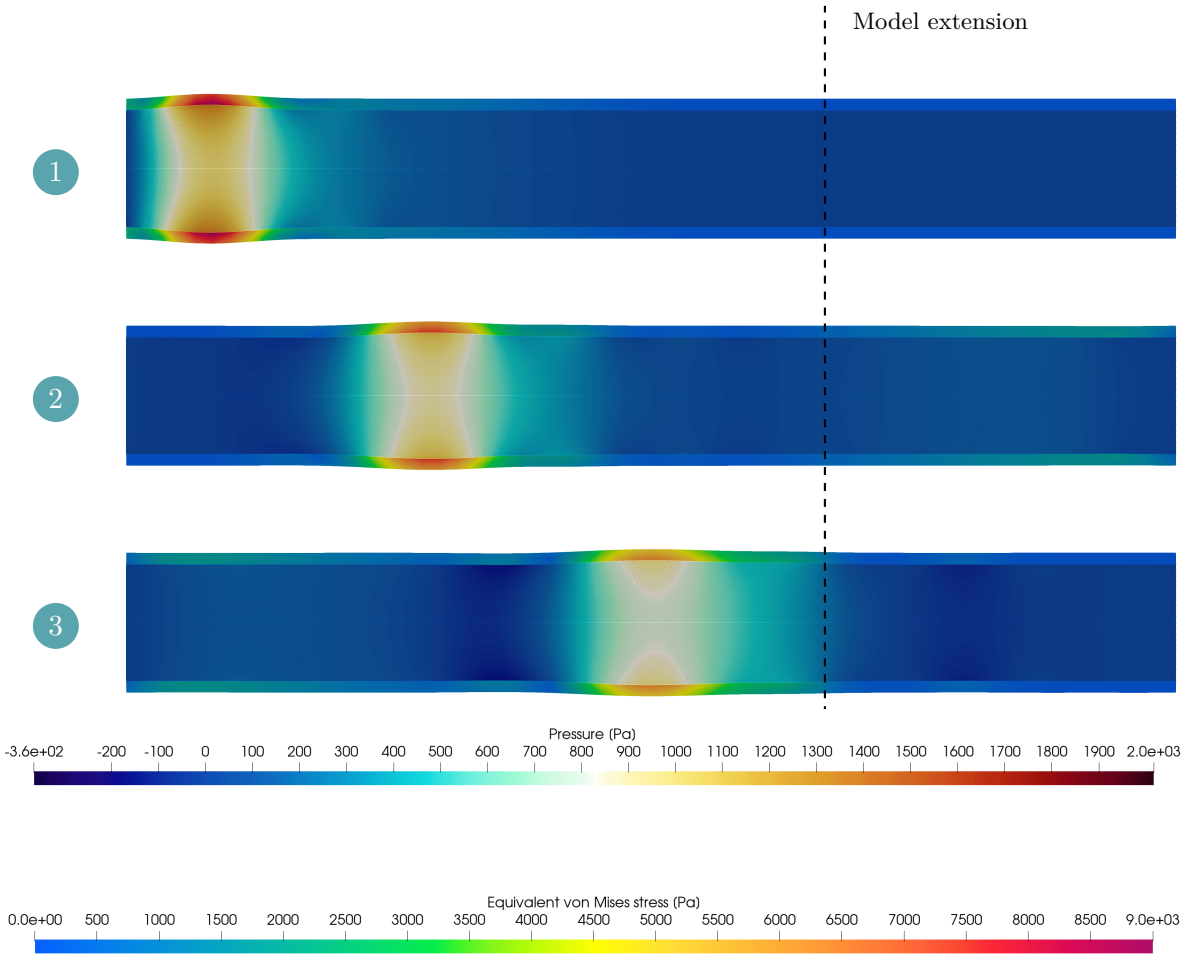

FIGURE 3.11 – Pressure (fluid) and equivalent von Mises stress (solid) in a radial plane at three different times: 1 $t = 5.0$ ms, 2 $t = 12.6$ ms, and 3 $t = 20.0$ ms.

A quantitative verification of the results can be obtained by comparing the computed wave speed with the estimate given by the Moens-Korteweg equation

$$c_0 = \sqrt{\frac{Et}{2\rho^f R}} \tag{3.39}$$

for the propagation of a pressure disturbance in a circular tube with wall thickness t and undisturbed radius R [181]. Using this equation and the parameters of the current numerical experiment in Tables 3.2 and 3.3, a wave speed of 3.09 m/s can be estimated (Note that this value is much lower than the expected physiological value on account of the reduced wall rigidity taken from Sun et al. [172] and used here for comparison purpose). This value compares reasonably well with the estimate of 2.85 m/s that can be obtained from Figure 3.12a by looking at the delay between the time of occurrence of the foot of the wave at the two locations. Note however that the theoretical and numerical estimates rely on different assumptions. The Moens-Korteweg equation (3.39) considers the idealized case of an infinitely long circular thin-walled artery with a homogeneous, incompressible, and non-viscous fluid. The artery wall is also considered to be a Hookean solid with small deformations. Although modeling assumptions differ, the fact that the two values are close to each other provides a quantitative verification of the numerical approach used to simulate the propagation of a pulse in a blood vessel.

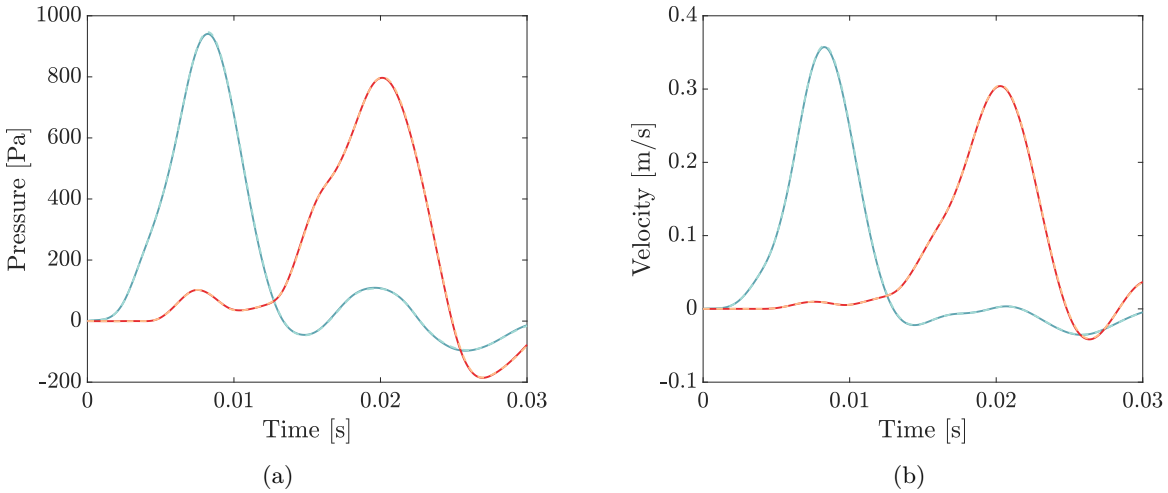

FIGURE 3.12 – Time series of pressure (a) and longitudinal velocity (b) at two points located on the symmetry axis at 1.5 cm (—/- - -) and 4.5 cm (—/- - -) downstream the upper boundary. Results are obtained with Casson (- - -) and Newtonian (—) fluid models.

Figures 3.12a and 3.12b show that the amplitude of the wave decreases as it progresses along the blood vessel. From a maximum amplitude of 2000 Pa at the inlet section at time 2.5 ms, the pressure peak is reduced to 938 Pa at $y = 0.015$ m, 5.9 ms later, and about 800 Pa further downstream at $y = 0.045$ m. This effect can be partly attributed to the smoothing effect of the finite discretization and numerical integration but is also directly related to the dissipation mechanism associated with the fluid viscosity and the no-slip boundary condition at the wall. The latter is not taken into account by the Moens-Korteweg equation which therefore predicts a constant pressure pulse.

Results are also shown for a Casson fluid (yield stress $\tau_y = 0.0035$ Pa and asymptotic dynamic viscosity $\mu_\infty = 0.0038$ Pa $\cdot$ s). Modeling blood either as a Newtonian fluid or a Casson fluid has however no noticeable influence on the results. This is due both to the high shear rate generated by the pressure pulse and its highly unsteady nature.

3.3.2 Realistic pulsatile flow in a straight artery.

To go further with the analysis of the blood flow in arteries and identify the appropriate constitutive model and numerical parameters for their simulation, we now introduce more realistic conditions that are explicitly related to the physiological values found in the real body.

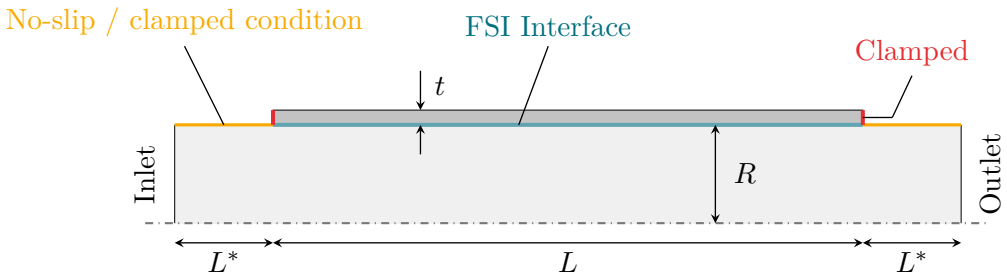

FIGURE 3.13 – Geometry of the axisymmetric straight artery with fluid domain ( ), solid domain ( ), and boundary conditions (clamped (—), FSI interface (—), and no-slip/clamped condition (—)). In essence, a no-slip condition is also prescribed at the FSI interface.

We still consider a straight segment of an artery as schematized in Figure 3.13 but use now the geometrical data in Table 3.4 and force the model with boundary conditions adapted from the literature. The velocity and pressure signals plotted in Figures 3.14 and 3.15 are obtained from clinical studies and can be considered as typical of the time evolution over the cardiac cycle of the physiological parameters in the infrarenal segment of the human abdominal aorta [118]. These waveforms describe a pulse repeating every 1 second (period $T = 1$ s). The peak systolic flow occurs at $t = 0.304$ seconds and outlet peak pressure at $t = 0.4$ seconds. They are used to force the model, respectively at the upstream and downstream boundaries of the fluid domain.

Parameters	*Values*	*Units*
Length L	6	cm
Length extension L^*	1	cm
Radius R	1	cm
Thickness t	0.15	cm

TABLE 3.4 – Geometrical parameters for the straight artery realistic simulations. The actual domain is extended upstream and downstream by 1 cm to avoid numerical artifacts and instabilities at the boundaries of the fluid domain.

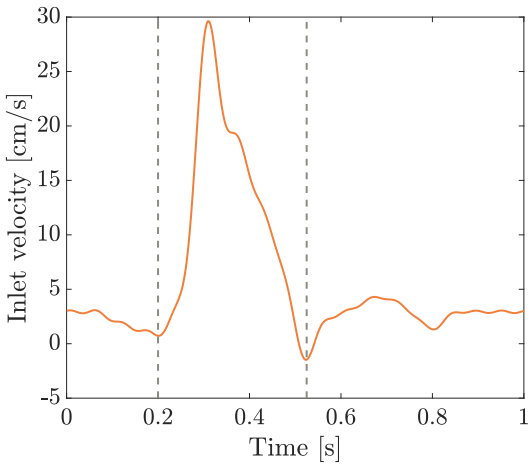

FIGURE 3.14 – Inlet velocity waveform reproduced from [118].

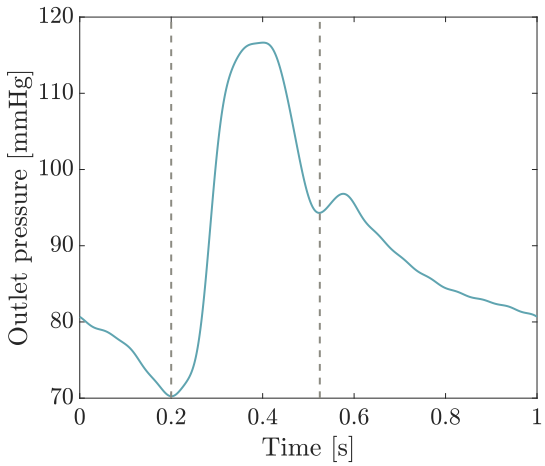

FIGURE 3.15 – Outlet pressure waveform reproduced from [118].

The pressure waveform can be divided into a systolic (between the two vertical dotted lines) and a diastolic part. The systole is the phase of the heartbeat where the heart muscle contracts. It relaxes during diastole. When the left ventricle ejects blood into the aorta, the aortic pressure rises. The maximal aortic pressure following ejection is termed the systolic pressure. Similarly, the velocity rises to a peak velocity of 30 cm/s. A small period of backflow, *i.e.,* with negative velocity, is then observed. It accompanies the aortic valve closing and is responsible for the rebound of aortic pressure observed in the pressure waveform, the dicrotic notch. This small increase of pressure typically defines the beginning of the diastolic phase, when the aortic valve closes. As the left ventricle is relaxing and refilling, the pressure in the aorta then falls. The lowest pressure in the aorta, which occurs just before the ventricle ejects blood into the aorta, is termed the diastolic pressure. In this study, pressure varies between a diastolic pressure of 70 mmHg and a systolic pressure of 115 mmHg (1 mmHg = 133.3 Pa). The velocity is close to zero during diastole [178].

The boundary data plotted in Figure 3.14 define the average value v_a across the inlet section. The actual velocity profile is prescribed as

$$v = 1.5 v_a (1 - \xi^4) \tag{3.40}$$

where $\xi \in [0, 1]$ is the relative coordinate measured from the symmetry axis. This profile is relatively flat but ensures that the velocity vanishes at the artery wall.

To feed the data into the model, the inlet velocity and outlet pressure data are digitized from the figures published by Mills et al. [118] using the WebPlotDigitizer tool[2]. They are then submitted to a Fast Fourier Transform to extract the dominant components and get periodic analytical expressions of the two signals. Accurate representations of the two time series can be obtained with 17 harmonics.

3.3.3 Numerical considerations.

Both the fluid and solid domains have a simple rectangular geometry. The fluid-structure interaction occurs along their common boundary. To avoid numerical artifacts associated with boundary conditions, 1 centimeter long (= one radius) buffer zones are added downstream and upstream the segment of interest. Fluid-structure interactions are not considered in these buffer zones and the boundaries of the arterial walls are fixed (no translation in any direction). This prevents the development of instability issues observed in preliminary numerical tests due to spurious interactions between the deformation of the arterial wall and the inlet and outlet sections where the boundary conditions are prescribed.

Blocking the two degrees of freedom in translation of the artery wall in the buffer region is motivated by numerical stability requirements, but is also justified from a physiological point of view. The arteries do not float freely in the body, but are attached to other tissues in the body, including the vascular nerves. This tethering occurs at different positions along the artery. This ensures the consistent functioning of the cardiovascular system. In particular, the movement and deformation of the aorta are reduced by the rigidification provided by the geometry of the aortic arch and its connection with the left ventricle, upstream, and by the branching with other arteries downstream [116].

The spatial discretization in the fluid domain is controlled by locally adjusting the characteristic size h of the PFEM elements. This reference value is gradually decreased by a factor of two as one approaches the fluid-structure interface, where the influence of the deformable wall is greatest and the velocity gradient reaches its maximum values.

The solid domain is discretized using a transfinite mesh of linear rectangular elements with up to 12 elements across the wall and 450 elements to capture the variation in stress state along the arterial segment. For instance, an initial mesh with 8 elements across the wall and 300 elements along the segment is found in Figure 3.16. The initial fluid domain is made of 5137 elements.

The model is integrated forward in time from zero initial conditions with a maximum time step of 0.1 ms. To avoid instabilities, the external forcing must be applied gradually. In particular, the brute application of the 80 mmHg output pressure would produce large oscillations and instabilities that the PFEM code (PFEM3D) would not be able to handle. Also, the 80 mmHg pressure cannot be included in the initial conditions because the artery wall would suffer from a similar problem. Instead, a gradual loading must be introduced. In practice, the inflow velocity is multiplied by a ramp function

$$f(t) = min(1, t/T_{trans}) \tag{3.41}$$

[2] `https://automeris.io/WebPlotDigitizer`

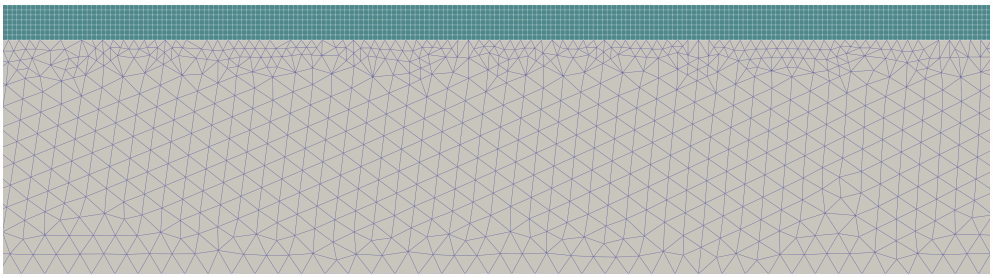

FIGURE 3.16 – Part of the initial mesh of the fluid and solid subdomains. The resolution in the fluid domain is increased along the interface.

that goes from 0 (no load) to 1 (full load) over the timescale $T_{trans} = 0.1$ s. A similar approach is used to initialize the pressure field. However, to avoid any non-physical backflow that can be induced during the initialization phase by the increase of the outlet pressure, this boundary value is not allowed to increase until a longitudinal pressure gradient has built up, and the ramp function (3.41) for the pressure field uses a longer timescale $T_{trans} = 0.3$ s.

The simulations are run for 2 cardiac cycles (2 s). The results to be analyzed are extracted from the second cycle.

Four different meshes are considered in a convergence study (Table 3.5). Both the number of PFEM nodes (*i.e.,* particles) and the number of finite elements in the artery wall are varied. Convergence is assessed against the blood velocity at the middle of the segment length on the symmetry axis, as well as the wall displacement, the equivalent von Mises stress, and the σ_{xy} stress at the point at the middle of the artery wall on its inner surface (Note that the σ_{xy} component of the stress tensor at this point is indicative of the wall shear stress but, as explained in Appendix B, cannot be used to compute the shear stress actually sensed by endothelial cells.). All the results are extracted at time $t = 1.4$ s, corresponding to the peak systolic pressure. The simulation time reported in Table 3.5 are on 2 nodes of a PC with an Intel Core i7-4790 CPU running at 3.60 GHz.

Fluid elements	*Solid elements*	h [cm]	*Velocity* [cm/s]	σ_{xy} [Pa]	σ_{VM} [MPa]	*Wall displacement* [mm]	*CPU time* [s]
5128	1120	0.10	14.06	66.00	0.146	1.221	3116
5137	2093	0.08	14.03	64.06	0.147	1.219	4052
8854	2093	0.08	14.00	65.36	0.147	1.216	10 075
28063	4939	0.04	13.97	65.42	0.147	1.217	29 268

TABLE 3.5 – Convergence study. Displacement and stresses are computed at the interface between the fluid and the solid domains, at the middle of the artery, at time $t = 1.4$ s of the peak systolic pressure.

The results in Table 3.5 show the rapid convergence for the wall displacement and the equivalent von Mises stress. The shear stress and the point value of the velocity are more sensitive to the number of solid and fluid elements. Even if some parameters are more sensitive than others, we can nevertheless state that reliable, mesh-independent results can be obtained with the various models considered. As the computation time increases considerably with the resolution of the models, with little influence on the results, the parameters of the second model in Table 3.5 are used in the following studies.

3.3.4 Analysis of the flow in a straight artery.

The results of the nominal simulation using the parameters listed in Table 3.6 provide insight into the blood flow in the upper aorta and in the larger arteries. In this nominal simulation, the fluid is Newtonian and the arterial wall is modeled as a Hookean solid.

Parameters	*Values*	*Units*
Fluid density ρ^f	1050	kg/m^3
Dynamic viscosity μ	0.0038	Pa · s
Arterial wall density ρ^s	1200	kg/m^3
Arterial wall Young's modulus E	0.675	MPa
Arterial wall Poisson's ratio ν	0.45	-

TABLE 3.6 – Material parameters for the straight artery realistic simulations.

Figure 3.17 shows some snapshots taken at different characteristic moments of the cardiac cycle.

At the end of diastole, Cauchy stresses in the arterial wall and wall deformation are at their minimum. These are different from zero because the internal pressure is not zero, but at the diastolic pressure of 70-80 mmHg (1).

The rapid increase in pressure pushes the flow into the artery in a pulsatile manner. A maximum velocity of more than 40 cm/s is then observed along the axis of the blood vessel (2). The deformation of the arterial wall closely follows the time evolution of the blood pressure. Therefore, the maximum displacement of about 2.3 mm is observed at the peak systolic pressure, together with the maximum internal stresses in the walls. This value of the wall displacement, of the same order of magnitude as the thickness of the wall itself (1.5 mm), is in agreement with the results reported by Balzani et al. [8] and Barnett et al. [9].

At the moment of the dicrotic notch, the pulse is in a rapid deceleration phase. While blood is still flowing toward the various organs in the center of the artery, though at a much slower rate, a small backflow develops along the arterial walls (3).

During diastole, the flow continues to decrease and the velocity is only a few centimeters per second. The pressure also steadily decreases, along with the deformation of the arterial wall and the internal stresses (4).

Figure 3.18 shows the velocity profiles across the center of the segment at 10 consecutive times. While a few of these profiles show the typical parabolic distribution of the fully developed Poiseuille flow, most of them differ significantly from this classical profile. This deviation from the Poiseuille flow reflects the unsteadiness of the flow.

The parabolic Poiseuille profile appears when the pressure gradient is balanced by viscous forces. In an unsteady flow, however, one must also consider the ratio of the unsteady inertia to viscous effects. This can be quantified using the Womersley number α

$$\alpha = \sqrt{\frac{\rho^f R^2 \omega}{\mu}} \tag{3.42}$$

where ω is the angular frequency of the oscillatory motion and R is the undeformed radius of the artery [65]. The Womersley number compares the characteristic time associated with diffusion to the period T of pressure variations. It is related to the Reynolds number, Re, and the Strouhal number, St, by

$$\alpha = \sqrt{2\pi StRe} \tag{3.43}$$

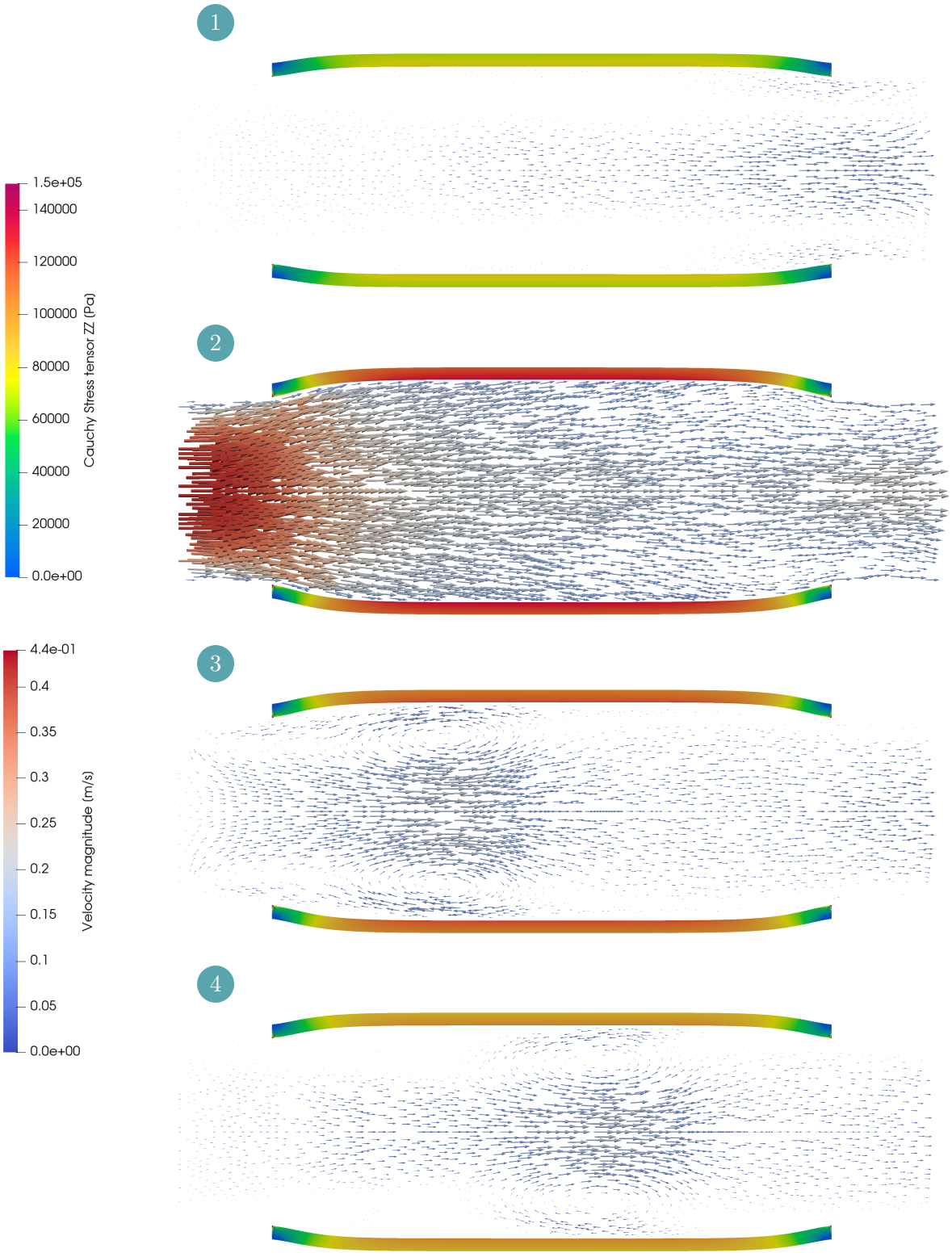

FIGURE 3.17 – Velocity profiles and artery wall deformation at four characteristic moments of the cardiac cycle: 1 end of diastole ($t' = t - T = 0.20$ s), 2 systole velocity peak ($t' = 0.30$ s), 3 beginning of diastole (dicrotic notch, $t' = 0.55$ s), and 4 diastole ($t' = 0.80$ s).

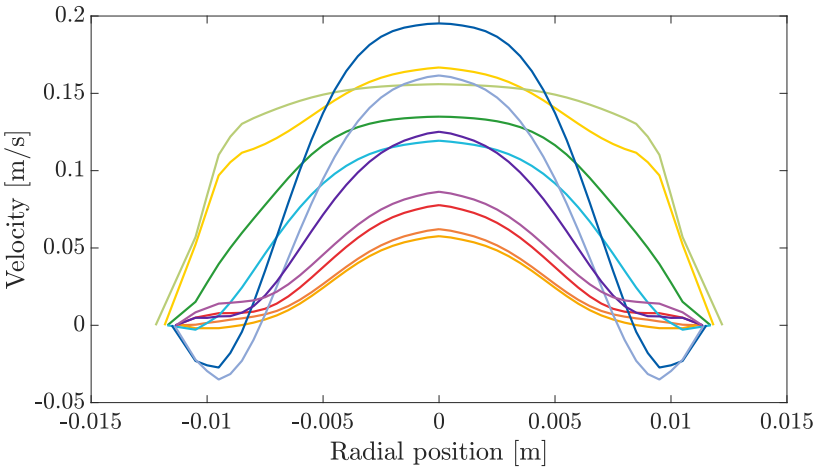

FIGURE 3.18 – Velocity profiles across the midsection of the straight artery at $t' = t - T = 0.0$ s (—), 0.1 s (—), 0.2 s (—), 0.3 s (—), 0.4 s (—), 0.5 s (—), 0.6 s (—), 0.7 s (—), 0.8 s (—), 0.9 s (—), and 1.0 s (—).

Using the parameters of the straight artery simulations, a value of 13.18 is found, which is typical for the human abdominal aorta under resting conditions [193]. Such a large value of Womersley implies that the dominant balance in the fluid is not between the pressure and viscosity terms, but between inertia and pressure gradient. For such large values of the Womersley number, the velocity profiles are flatter, the flow rate decreases, the oscillations of the flow in the center of the pipe lag behind those at the walls, and the velocity profiles during flow reversal exhibit local maxima that are off-center.

The Cauchy stresses are also worthy of careful analysis. Figure 3.19 shows the time series of relevant statistics in the artery wall. These statistics are computed at the interface between the fluid and solid domains, in the central part of the segment, where the displacement is only radial.

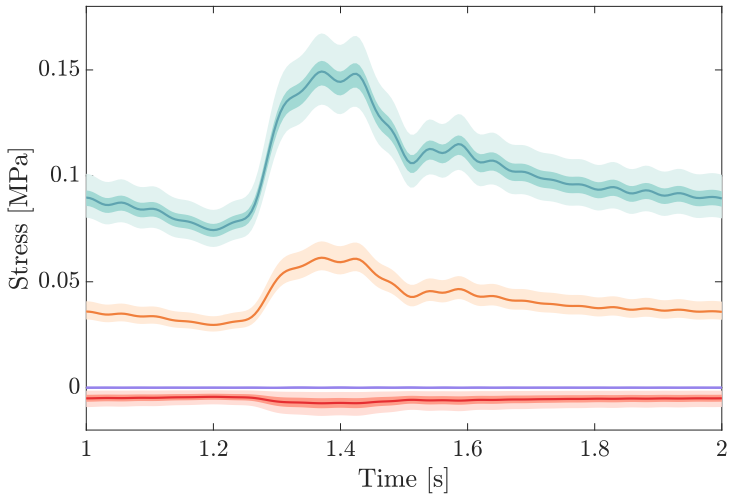

FIGURE 3.19 – Variation of the components of the Cauchy stress tensor during the second cardiac cycle (σ_{zz} (—), σ_{yy} (—), σ_{xx} (—), and σ_{xy} (—)), as computed in the central part of the artery segment. Values are represented by the average value (—), the first and third quantiles (■), and minimum and maximum (■).

The largest Cauchy stresses are in the azimuthal direction. Using the thin-wall assumption and linear elasticity theory, these hoop stresses would be approximated as

$$\sigma_{zz} = \frac{pR}{t} \tag{3.44}$$

which would result in a peak hoop stress of about 0.1 MPa. In the simulated results, the Cauchy peak hoop stress is about 50% larger, which can be attributed to the deformation of the artery wall, which is responsible for both an increase in the actual radius and a decrease in the wall thickness, and to inertial effects, since the fluid and the artery wall have about the same density. A careful analysis of the model results also shows that, contrary to the assumption behind (3.44), the hoop stresses are not constant but vary linearly across the wall. The difference between the results of the linear thin-wall theory and the computed value illustrate the significance of nonlinear effects in this simple set-up. The discrepancy between the figures computed using the two approaches decreases significantly when considering the results at the end of diastole. The computed mean hoop stress then reaches 0.075 MPa, while the corresponding estimate using (3.44) is 0.062 MPa.

The second most important component of the Cauchy stress tensor is the longitudinal stress σ_{yy}. This takes a mean value of about 0.04 MPa. It also varies much less during the cardiac cycle. The longitudinal stress appears because the two extremities of the artery segment are fixed to the neighboring segments and cannot therefore move freely, while the deformation of the straight artery under the internal pressure produces a net longitudinal force.

The radial component of the Cauchy stress tensor σ_{xx} simply balances the internal pressure on the artery wall and varies accordingly between this value on the inner surface of the wall to zero at its outer surface.

Finally, a very small component of the shear stress σ_{xy} is hardly noticeable in Figure 3.19. Despite its small value, this parameter has important physiological implications. This is indeed a predictor of atherosclerosis and risk of aneurysm rupture. The analysis of the wall shear stress is therefore deferred to a specific section.

3.3.5 Wall shear stress and atherosclerosis.

Atherosclerosis is a chronic inflammatory disease of the arteries and is the underlying cause of about 50% of all deaths in westernized society [132]. Atherosclerosis is when plaque, a sticky substance made of cholesterol, fatty substances, calcium, collagen fibers, and other materials, builds up inside the walls of the arteries. This affects the intima, *i.e.,* the inner layer of the blood vessel.

Plaque progression and eventually plaque rupture is influenced by a complex interaction between biological and hemodynamic factors: the initiation of plaque formation has been strongly linked to the wall shear stress [100, 119]. Endothelial cells are indeed sensors of the frictional force exerted by blood flow. Low WSS modulates endothelial gene expression through complex mechanotransduction processes that promote lipid accumulation and oxidation, inflammatory cell infiltration, smooth muscle cell proliferation, and extracellular matrix production [30, 127]. The consequence of this accumulation of lipid molecules and inflammatory cells at specific locations within the wall may result in heart attack. The uneven surface of the arteries may also result in blood clot formation and thrombosis, which leads to the sudden obstruction of blood flow. The rupture of atherosclerotic plaques is also known to cause heart attacks and strokes.

The direct measurement of wall shear stress in a blood vessel within the body is impossible, although pathologically low WSS is a major risk factor for initiation and progression of atherosclerosis. Therefore, the use of computer simulations to access this parameter could open the way to promising early diagnosis of plaque formation.

The low and/or oscillatory WSS hypothesis has become the consensus mechanism for the initiation of atherosclerosis. Two related parameters are often reported in literature to assess the risk of atherosclerosis, namely the *Time-averaged Wall Shear Stress* (T-WSS) and the *Oscillatory Shear Index* (OSI) [26, 202]. The T-WSS is obtained by integrating the WSS magnitude over the cardiac cycle

$$\text{T-WSS} = \frac{1}{T}\int_0^T |wss(t)|dt \tag{3.45}$$

while the oscillatory shear index

$$\text{OSI} = \frac{1}{2}\left[1 - \frac{\left|\int_0^T wss(t)dt\right|}{\int_0^T |wss(t)|dt}\right] dt \tag{3.46}$$

is a non-dimensional parameter measuring the directional change of WSS during the cardiac cycle. Wall cells with a low T-WSS and large OSI (*i.e.,* with highly oscillating WSS directions) are prone to lesion development. Prior research reported in particular that T-WSS values less than 0.4 Pa can result in plaque buildup in the arterial wall and stimulates an atherogenic phenotype while T-WSS above 1.5 Pa induces endothelial quiescence and an atheroprotective gene expression profile [112]. When the disease has started, however, plaques will begin to invade the lumen and affect local hemodynamics. Upon further progression of plaques, high WSS is associated with the formation of vulnerable/unstable plaque. It promotes the transformation of plaque to high-risk phenotype [209]. Low WSS and high WSS are therefore both involved in the occurrence and development of atherosclerosis.

Figure 3.20 shows the spatial distribution of both the time-averaged and maximum wall shear stress along the considered segment of the aorta. It is important to note that accurately computing this parameter requires an extensive treatment of the fluid model results, as detailed in Appendix B.

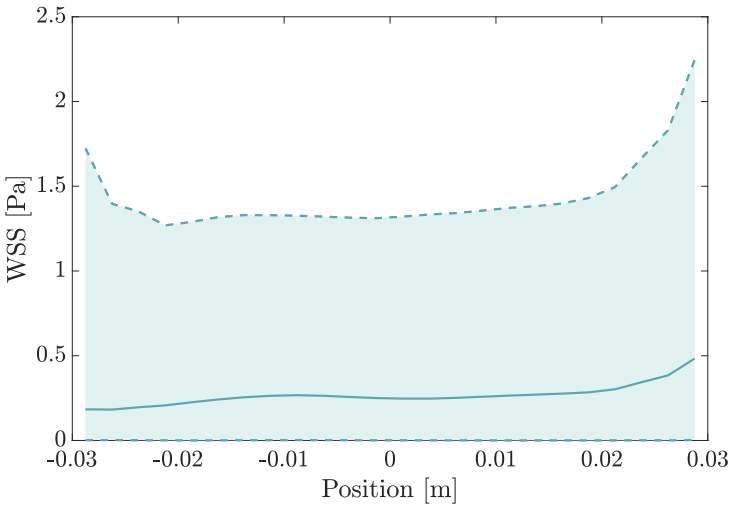

FIGURE 3.20 – Time-averaged WSS (——), range of variation (■), and minimum and maximum values along the artery segment (- - -).

While the maximum values fall within the healthy range for an individual, the time-averaged wall shear stress index is slightly lower than the range typically expected to inhibit plaque formation (0.4 Pa $<$ T-WSS $<$ 7 Pa) [112]. Our results are however similar to those reported by

Scotti et al. [155]. The relatively small WSS value may be due to the simplified geometry employed in this analysis. In a perfectly straight artery, the wall shear stress necessary to force the velocity profile to adapt to the geometric constraints is small. More realistic geometries featuring variable curvature and full three-dimensional effects are anticipated to yield higher WSS values. Conversely, the lack of tortuosity of the current simulation adversely impacts the T-WSS index. This preliminary conclusion is supported by the observation that WSS increases near the outlet of the artery segment, where there is a slight increase in the curvature of the artery wall (Figure 3.17). This phenomenon is even more marked at the systolic peak, where the wall deformation is greatest, causing the instantaneous WSS to rise above 2 Pa.

3.3.6 Influence of the material parameters.

As explained in the first sections of this chapter, different options are available and are commonly used to model the behavior of blood and of the artery wall. In this section, we analyze the influence of the constitutive laws through the different runs described in Table 3.7. In particular, the different simulations give insight into the influence of the arterial stiffness, which is an important parameter for the dynamics of the cardiovascular system. Stiffening is known to contribute significantly to cardiovascular diseases in older individuals and is positively associated with systolic hypertension, coronary artery disease, stroke, and heart failure, which are the leading causes of mortality in the developed countries [160]. The influence of the constitutive model is also considered. Models of increasing complexity (Linear elastic, Neo-Hookean, Mooney-Rivlin) are used to model the artery wall. The effect of the fluid assumption is also studied (Casson *vs.* Newtonian fluid).

Note that negative coefficients in the Mooney-Rivlin hyperelastic energy density function can lead to instability problems but are nevertheless sometimes reported in the literature [101, 188]. Our results for the $R5$ simulation do not exhibit such problems.

Name	*Type of solid*	*Young's Modulus [MPa]*	C_1 *[MPa]*	*Type of fluid*
$R1$ (——)	Linear elastic	0.675	/	Newtonian
$R2$ (——)	Linear elastic	1	/	Newtonian
$R3$ (- - -)	Linear elastic	100	/	Newtonian
$R4$ (- - -)	Linear elastic	0.675	/	Casson
$R5$ (——)	Mooney-Rivlin	0.675	-20	Newtonian
$R6$ (- - -)	Mooney-Rivlin	0.675	10	Newtonian
$R7$ (——)	Neo-Hookean	0.675	/	Newtonian

TABLE 3.7 – Constitutive laws and parameters used to analyze the influence of the material parameters. The Poisson's ratio is kept at $\nu = 0.45$ in all the simulations.

Figure 3.21 shows the displacement of the arterial wall at the center of the artery as a function of time during the second of simulated heartbeats. Note that the displacement is defined with respect to the unloaded situation with zero internal pressure in the artery. The obvious conclusion is that the choice of constitutive model has no significant effect on the deformation of the artery wall when the constitutive models are consistent with each other. Of course, this is expected since the deformation of the artery wall is moderate, *i.e.,* a displacement of 2.3 mm at most (for an initial radius of 1 cm), and the models are built to behave in the same way in the linear regime.

Varying the Young's modulus does however have a large influence on the displacement of the artery wall. Changing the Young's modulus from the reference value of 0.675 MPa ($R1$) to 1 MPa ($R2$) decreases the maximum displacement from 2.29 mm to 1.30 mm, which is more than the ratio of the Young's moduli. Of course, the displacement of a nearly rigid wall ($R3$) is close to zero.

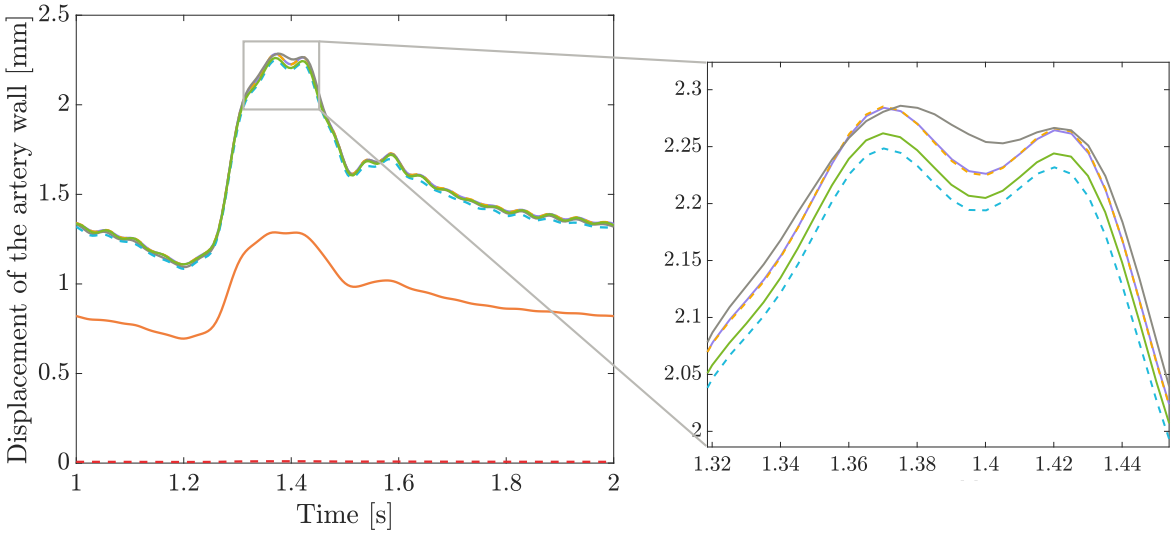

FIGURE 3.21 – Evolution of the displacement of the artery wall at the middle of the artery segment for the constitutive laws detailed in Table 3.7 ($R1$ (—), $R2$ (—), $R3$ (- - -), $R4$ (- - -), $R5$ (—), $R6$ (- - -), and $R7$ (—)).

A close examination of the displacement curve at the moment of peak systolic pressure (Figure 3.21) reveals minor, not really significant, differences among the models with identical equivalent Young's modulus. The maximum deformation with the linear model $R1$ occurs at $t - T = 0.37$ s and is 2.293 mm. For the same shear modulus, the wall deformations predicted by the Neo-Hookean ($R7$) and Mooney-Rivlin models ($R5/R6$) are 2.270 mm and 2.296/2.260 mm, respectively. The difference between all these models is less than 2%. The solutions computed with the two versions $R5$ and $R6$ of the Mooney-Rivlin model display the largest differences and form the envelope of the different results. Except for the Mooney-Rivlin model with a negative C_1 coefficient ($R5$), all the models show the same time series with a small, nearly constant vertical offset.

These observations are perfectly in line with the conclusions of Kallekar et al. [93] who analyzed the effect of the constitutive model on deformation during flow in a coronary artery.

The influence of the constitutive law on the von Mises stress is also not of major influence, with the Neo-Hookean slightly overestimating the von Mises stress compared to other models (Figure 3.22). Again, the largest influence comes from the stiffness of the artery wall, with the two more rigid models yielding to smaller values. For the kind of simulations considered here, it is therefore clear that the accurate quantification of the Young's modulus of the arterial material is definitely more important than the choice of the constitutive model.

The analysis does not reveal any significant difference if blood is modeled as a Newtonian or Casson fluid. This means that in large arteries (diameter of 2 cm), the assumption of a Newtonian fluid is valid. This is due both to the high shear rate in such a flow and to its highly unsteady nature. As mentioned above, viscosity terms play only a secondary role here, as long as the Womersley number is large.

The exact material parameters have a significant influence on the wall shear stress and the T-WSS index discussed in section 3.3.5 (Figure 3.23). The choice between a Newtonian or Casson model has little influence, in contrast to the constitutive model of the arterial wall. In section 5.2.6, we will show however that this partial conclusion does not extend to more complex geometries.

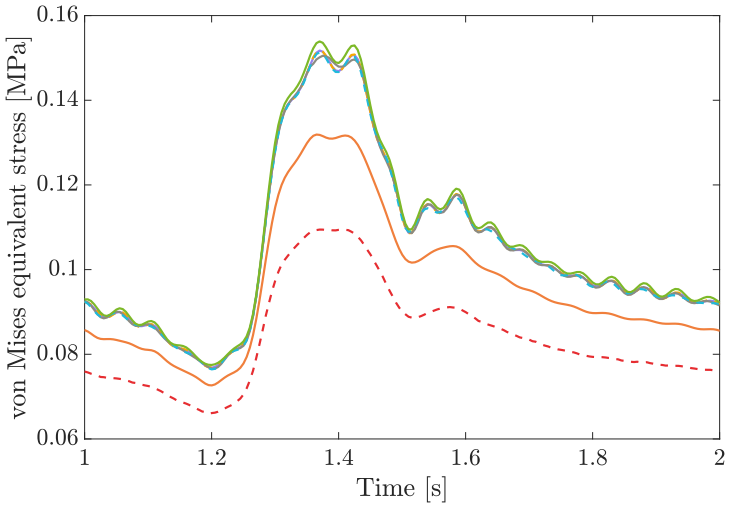

FIGURE 3.22 – Evolution of the von Mises equivalent stress at the middle of the artery segment for the constitutive laws detailed in Table 3.7 ($R1$ (—), $R2$ (—), $R3$ (- - -), $R4$ (- - -), $R5$ (—), $R6$ (- - -), and $R7$ (—)).

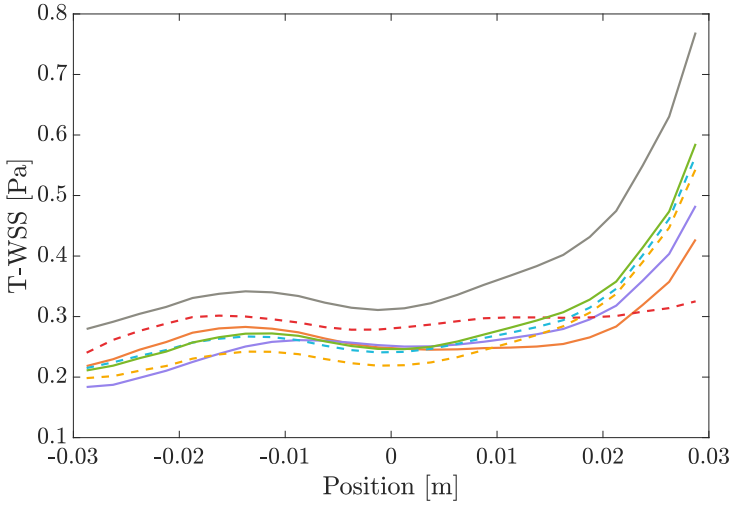

FIGURE 3.23 – T-WSS along the artery segment computed with the constitutive laws detailed in Table 3.7 ($R1$ (—), $R2$ (—), $R3$ (- - -), $R4$ (- - -), $R5$ (—), $R6$ (- - -), and $R7$ (—)).

With the exception of the most rigid model $R3$, the other models show spatial variations of the T-WSS index that are similar to those discussed previously (Figure 3.20). Overall, the mean values are below the expected threshold of 0.4 Pa, despite a significant increase as the outlet section is approached. Among all the models, $R5$ stands out for its higher T-WSS values. In particular, the two Mooney-Rivlin model parameter choices introduced in models $R5$ and $R6$ lead to different values of T-WSS, even though they gave rise to similar internal stresses and displacements. In the absence of experimental data to validate one choice over the other, it therefore seems reasonable to consider that the choice of arterial wall constitutive model can significantly influence the calculation of WSS and therefore the assessment of the propensity to develop an atherosclerosis problem if this parameter is used for diagnostic purposes. Further investigation of these issues, in more complex geometries and with extensive experimental data, is however required before reaching meaningful conclusions. The potential influence of numerical

implementation details should also be investigated. The different models differ indeed by the way the stiffness matrix of the finite element formulation is computed, with an analytical derivation used for all the models except Mooney-Rivlin, for which a perturbation method is used.

3.4 Typical flow in a vein.

The results of the previous sections show that blood in larger arteries behaves as a Newtonian fluid and that there is no need to resort to a Casson type constitutive equation. In fact, the viscosity of blood decreases with increasing shear rate until reaching an asymptotic value for shear rates above about 100 s^{-1}. In most computational hemodynamic studies, such high shear rates are commonly reached and blood can be modeled as a Newtonian fluid with a viscosity equal to its asymptotic value [6]. In addition, the unsteadiness of the flow also plays an important role, since viscosity effects, and thus the distinction between Newtonian and Casson models, are hardly relevant in a pulsatile flow with a large Womersley number.

To illustrate a situation in which the Casson model is relevant, we consider here the flow in the Inferior Vena Cava (IVC). The IVC is the largest vein of the human body. It is located at the posterior abdominal wall. The lack of pulsatility plays a double role here. On the one side, the flow remains nearly constant so that the Womersley number takes a small value. On the other side, the transport of a given flow rate at a nearly constant rate requires smaller velocity, which creates smaller shear rates [6].

The human inferior vena cava geometry can be simplified as a straight tube with a slightly thinner wall than that of an artery. The geometrical parameters are summarized in Table 3.8. As depicted in Figure 3.24, the inlet velocity maximum and minimum values, measured via in vivo magnetic resonance imaging by Cheng et al. [31], vary only by a factor of two. The pressure wave from the heartbeat experiences significant damping upon reaching the capillary beds, resulting in the IVC operating at a nearly constant pressure of 5 mmHg.

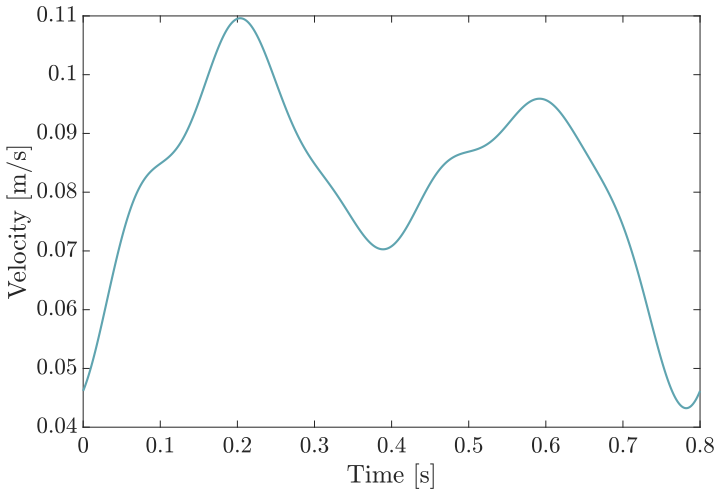

FIGURE 3.24 – Inlet velocity in the IVC as a function of time. The period of the cardiac cycle is $T = 0.8$ s.

The simulations are carried out following the same approach as in section 3.3.3 using either a Newtonian or a Casson constitutive equation. The inlet velocity profile is assumed to be uniform. The walls of the vein are modeled as a linear elastic material with a Young's Modulus of 1.25 MPa to account for the larger rigidity of the walls of the IVC [20]. The material parameters of the

Parameters	*Values*	*Units*
Length L	14	cm
Radius R	1	cm
Thickness t	0.12	cm

TABLE 3.8 – Geometrical parameters for the IVC simulations.

different simulations are summarized in Table 3.9. The results are extracted during the second of the two simulated cycles.

Parameters	*Values*	*Units*
Fluid density ρ^f	1050	kg/m^3
Dynamic viscosity μ (Newton model)	0.0038	Pa · s
Asymptotic dynamic viscosity μ_∞ (Casson model)	0.0038	Pa · s
Yield stress τ_y (Casson model)	0.0035	Pa
Venous wall density ρ^s	1200	kg/m^3
Venous wall Young's modulus E	1.25	MPa
Venous wall Poisson's ratio ν	0.45	-

TABLE 3.9 – Material parameters for the IVC simulations.

The velocity profiles in the IVC are plotted in Figure 3.25. The results are qualitatively similar to those of the analytical study carried out in section 3.1. While the simulations carried out using the assumption of a Newtonian fluid show the typical parabolic profile, the results for the Casson fluid do not show a well-defined velocity maximum at the center of the vein, but rather a zone where the velocity is nearly constant.

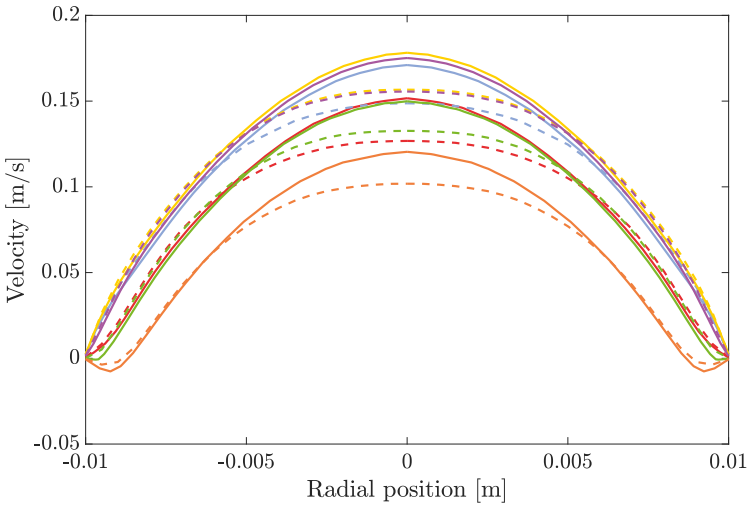

FIGURE 3.25 – Velocity profiles in the IVC at $t' = t - T = 0.40$ s (——), 0.48 s (——), 0.56 s (——), 0.64 s (——), 0.72 s (——), 0.80 s (——). Comparison between Casson (- - -) and Newtonian fluid models (——). Results are taken across the undilated section of the vein, 2 cm before the outlet.

The shear rates can be extracted from the model results using the ParaView `Compute Gradient` filter[3]. Due to the linear interpolation of the velocity field inherent to the PFEM, the velocity gradient is constant over each element, producing the mean staircase distribution shown in Fig-

[3]See `www.paraview.org`.

ure 3.26a. The results, which are similar to those reported by Cheng et al. [31], explain why a Casson model is relevant for the modeling of the flow in the IVC: the mean shear rate is everywhere significantly smaller than the 100 s^{-1} threshold for neglecting the yield stress and the shear thinning behavior of blood.

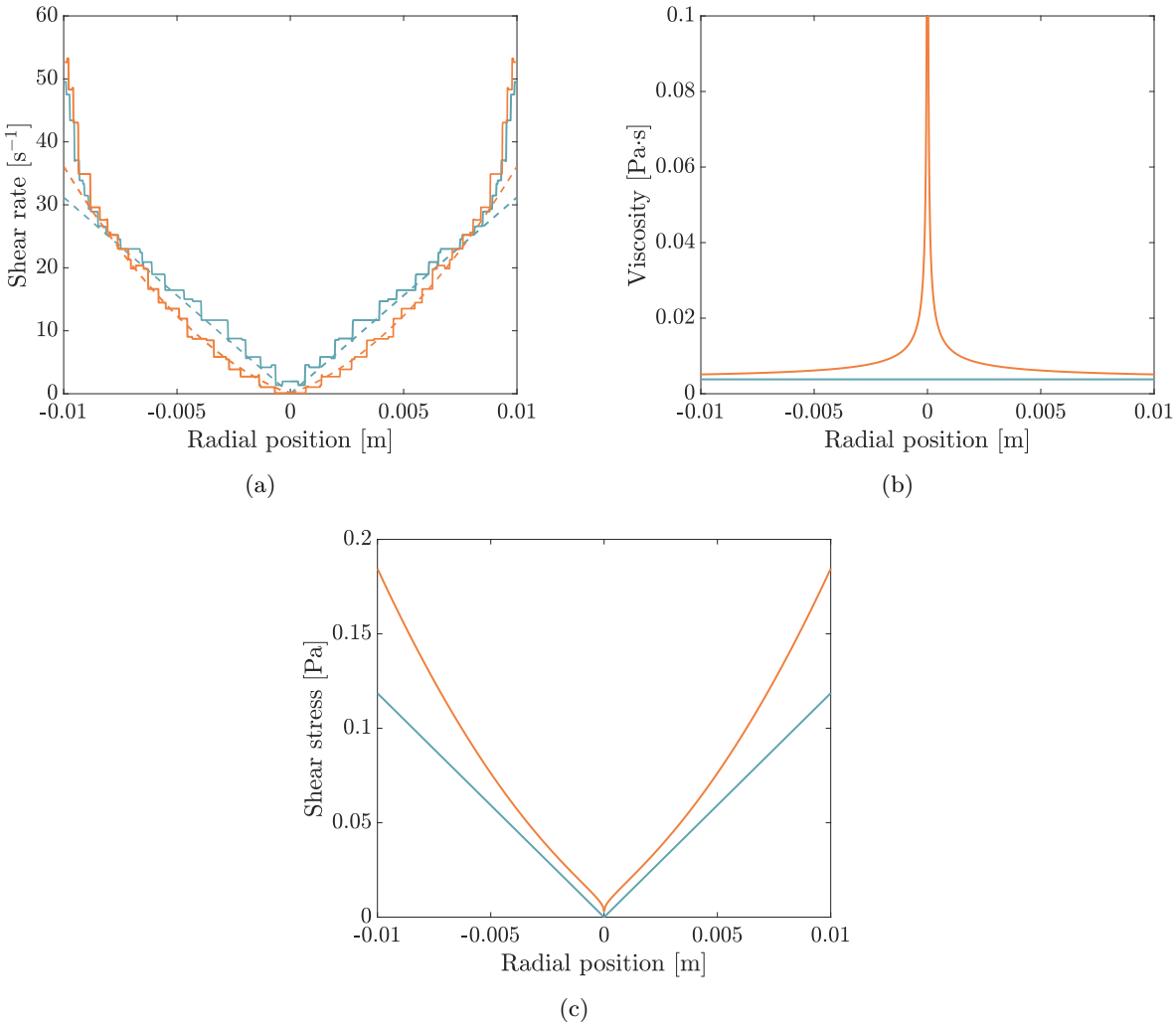

FIGURE 3.26 – Mean shear rate in the IVC (a), reconstructed mean viscosity in the IVC (b), and reconstructed mean shear stress in the IVC (c) using either a Newtonian (——) or a Casson (——) fluid model. Results are taken across the undilated section of the vein, 2 cm before the outlet, at $t' = t - T = 0.555$ s.

The staircase numerical data can be approximated by polynomial functions (dotted curves in Figure 3.26a). While the shear rate for a Newtonian fluid varies linearly with the radial distance (- - -), the corresponding distribution for the Casson fluid is better approximated with a cubic function (- - -). The two curves can be used to estimate the viscosity (Figure 3.26b) and shear stress (Figure 3.26c) corresponding to the two models. The viscosity of the Casson model is definitely larger than the constant viscosity of the Newtonian approximation, especially in the central section. This larger viscosity is large enough to compensate for the smaller shear rate shown in Figure 3.26a. As a result, the Casson model produces a significantly higher shear stress. In particular, where the wall shear stress matters, it is therefore important to rely on the right constitutive model and use a Casson model when appropriate.

CHAPTER 4

AORTIC VALVE

4.1 Modeling of the aortic valve.

Cardiac valves play a crucial role throughout the cardiac cycle as they ensure the one-way flow of blood to and from the heart. Valves are passive structures that react to the dynamic pressure variations created by the heart muscle contractions. Specifically, the aortic valve, situated between the left ventricle and the aorta, controls the ejection of oxygen-rich blood from the heart and prevents it from flowing back into the left ventricle [145].

The aortic valve has a semilunar shape and usually comprises three leaflets, which are thin cusps connected to the aortic root (Figure 4.1). The primary sealing function of the valve is provided by the complete coaptation of the three leaflets during diastole, effectively separating the ascending aorta from the left ventricle. The leaflets tissue features a layered structure (ventricularis, fibrosa, and spongiosa) and contains collagen fibers that are circumferentially aligned, leading to an anisotropic mechanical response [73].

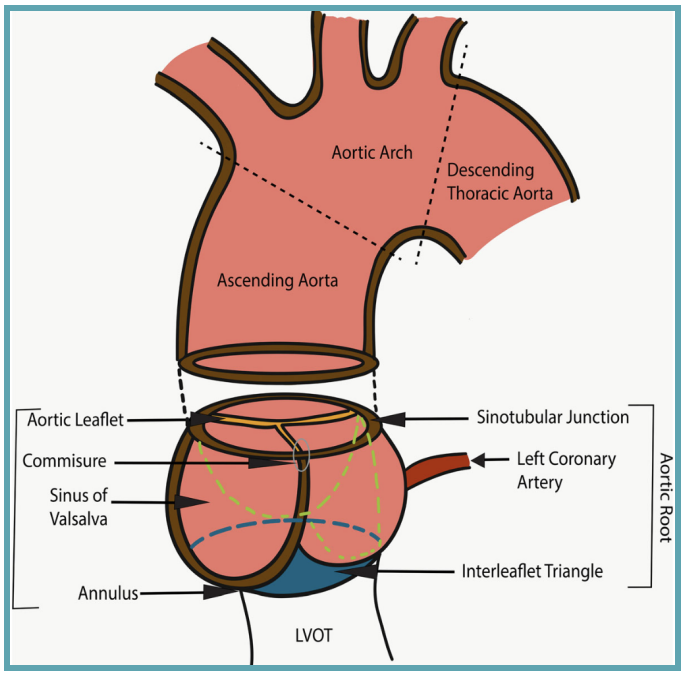

FIGURE 4.1 – Anatomy of the aortic root. Reproduced from Napgal et al. [126].

The aortic root refers to the anatomical bridge between the left ventricle and the ascending aorta. The three bulges of the aortic wall are named the sinuses of Valsalva. Two of the three sinuses host the origin of the coronary arteries [29]. The vortices created in the sinuses are thought to contribute to stress reduction on the aortic leaflets and to minimize the systolic pressure drop across the aortic valve. The sinuses also serve as a support structure for the aortic valve and provide space behind the valve leaflets when the leaflets are open during systole so that they do not occlude the coronary ostia (ostia = opening) [40]. The distal part of the sinuses toward the ascending aorta forms a tubular structure called the sinotubular junction, which separates the aortic root from the ascending aorta.

4.1.1 State-of-the-art on aortic valve modeling.

Numerical modeling is emerging as a valuable tool for accessing physiological parameters that are not directly measurable or observable. It can be used to assess heart valve performance in healthy and pathological conditions, facilitate pre-operative planning, develop new designs for replacement valves, and analyze blood flow patterns to guarantee the same functioning of the valve.

FSI-based heart models have been created to precisely simulate the complex motions of heart valves as they open and close, capturing the fluid dynamics within the heart chambers. Fluid-Structure Interaction (FSI) is particularly appropriate for modeling the dynamics of both native and prosthetic heart valves, given the mutual dependence between the movement of the valves and the pressure and flow fields within the heart chambers [77]. This interaction is vital, as the hemodynamics are affected by the condition of the valves, and conversely.

Gao et al. [61] developed a FSI model of the full cardiac cycle, including valve features, left ventricle contraction, nonlinear structural mechanics of valves, and the interaction of the fluid, ventricular wall, and valve. Some modeling studies focus on the aortic valve and consider the effects on the downstream large arteries: Hasan et al. [72] for instance successfully created a patient-specific FSI model of aortic root and ascending aorta to be used to plan valve repair or replacement surgeries. Fedele et al. [51] also created a model of the aorta that included the valve. Cao et al. [25] published a study investigating the contribution of coronary blood flow to aortic valve dynamics. Their results indicate that coronary flow decreases vortex development and affects the Wall Shear Stress (WSS) distributions.

Several other studies aim at determining the causes of heart valve stenosis and the response of valves to calcium buildup. Sadeghpour et al. [146] studied flow through a stenotic aortic valve and found that the low orifice area resulting from incomplete aortic valve opening causes a jet of fluid with high blood stresses. Cai et al. [19] also studied the mechanics of calcified aortic valve stenosis. Their results show significant changes in valve elasticity, mobility, and orifice area due to calcification, leading to changes in flow patterns.

Gharaie et al. [63] studied the nonlinear deformation of polymeric aortic valves using FSI. The valve leaflets are very flexible, hence it is essential to study the leaflet motion as well as the fluid dynamics of the complex flow through the valve. Research on bileaflet mechanical heart valves and associated complications, such as valve dysfunction, tissue overgrowth, and thromboembolism also employ FSI techniques. FSI techniques have, for instance, been used to simulate leaflet motion and investigate the role of vorticity in platelet activation. Hedayat et al. [75] looked at the effect of leaflet gap size of mechanical prosthetic heart valves on this mechanism. Their results show that a larger gap leads to higher total activation, but also improved washout ability due to increased flow velocity.

FSI models are also used to study the effects and dynamics of congenital bicuspid aortic valves. Cao et al. [24] published studies in this area, determining the WSS profile and leaflet deformation

of normal tricuspid aortic valves and bicuspid ones, and also investigating aortic dilation: bicuspid aortic valves result in abnormal aortic hemodynamics in areas with high dilation risk.

Although the intraventricular flow is three-dimensional by nature, it is a real computational challenge to describe the complex geometry of the flow and its interaction with the heart valves. Therefore, most numerical studies of aortic valve dynamics use simplified geometries, often with a 2D description of the aortic root, leaflets, and sinuses of Valsalva. Sometimes the sinus component includes a portion of the ascending aorta and the two coronary arteries [97]. Although two-dimensional approaches may not be realistic enough to analyze some physiological parameters in great detail, especially in pathological situations, they are capable of capturing the main flow characteristics. Therefore, they provide valuable insights into the dynamics that allow to improve the general understanding of cardiac fluid dynamics. For example, Segarra et al. [156] used a 2D FSI model to analyze the operation of a stenotic valve compared to a normal valve. Kivi et al. [97] studied the hemodynamic effects of calcification on the aortic root and coronary arteries to identify potential sites of coronary stenosis in a two-dimensional healthy aortic valve model.

When physiologically accurate results are required, one can feed the model with patient-specific image-based geometries of the aortic root, the left ventricle, and atrium. For instance, Hasan et al. [72] built a realistic, three-dimensional anatomical model of the aortic root and ascending aorta, using an anatomical geometry reconstructed from patient-specific Computed Tomography (CT) angiography data. Gao et al. [61] also presented an integrated model of the mitral valve coupled to the left ventricle, with the geometry derived from in vivo clinical magnetic resonance images. Some studies, *e.g.,* Halevi et al. [69], also considered the 3D geometry of the calcification with patient-specific 3D calcification patterns obtained from CT images.

The various elements discussed in section 1.3.3 regarding FSI methods in general are all the most relevant for modeling the dynamics of heart valves. Fully coupled models are crucial to account for the opening and closing of the valve. A recent review of the different modeling strategies of the dynamics of the aortic valve reported that 51% of the studies published before 2021 used a moving grid method (like Arbitrary Lagrangian-Eulerian (ALE)) while 38% used a fixed grid method (like the Immersed Boundary Method (IBM)) [1]. ALE methods ensure an accurate calculation of blood rheological properties and shear stresses near the blood leaflet interface. However, the need for a constant remeshing is a challenging and expensive computational step. For this reason, and because of the amplitude of the deformation undergone by the very thin leaflets, the IBM is often preferred to the ALE approach. Gao et al. [61] for instance developed a left ventricle two-way FSI model to simulate a complete cardiac cycle using the immersed boundary method. Hasan et al. [73] also constructed physiologically realistic immersed boundary models of the dynamics of the aortic root and ascending aorta. Lemmon and Yoganathan [105] used the IBM approach to develop a three-dimensional FSI model to account for blood–tissue interaction in order to simulate the leaflets kinematics of bioprosthetic valves. Fixed-grid methods have however to interpolate the solution data near the blood leaflet interface, which consequently results in imprecise calculation of important flow parameters such as wall shear stresses on the leaflets. It was therefore concluded by Bavo et al. [10] that for two-dimensional aortic heart valve geometries, the differences between ALE and IBM are unsubstantial, but that ALE face major grid quality distortion when it is used in simulating three-dimensional geometry of the aortic valve.

The most significant challenge of mesh-based approach is the coaptation between the leaflets during valve closure, where the flow domain is separated into two unconnected regions. Dabiri et al. [37], for instance, investigated the effect of different designs of linear elastic leaflets of bioprosthetic heart valves on the transvalvular gradients using ALE but, despite its influence on the kinematics, the mutual coaptation between the leaflets was not modeled.

Meshless methods have been able to counter the problems faced by grid-based FSI methods in terms of accuracy and stability. These methods may significantly contribute to the improved estimation of blood damage because they can more accurately model the blood particles compared with conventional Lagrangian particle-tracking methods. Mao et al. [114] applied an implicitly coupled FSI algorithm based on Smoothed Particle Hydrodynamics (SPH) to investigate the leaflets dynamics of a transcatheter aortic valve. Shahriari et al. [158] extended this method to investigate the accumulation of shear stresses on blood particles by simulating blood flow through normal and dysfunctional bileaflet mechanical heart valves. So far, the meshless methods have however been only occasionally applied to heart valve simulations.

To the best of our knowledge, the Particle Finite Element Method (PFEM) has never been applied to analyze the dynamics of heart valves.

4.2 Two-dimensional model of the aortic valve.

In order to illustrate the capability of the PFEM to describe the dynamics of the ejection of blood from the left ventricle, we consider here the simplified two-dimensional plane strain model of the aortic valve shown in Figure 4.2. This geometry and the parameters listed in Table 4.1 are that of Ariane et al. [3] and Sun et al. [172].

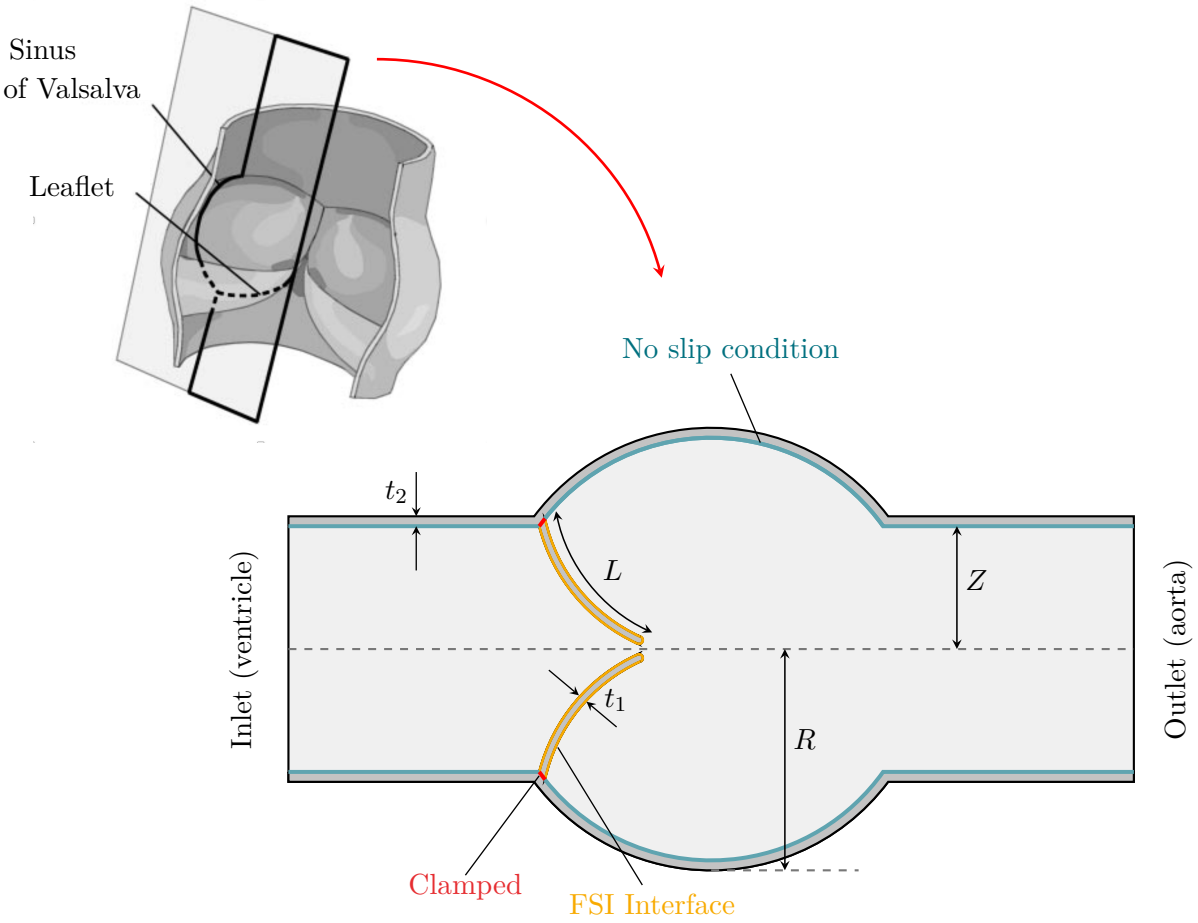

FIGURE 4.2 – Geometry of the two-dimensional aortic valve with fluid domain ( ), solid domain ( ), and boundary conditions (clamped (—), FSI interface (—), and no slip condition (—)). Inspired by De Hart et al. [39].

Parameters	*Values*	*Units*
Aorta radius Z	1.25	cm
Leaflet length L	1.6	cm
Leaflet thickness t_1	0.05	cm
Sinus cavity radius R	2.15	cm
Aortic wall thickness t_2	0.1	cm
Domain total length	6	cm

TABLE 4.1 – Geometrical parameters for the aortic valve simulations.

The fluid domain comprises the left ventricle, two sinuses, and the initial segment of the aorta. The aortic valve is modeled as two flexible leaflets. In the real heart, the valve has three leaflets that can open in their respective sinus cavity, with the left and right sinuses containing their own coronary ostia.

The main objective of the model is to reproduce the interaction of the flow with the leaflets and the opening/closing of the valve. With this objective in mind, and considering the much larger rigidity of the peripheral walls, only the leaflets are considered as deformable.

Only a few models describe the behavior of the leaflets with complex constitutive models. Sadeghpour et al. [146] used a Mooney-Rivlin material. Gao et al. [61] and Hasan et al. [72] modeled the leaflets as a fiber-reinforced material to reflect the collagen fibers distributed throughout the leaflets. Such complex approaches are necessary and appropriate in realistic geometries that focus on the mechanical loading of the leaflets. However, the vast majority of previous models of heart valves introduce extensive simplifying assumptions. The large rotations of the nearly incompressible isotropic leaflets are indeed accompanied by small strains, so that the assumption of linear elasticity according to Hooke's law is considered as a reasonable assumption [63]. This approach is used in the current study.

In light of the previous discussion about blood rheology, blood can be described as a Newtonian fluid when it flows through the aortic valve. The pulsatility of the flow and the large velocity shear largely support this approach. By the same token, however, the hypothesis of a laminar flow implicitly made so far is no longer valid for the Reynolds number corresponding to a 1 m/s flow through the valve, *i.e.,*

$$Re = \frac{\rho^f U Z}{\mu} = 3450 \tag{4.1}$$

is larger than the commonly accepted threshold of 2300 for a laminar flow. If one takes into account the fact that the flow is accelerated rapidly by the contraction of the ventricle and pushed through a narrow inter-leaflet space, turbulent effects must be taken into account. In the absence of a turbulence model, blood viscosity is artificially increased by a factor of 10 in the simulations presented here to reflect the increase in momentum diffusion.

In some previous models of flow through the aortic valve, a time-dependent velocity profile is prescribed at the inlet, while the outlet pressure is either kept constant or made to vary with time [97, 128, 172]. This approach is inappropriate to capture the real mechanism behind the opening of the aortic valve, which is controlled by the pressure difference between the left ventricle and the aorta[1].

[1]Sun et al. [172] incorrectly impose a velocity time series as input to their model, which is the one reported by Scotti et al. [155] to describe the flow approaching an abdominal aneurysm, and is therefore unrelated to the velocity upstream of the aortic valve.

We chose to drive the model by imposing the temporal pressure variations shown in Figure 4.3 on both the ventricular and aortic sides. The boundary data are obtained from Nobari et al. [128]. This approach allows the processes responsible for opening and closing the aortic valve, as well as the ejection of blood from the left ventricle into the sinuses, to be fully modeled. When the ventricular pressure exceeds the aortic pressure during the contraction of the heart, the balance of forces on either side of the leaflet drives its opening, while the leaflets close when the pressure gradient is reversed.

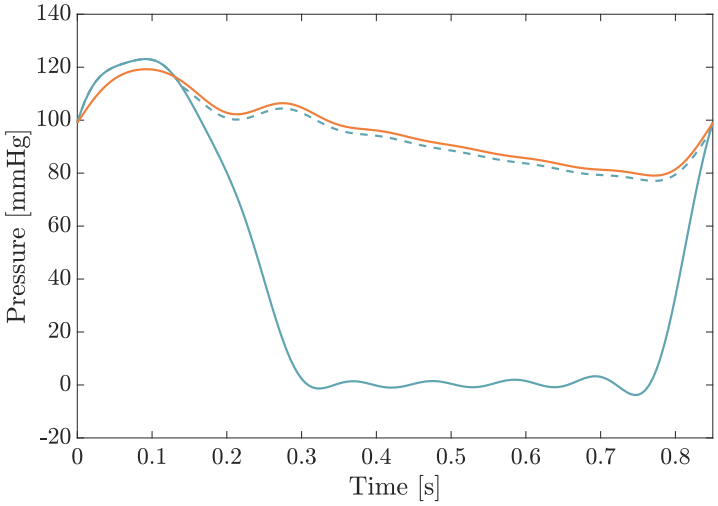

FIGURE 4.3 – Time series of the inlet (ventricle) (——) and outlet (aorta) pressures (——) prescribed at the open boundaries of the model domain. To compensate for the impact of the 2D geometry, the ventricular pressure is modified to ensure that the valve resists the applied pressure difference (- - -): the maximum pressure difference between the aorta and the ventricle is 2 mmHg.

4.2.1 Limitations of the 2D approximation.

The simplification of the geometry associated with the 2D model comes together with an important modification of the dynamics of the aortic valve. In the 2D model, the leaflets appear as curved cantilever beams, *i.e.*, they are supported only at their base where they connect with the heart wall. A simple calculation reveals that such a thin two-dimensional leaflet would not be able to resist the huge pressure difference between the sinus cavity and the left ventricle.

Deflection of a two-dimensional leaflet

The maximum deflection of a clamped beam (with free extremity) of length L, height t, and transversal dimension e under a constant distributed load per unit length w is given by

$$V_{max} = \frac{wL^4}{8EI} = \frac{3pL^4}{2Et^3} \tag{4.2}$$

with the inertia $I = et^3/12$ and $w = pe$, with p the pressure [115]. Considering the numerical values of $t = 0.5$ mm, $p = 100$ mmHg, $L = 1.6$ cm, and $E = 2$ MPa, a maximum deflection of about 5 m is obtained. This value of the Young's modulus is a physiological value reported by Ghasemi et al. [64] and Nobari et al [128].

In reality, leaflets derive their stiffness from the fact that they are not flat but curved along two axes, and are attached to at least a third of the valve perimeter. These aspects cannot be reproduced in a two-dimensional approach. This has two important implications for the model.

- First, the artificially reduced resistance to deformation of the leaflets under a given pressure difference must be compensated by artificially increasing their Young's modulus. A value of 10^7 Pa, much larger than the actual value of the constitutive material of the leaflets, is therefore used in the simulations. This value has been set by trial and error to match the observed outflow peak velocity.
- Second, even with such a large value of the Young's modulus, the leaflet would not resist the 100 mmHg pressure difference between the aorta and the left ventricle when the valve is closed. Therefore, the boundary conditions are modified to clip the pressure difference and prevent that the pressure within the sinus cavity exceeds the pressure on the other side of the leaflet by more than 2 mmHg (Figure 4.3). This has little influence on the flow since the two regions are disconnected when this clipping is activated.

Replacing the 2D model with an axisymmetric model would address both the above problems, by replacing the two leaflets with a single one covering the entire valve perimeter. The strength of this single leaflet would then be ensured by its axisymmetric geometry. Beside the resulting artificially large strength, this solution poses other technical problems when the valve closes, since the valve would then have to make contact with itself along the axis of symmetry, which is likely to pose numerical problems because of the singularity on this axis.

The final choice of material parameters is reported in Table 4.2.

Parameters	*Values*	*Units*
Fluid density ρ^f	1050	kg/m^3
Dynamic viscosity μ	0.038	Pa $\cdot$ s
Leaflets wall density ρ^s	1060	kg/m^3
Leaflets Young's modulus E	10	MPa
Leaflets Poisson's ratio ν	0.45	-

TABLE 4.2 – Material parameters for the aortic valve simulations.

4.2.2 Other numerical considerations.

The initial PFEM mesh contains 4960 particles with an increased resolution near the leaflets (Figure 4.4) to capture the larger velocity shear around the leaflets. The leaflets themselves are discretized with a transfinite mesh consisting of 200 elements along each leaflet and 12 elements across.

The model is integrated forward in time with a time step of $5 \cdot 10^{-5}$ s that is necessary to capture the delicate contact between the leaflets and to cope with the large velocity, exceeding 1.2 m/s, associated with the pulsed outflow from the ventricle. Instability develops at the open boundaries when attempting to solve the problem with smaller time steps. With such a small time step, it takes about 6 hours and a half to simulate one single heartbeat (= 0.85 s).

Unlike the study of arteries presented in the previous section, there is no need here for a progressive application of boundary conditions. In fact, it is sufficient to start the simulations at the moment when the pressure in the ventricle is equal to the pressure in the aorta and the valve begins to open. At this point, pressure is uniform and velocity is naturally zero, so that initial conditions compatible with the boundary conditions can be easily prescribed.

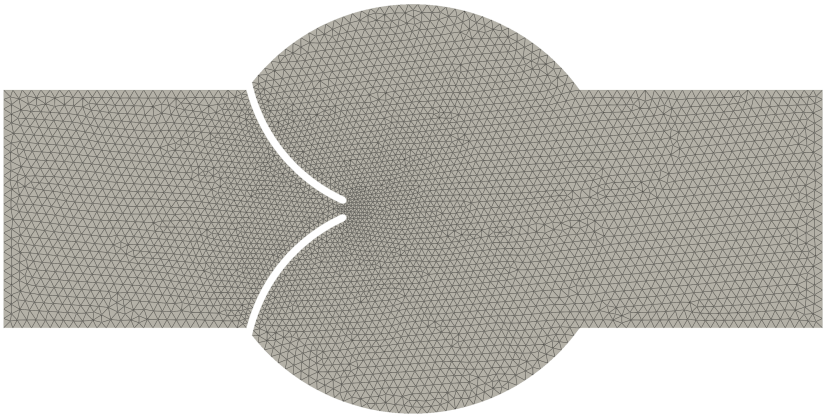

FIGURE 4.4 – Initial PFEM mesh with 4960 particles. The resolution is increased by a factor 2 in the vicinity of the leaflets.

Running the simulation for two cycles confirms that there is very little difference between the first and second cycles, even at the initial time. Therefore, the solution computed during the first cycle can be considered to be representative of the periodic solution.

The contact interactions between the two leaflets are handled using the *sticking model* implemented in Metafor (penalty of 10^8 Pa and $0.7 \cdot 10^8$ Pa respectively for the normal and tangential components). This contact model turns out to be necessary to avoid sliding of the two leaflets. This model ensures that the tips of the two leaflets stick to each other when they touch and the valves remain closed as long as the net normal force between is opposed to their outer normal vector.

4.2.3 Flow through the aortic valve.

Snapshots of the flow through the aortic valve, as computed with the nominal parameters listed in Tables 4.1 and 4.2, are shown in Figure 4.5. In spite of the many simplifying assumptions, the model succeeds in reproducing the qualitative behavior of the aortic valve as well as some of its quantitative aspects.

Initially ❶, the valve is closed as the pressure inside the left ventricle is less than that in the aorta. There is no flow through the valve, nor through the aorta.

As the heart contracts, the valve opens when the pressure difference across the leaflets is large enough to push them toward the sinus cavity ❷. Blood starts then to flow from the left ventricle to the aorta.

The opening of the valve and the flow are very dynamic events, which produces a very pulsatile flow ❸. In the Valsalva cavity, the velocity peaks at more than 1 m/s. This value is usually reported for a normal healthy patient [205].

As the pulse progresses, vortices appear in the sinus cavity and a backflow develops along the aortic walls ❹. The aortic sinus vortex is one of the most important and prevalent fluid dynamic features in the aortic sinuses. It is known to play a crucial role in the context of sinus washout and overall energy efficiency of the aortic valve system [74].

Combined with the decrease of the ventricular pressure, the secondary circulation contributes to the progressive closure of the valve ❺. This, also, is in agreement with the in vivo observations of the flow [148].

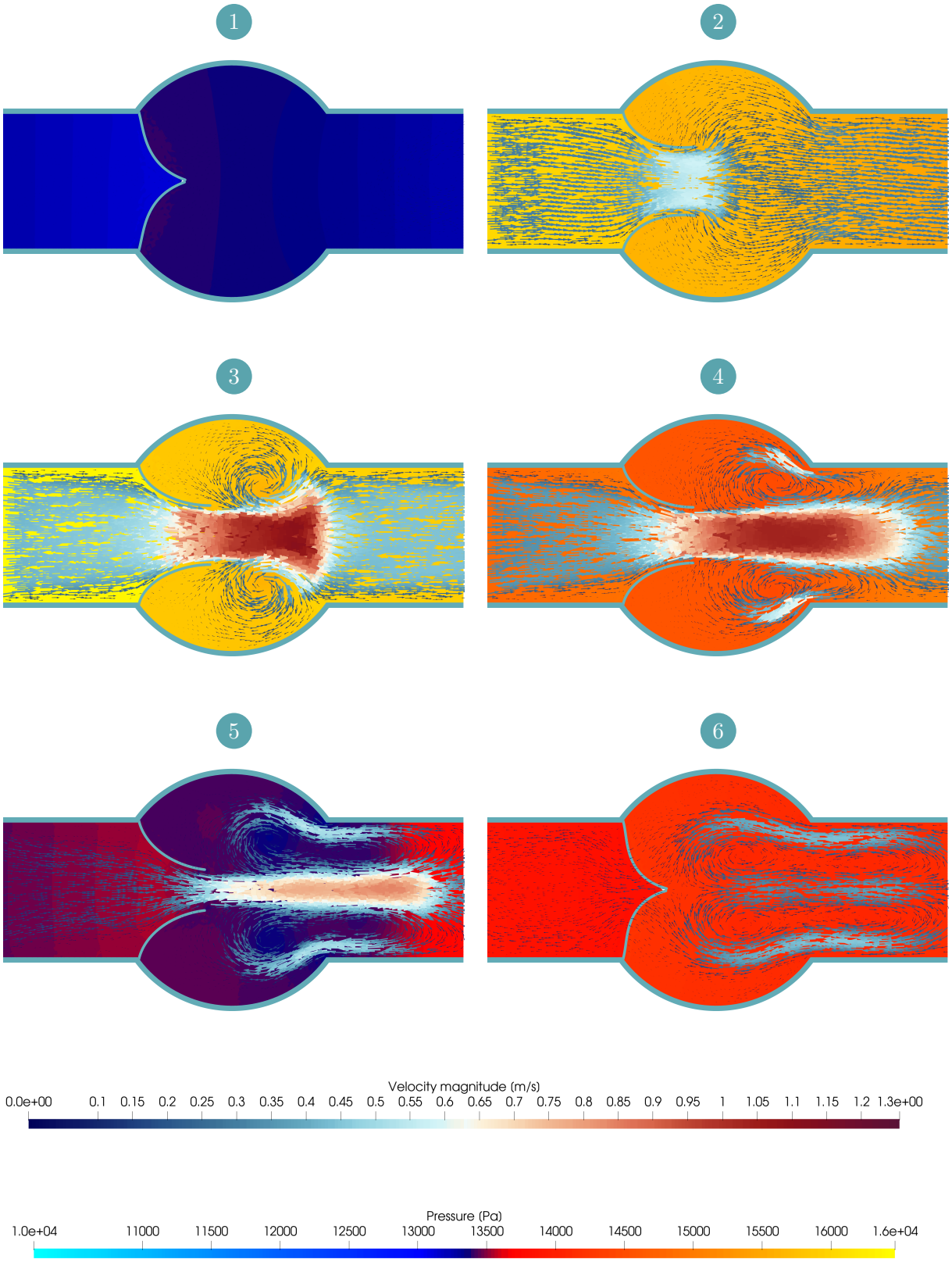

FIGURE 4.5 – Pressure (background color) and velocity fields (arrows) at 6 successive moments of the cardiac cycle: ❶ $t = 0.00$ s, ❷ $t = 0.05$ s, ❸ $t = 0.10$ s, ❹ $t = 0.15$ s, ❺ $t = 0.20$ s, and ❻ $t = 0.30$ s.

With the closing of the valve, the flow from the heart toward the aorta stops while the vortices are progressively damped [6]. The velocity progressively goes to zero during diastole before a new cardiac cycle begins.

The model results are not directly applicable for estimating the volume of blood pumped into the circulatory system with each heartbeat (the stroke volume), as the 2D model only provides an estimate of the flow rate per unit length across the transverse dimension. Extrapolating the 2D results to a depth of $2Z = 2.5$ cm, one comes out with a stroke volume of 34.4 mL, which is of the right order of magnitude but a half of the physiological value of 70 mL [178]. This difference can be attributed to the 2D geometry and the rather small 13 mm opening of the valve [185].

The rapid movement of blood through the constricted valve generates significant shear stresses on the leaflets, and to a lesser extent, around the intersection of the sinus cavity and the aorta. When the valve is fully open, the shear rate ($\dot{\gamma} = \sqrt{2\,\mathbf{D} : \mathbf{D}}$) reaches 540 s^{-1} on the ventricularis side (*i.e.,* facing the ventricle) of the leaflets (Figure 4.6). The maximum appears at the tip of the leaflets. While more quantitative estimates should be confirmed with an even higher resolution modeling to better capture the large gradients in the vicinity of the leaflets, our results are in line with the previous studies and show that the shear rate, and hence the wall shear stress, on the fibrosa side (*i.e.,* facing the aorta) of the leaflets and the sinus section behind them is considerably lower and more dynamic. As reported by Moore et al [122], these areas are particularly prone to calcification, especially if the vortices in the Valsalva cavity fail to adequately cleanse them.

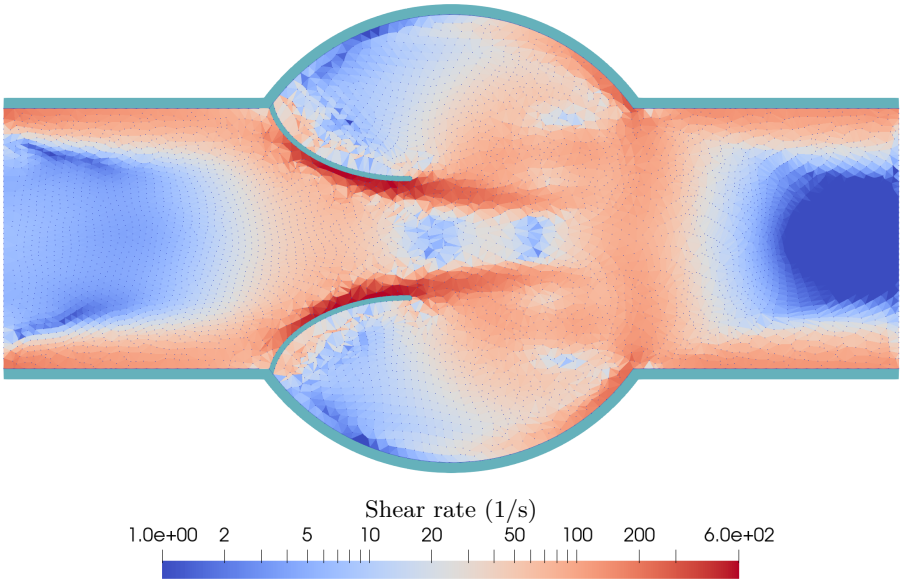

FIGURE 4.6 – Shear rate at the time of maximum opening of the aortic valve.

4.2.4 Modeling the effect of calcification.

As mentioned in chapter 1, calcification is one of the most recurrent causes of aortic valve diseases. To illustrate how calcification can affect the normal functioning of the valve, the simulation described in the previous section is repeated by adjusting the thickness t_1 of the leaflets. Instead of the nominal thickness of 0.5 mm, we consider two alternative values of, respectively, 0.75 mm and 0.85 mm. While these changes do not affect the results in any qualitative way, they increase the flexural stiffness of the valves, which are therefore expected to be more resistant to the imposed pressure gradient. Obviously, the same effect could also be modeled by increasing the Young's modulus of the material of the leaflets.

Figures 4.7, 4.8, and 4.9 provide a quantitative comparison of the results obtained with the baseline case and the two alternative simulations with thicker leaflets.

The effect of the increased flexural rigidity of the leaflets can first be observed in Figure 4.7 of the distance between the two leaflets as a function of time, *i.e.,* of the opening of the valve. This figure suggests that calcification will affect both the duration of the opening and its width. In the nominal configuration, the valves remain open for about 0.28 s. This is about 33% of the cardiac cycle (period $T = 0.85$ s), which is in agreement with experimental data for the normal heart [128]. With the thicker leaflets, the time during which the valve is open decreases to 0.22 s or even 0.20 s for the 0.85 mm-thick leaflets. At the same time, the width of the opening is also strongly reduced by calcification. With the thickest leaflets, the maximum opening is reduced by a factor 2, going from about 13 mm in the nominal run to 6.5 mm for the 0.85 mm-thick leaflets.

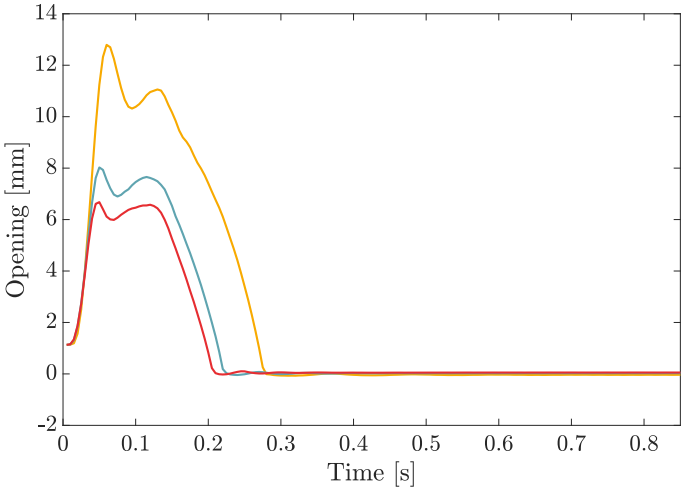

FIGURE 4.7 – Evolution of the opening of the valve with time for the nominal configuration with $t_1 = 0.5$ mm (—) and for two alternative configurations with thicker leaflets ($t_1 = 0.75$ mm (—) and $t_1 = 0.85$ mm (—)).

The opening of the valve influences of course the flow rate into the sinuses of Valsalva (Figure 4.8). The decreased opening of the thicker leaflets goes with a reduction of the flow rate through the valve. The maximum flow rate decreases and the flow occurs during a reduced period of time. It should be noted, however, that the maximum flow rate is not reduced in proportion to the reduction in valve opening. While the thickest leaflets show a maximum opening that is about half of the opening in the nominal configuration, the corresponding maximum flow rate nevertheless reaches 60% of that of the more flexible leaflets.

The reduction in both the maximum flow rate and the duration of the ejection phase for the stiffer leaflets results in a large decrease in stroke volume, the volume of blood ejected with each heartbeat (Table 4.3). Again, direct comparison of the raw numbers with physiological values is difficult, but the results illustrate how calcification can have a serious impact on the heart ability to pump blood throughout the body. Patients with calcification problems must compensate by increasing the heart rate, which can lead to excessive fatigue and even more acute heart and circulatory problems.

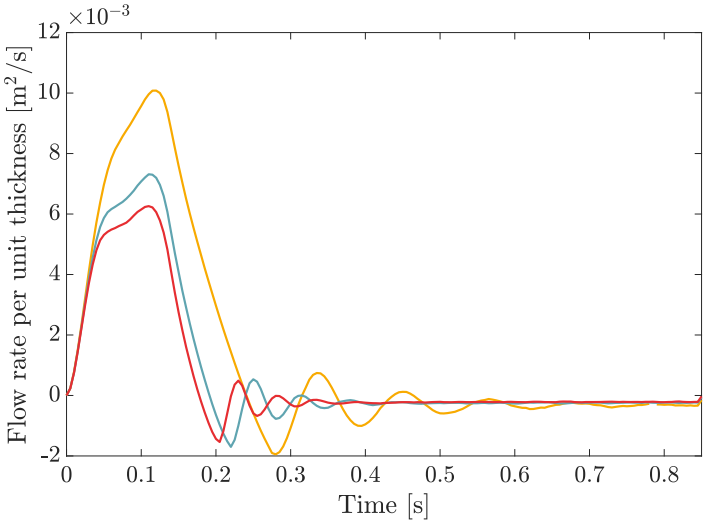

FIGURE 4.8 – Evolution of the flow rate (per unit length of transverse direction) with time for the nominal configuration with $t_1 = 0.5$ mm (—) and for two alternative configurations with thicker leaflets ($t_1 = 0.75$ mm (—) and $t_1 = 0.85$ mm (—)).

$t_1 = 0.5$ *mm*	$t_1 = 0.75$ *mm*	$t_1 = 0.85$ *mm*	*Units*
1377.1	871.4	724.9	mm^2

TABLE 4.3 – Stroke volume per unit thickness.

The data plotted in Figure 4.8 are computed by integrating the velocity field in the ventricle along a vertical line between the inner attachment points of the leaflets. The first negative peaks in the curves correspond to the small backward flow that occurs just before the valve closes. The following oscillations during diastole reflect the movements of the leaflets that, although remaining closed during that phase, oscillate in response to the variations of the pressure gradient and the oscillating flow in the Valsalva cavity to which they are exposed. The small oscillations of the closed leaflets set the fluid in motion inside the ventricle without contributing to any net blood transfer between the disconnected ventricle and aorta. The thinner leaflets are of course more sensitive to this phenomenon. It is unclear whether oscillations of this amplitude really occur in the real heart or if they are largely influenced by the 2D simplification of the leaflets considered in this simplified model.

The above discussion suggests that calcification has a proportionally stronger influence on the opening of the leaflets than on the flow rate. As suggested by Figure 4.9, which shows the evolution of the longitudinal velocity at a point located 0.5 cm downstream the center of the sinus cavity, the decreased opening is partly compensated by a small increase of the maximum velocity. This is of course because the pressure difference between the ventricle and the aorta remains the same in all the simulations but the fluid is pushed through a smaller orifice when calcification restricts the opening of the valve [130].

Clinical studies reveal that calcification of the aortic valve affects the hemodynamics inside the aortic root such as the transvalvular pressure gradient and the wall shear stress on both sides of the leaflets. Prior research has shown that variations in wall shear stress levels on the front and back surfaces of leaflets play a role in calcification formation [97]. As calcification levels rise, WSS levels increase on the front ventricularis surface, but decrease on the back fibrosa surface. Therefore, the WSS gradient between the two surfaces intensifies, potentially triggering mechanobiological

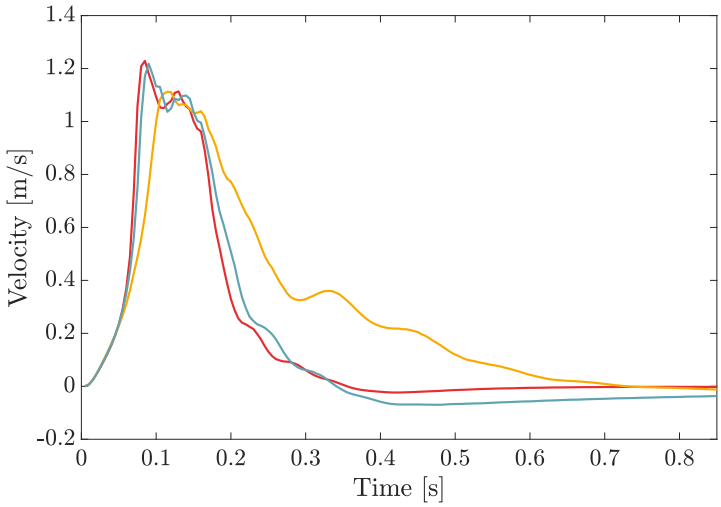

FIGURE 4.9 – Evolution with time of the longitudinal blood velocity 0.5 cm downstream the valve for the nominal configuration with $t_1 = 0.5$ mm (—) and for two alternative configurations with thicker leaflets ($t_1 = 0.75$ mm (—) and $t_1 = 0.85$ mm (—)).

.

mechanisms that further promote calcification, thus perpetuating stenosis over time [2, 96].

Our results are consistent with these findings. The general distribution of the shear rate for calcified leaflets is similar to Figure 4.6 but the the shear rate at peak systole on the ventricularis surface increases from 540 s^{-1} for the 0.5 mm-thick leaflets, to 580 s^{-1} and 620 s^{-1} in the two calcified cases.

4.2.5 About the influence of viscosity and turbulence.

The above results are obtained with a 10 fold increase of the viscosity in an attempt to account for turbulent features. To explore the effect of this crude parameterization on the results of the different runs, the nominal simulation is repeated here without this parameterization, *i.e.,* using the nominal value of blood viscosity ($\mu = 0.0038$ Pa $\cdot$ s).

The time series of the width of the opening between the leaflets and the flow rate across the valves are shown in Figures 4.10 and 4.11. The results suggest that the value of the effective viscosity has little effect on these two parameters until the valve is about to close. At this time, however, without any parameterization of turbulence, the distance between the two leaflets passes through a small almost horizontal plateau (see Figure 4.10 at $t = 0.2$ s) when the symmetry of the movement of the two valves is lost. Very energetic and asymmetric vortices develop in the sinus cavity, forcing the two leaflets to move in a completely asynchronous manner (❶ in Figure 4.12). By chance, during this simulation, the two leaflets are pushed against each other at a later time and the valve closes. The asynchronous movements of the two valves could however make them flip into the ventricular region at different times without touching each other so that the valve would not close. The vortex behind the leaflets remains very active throughout the diastole, with a maximum velocity of 80 cm/s ❷. Such very energetic features are not expected in the healthy heart, demonstrating the need for proper treatment of turbulence to obtain realistic results in the model or a dramatic (and non affordable) increase of the spatial resolution to describe dissipation mechanisms. The latter option would require a three-dimensional model of the aortic root as turbulent eddies are essentially three-dimensional.

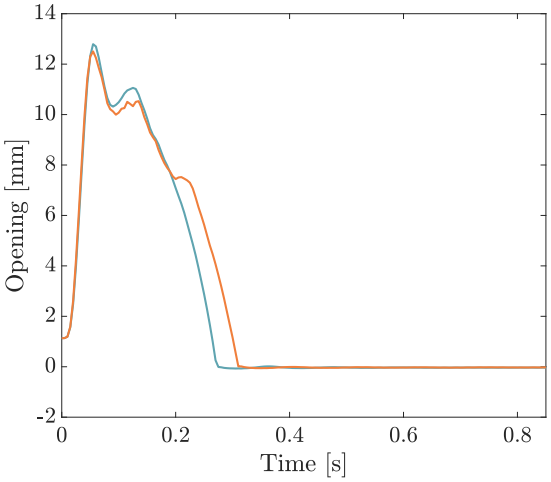

FIGURE 4.10 – Time evolution of the opening of the valve with (——) and without (——) parameterization of turbulence.

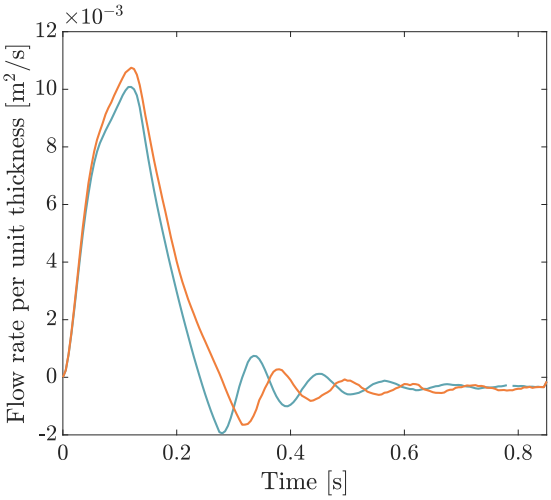

FIGURE 4.11 – Time evolution of the flow rate (per unit length of transverse direction) with (——) and without (——) parameterization of turbulence.

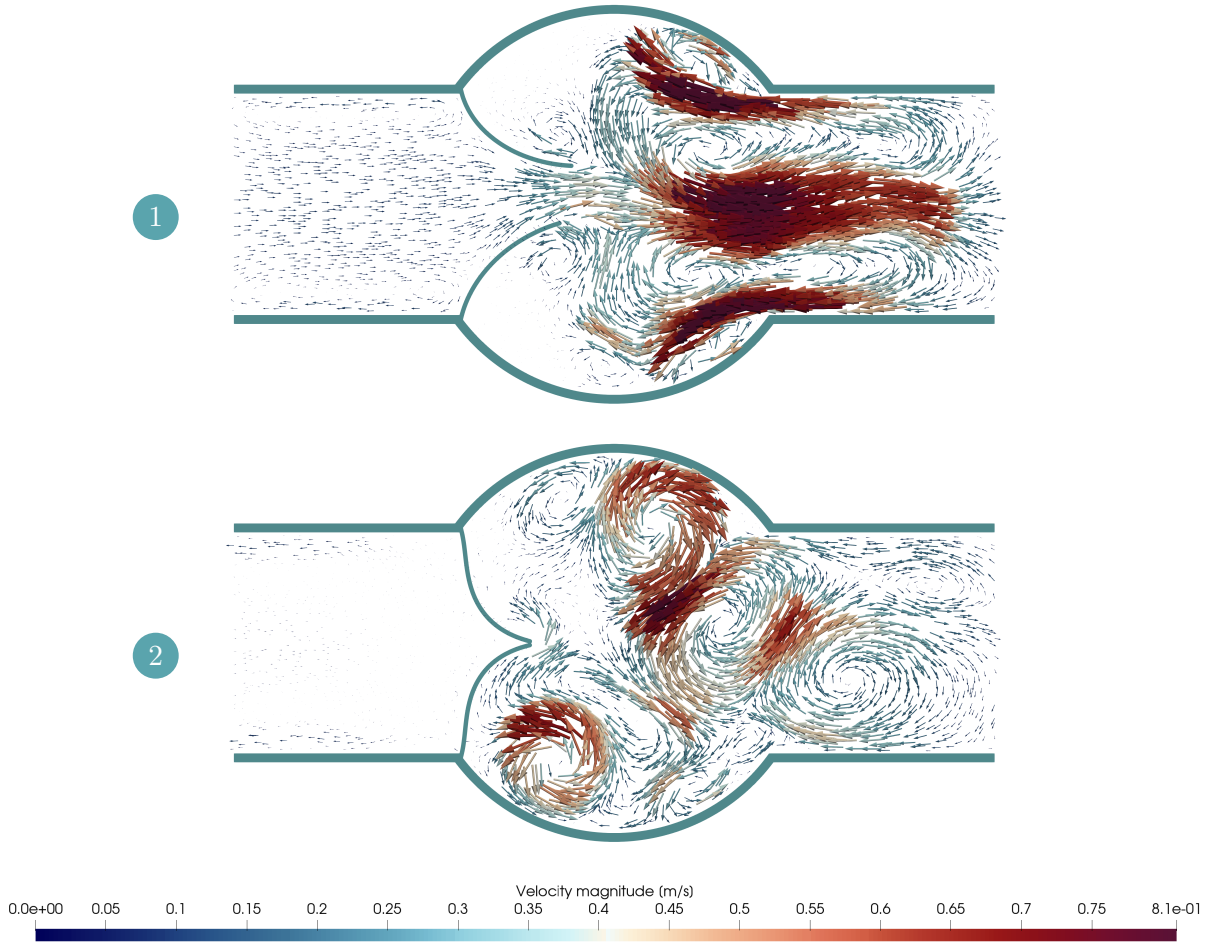

FIGURE 4.12 – Velocity fields without parameterization of turbulence at two moments of the cardiac cycle: ❶ $t = 0.225$ s (before the closure of the valve) and ❷ $t = 0.355$ s (after the closure of the valve).

CHAPTER 5

ANEURYSM

5.1 Modeling of aneurysms with FSI.

Considering the interdependence of structural and fluid domains, Fluid-Structure Interaction (FSI) approaches are frequently used to investigate the dynamics of abdominal aortic and cerebral aneurysms. These approaches provide crucial qualitative and quantitative insights for assessing the various risk factors linked to aneurysms.

Many studies demonstrate the potential of numerical modeling for predicting the progression and risk of rupture of Abdominal Aortic Aneurysms (AAAs). In these studies, geometry appears as one of the most important factors. It has been demonstrated that the shape of an AAA, the thickness of the arterial wall, and the degree of asymmetry are major factors in determination of the arterial wall stress distribution [141, 155]. Drewe et al. [46] also highlight the impact of iliac bifurcation angles on rupture risk. The geometry contributes therefore significantly to the mechanical response of AAA and its rupture risk.

Although some studies resort to simplified geometries, many rely on patient-specific models reconstructed from clinical images. Campobasso et al. [22], for instance, use 4D Magnetic Resonance Imaging (MRI) datasets acquired on a patient while Mesri et al. [117] build their model geometry from Computed Tomography (CT) angiographic data. Rostam-Alilou et al. [144] emphasize that individualized models based on patient-specific properties show significant differences from a generic model, with the patient-specific model demonstrating significantly altered stress at the site of the aneurysm compared to the generic model.

Mesri et al. [117] emphasize the importance of proper AAA material model and wall thickness, with isotropic material and uniform wall thickness significantly underestimating Wall Shear Stress (WSS) compared to anisotropic variable wall models. Nonlinear behavior of the artery wall is also reported by Rissland et al. [143] and Xenos et al. [201] as an important factor for robust and accurate FSI simulations of AAA risk.

While exploring the influence of geometry with two patient-specific abdominal aneurysm data, Canchi et al. [23] also point toward the importance of biomechanical parameters, such as wall shear stress, for accurate treatment decisions. Stergiou et al. [169] examine how hematocrit affects AAA progression. They show that low values of hematocrit result in lower WSS values, which in turn promote plaque formation on the aneurysmal wall.

Numerical studies with FSI have also been used to focus on specific connective tissue disorders: simulations with a hyperelastic modeling of the aortic wall have compared wall shear stress

between Marfan syndrome patients, *i.e.,* with altered elasticity of the aorta, and healthy patients. The findings revealed lower wall shear stress in Marfan syndrome patients, suggesting vascular remodeling in areas affected by aneurysms [140].

Different studies suggest the potential of coupled fluid-structure models for planning patient-specific surgical interventions. A study of Helthuis et al. [76] for example studied the efficacy of partial occlusion for the treatment of Cerebral Aneurysm (CA). A similar approach has also been used to optimize stent placement and assess its functionality after surgery [90].

Cerebral aneurysms have also been the focus of much modeling work. Hajirayat et al. [68] for instance employed FSI methods to explore the impact of cerebral aneurysm neck shape on rupture risk and hemodynamics, revealing significant differences between circular and elliptical neck cases (Figure 5.15 for neck definition). Other studies have identified arterial bifurcations as the most susceptible sites for intracranial aneurysm formation [144].

5.2 Numerical modeling of an axisymmetric aneurysm.

In this section, we consider the interaction of blood flow with a compliant axisymmetric abdominal aneurysm wall, with the objective of analyzing the influence of aneurysm size and wall thickness heterogeneity on the mechanical stresses and fluid dynamics.

The aneurysm is assumed to be fully developed with an axisymmetric shape shown in Figure 5.1. The geometry is directly inspired from Scotti et al. [155] (Figure 5.2). While the introductory discussion suggests that more realistic geometries should actually be considered, such simulations are beyond the scope of the current exploratory study.

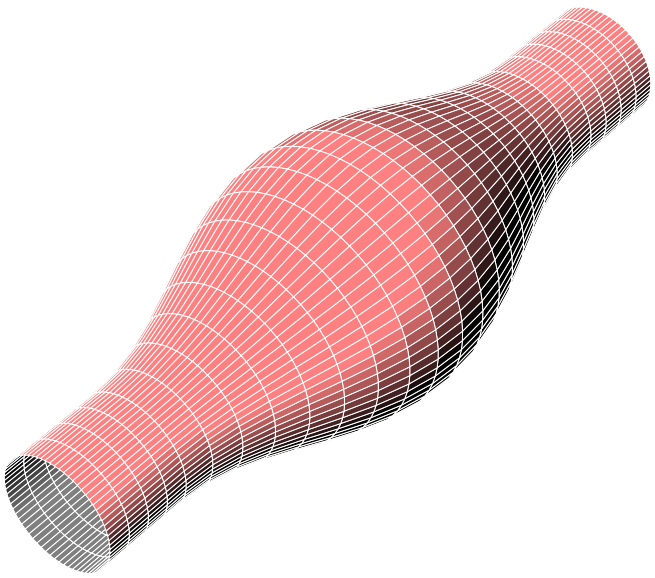

FIGURE 5.1 – Geometry of the axisymmetric abdominal aortic aneurysm.

The fluid domain is characterized by a circular cross section with a non dilated diameter r and a maximum radius R at the midsection of the AAA sac. More precisely, the radius $\phi(y)$ is assumed to vary with the longitudinal coordinate y according to

$$\phi(y) = \begin{cases} r + \dfrac{(R-r)}{2}\left[\cos\left(\dfrac{\pi y}{6r}\right) + 1\right] & \text{if } -6r \leqslant y \leqslant 6r \\ r & \text{if } |y| > 6r \end{cases} \tag{5.1}$$

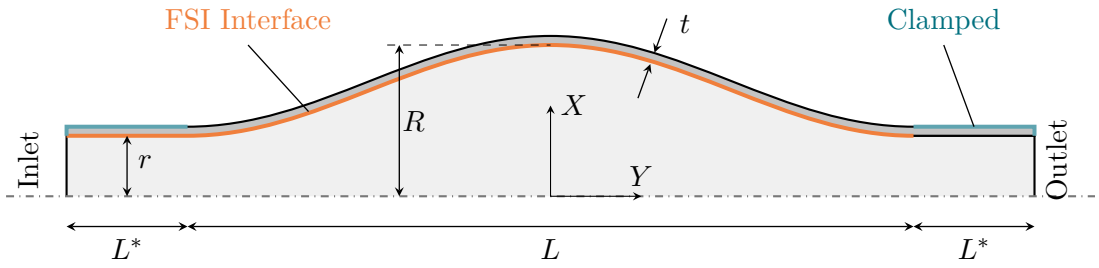

FIGURE 5.2 – Geometry of the axisymmetric abdominal aortic aneurysm with fluid domain (■), solid domain (■), and boundary conditions (clamped (—) and FSI interface (—)).

The total length of the aneurysm is $L = 12$ cm, which is about the actual length of the abdominal aorta, but the model is extended upstream and downstream with $L^* = 2$ cm segments to avoid spurious oscillations between the inlet/outlet boundary conditions and the moving walls. The geometrical parameters considered in the different simulations are listed in Table 5.1.

Parameters	*Values*	*Units*
Length L	12	cm
Length extension L^*	2	cm
Vessel radius r	1	cm
Aneurysm radius R	2 - 2.5 - 2.75	cm
Thickness t	0.15	cm

TABLE 5.1 – Geometrical parameters for the abdominal aortic aneurysm simulations. The actual domain is extended upstream and downstream by 2 cm to avoid numerical artifacts and instabilities at the boundaries of the fluid domain.

The model is forced by prescribing the same velocity and pressure time series at the upstream and downstream boundaries of the fluid domain as those considered for the straight artery (Figures 3.14 and 3.15). These describe a full cardiac cycle between a diastolic pressure of 70 mmHg and a systolic pressure of 115 mmHg. The average velocity at the inlet is assumed to peak at about 30 cm/s shortly before the maximum systolic pressure.

The time-averaged velocity prescribed at the inlet is about 6 cm/s. The mean Reynolds number is therefore 332 and, as observed by other authors, the flow can be assumed to be laminar in the abdominal aorta [54, 155]. In line with the discussion of the flow in a straight artery presented in chapter 3, blood is assumed to behave as a Newtonian fluid. The Womersley number and the anticipated shear rate are large enough to ignore any yield stress and shear thinning behavior of blood. The aortic segment is fixed at its two extremities, which accounts for the complete tethering of the aorta by the surrounding tissues and organs.

On account of the similar dynamics and forcing data, the numerical parameters identified through the convergence study in section 3.3.3 for analyzing flow through a straight artery are also used for simulating flow through an aneurysm. This results in an initial count of 4509 PFEM particles, with a resolution doubled near the fluid-structure interface. The segment of the artery wall in contact with the flow is represented by a transfinite mesh composed of 300 × 12 linear quadrangular elements (Figure 5.3).

5.2.1 Constitutive laws of the aortic aneurysmal wall.

As stated in the introduction, the choice of an appropriate constitutive law is an important factor for the successful modeling of the deformation of the wall of the AAA.

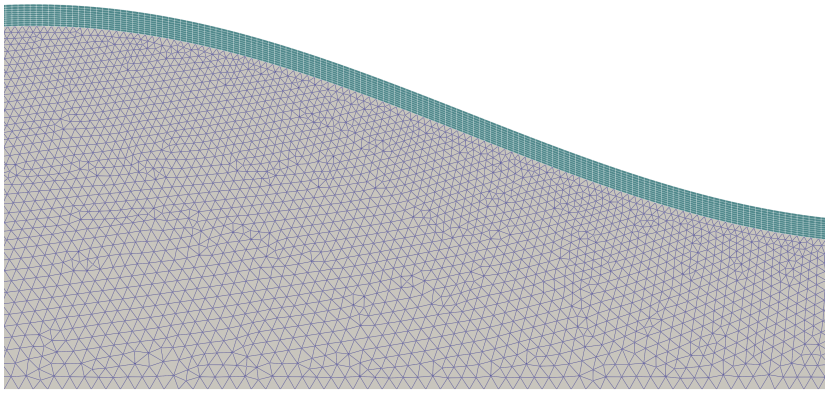

FIGURE 5.3 – Part of the initial mesh of the fluid and solid subdomains. The fluid and solid elements have similar sizes on the fluid-structure interface. The resolution in the fluid domain is increased along the interface.

Several studies consider that the aortic wall behaves as an isotropic, linear, and elastic solid. Scotti et al. [155], for instance, make this assumption with a Young's Modulus of 2.7 MPa and a Poisson's ratio of $\nu = 0.45$. These values are reported as the average characteristics for the aneurysmal abdominal aorta obtained by linearization of the stress-strain curve described by Di Martino et al. [41].

A Young's modulus of 2.7 MPa may seem significantly high compared to the reference value of 0.675 MPa mentioned in section 3. Indeed, the presence of AAA correlates with a marked increase in arterial wall stiffness. The formation of abdominal aortic aneurysms involves changes in the aortic wall connective tissue. A key histological characteristic of aneurysmal tissue is the breakdown of elastic fibers and the reduced presence of elastin as the aneurysm enlarges. This degradation predominantly occurs in the media layer, which begins to thin and lose its structured arrangement of elastic fibers, resulting in the deterioration of elastin and a rise in rigid collagen [11].

It is however widely agreed that aneurysm tissue should be modeled as a nonlinear hyperelastic material. Many such models have been proposed, with some of which also attempting to incorporate anisotropic behavior to reflect the underlying structure of the wall. Nevertheless, there is considerable inconsistency in the constitutive models used in the literature.

Different studies use the strain energy density function [95, 163, 172]

$$W = C_{10}(\bar{I}_1 - 3) + C_{20}(\bar{I}_1 - 3)^2 + \frac{K(J-1)^2}{2} \tag{5.2}$$

with the bulk modulus K and with the constants derived from the experimental data of the aneurysmal abdominal aorta provided by Raghavan et al. [139] ($C_{10} = 0.174$ MPa and $C_{20} = 1.881$ MPa). Apart from the fact that these authors do not specify whether they use reduced invariants or not, they incorrectly refer to a two-parameter Mooney-Rivlin type material when they are actually using a Yeoh model with $C_3 = 0$.

Other studies implement a true two-parameter Mooney-Rivlin law (3.33) but use the same experimental constants as Raghavan et al. ($C_1 = 0.174$ MPa and $C_2 = 1.881$ MPa) even though the parameters in the two models do not have the same interpretation and cannot be interchanged [4, 151]. The two constants in the two-parameter Mooney-Rivlin equation can be used to compute the shear modulus G as

$$G = 2(C_1 + C_2) \tag{5.3}$$

Using the above constant and a Poisson's ratio $\nu = 0.45$, one comes out with a Young's modulus of about 12 MPa. Although there is obviously considerable patient-to-patient variety in the stiffness of the aorta, such a huge value is never reported in experimental studies. The inconsistent use of constitutive laws and experimental parameters leads therefore many authors to work with an over-realistic stiffness.

To address the uncertainties in the constants and the model, we describe here a sensitivity study exploiting the data found in the literature and the implementation of the true Mooney-Rivlin model available in Metafor.

We consider three different values for the Young's modulus of the aortic wall, namely 0.675 MPa, 1.35 MPa, and 2.7 MPa. The smallest value characterizes the relatively flexible healthy aortic wall while the largest constant is typically reported for the fully developed aneurysm. These constants are further injected in both a linear elastic model and Mooney-Rivlin material. Since the Young's modulus is not sufficient to define the two constants of the Mooney-Rivlin constitutive equation but merely defines the sum of the two coefficients through Eq. (5.3) (using $\nu = 0.45$), we further introduce three variants of this constitutive equation using different values of parameter C_1. The parameters values for the M_1 variant are adapted from Valencia et al. [188] for the corresponding equivalent Young's moduli. The parameters values for M_2 and M_3 are introduced to explore the range of variability for the two parameters. The parameters constants are set proportionally for the different Young's moduli. The different sets of constants are listed in Table 5.2.

Young's Modulus E [MPa]	M_1 *[MPa]*		M_2 *[MPa]*		M_3 *[MPa]*	
	C_1	C_2	C_1	C_2	C_1	C_2
2.7 (High)	0.584	-0.1185	0.3	0.165	0.1	0.3655
1.35 (Mid)	0.292	-0.0592	0.15	0.0827	0.05	0.1828
0.675 (Low)	0.146	-0.0296	0.075	0.0413	0.025	0.091

TABLE 5.2 – Mooney-Rivlin parameters.

These different model parameters are used to simulate the deformation of an aortic abdominal aneurysm in a model of the wall only. This Metafor model uses the same geometry of the aneurysm introduced above but does not describe the actual fluid dynamics nor the fluid-structure interaction. The observed pressure variation (Figure 3.15) is therefore applied as a uniform loading to the model. In addition to varying the material constants, we also consider two sizes of aneurysm, *i.e.,* a small aneurysm with $R = 2$ cm and a larger aneurysm with $R = 3$ cm.

The results of these sensitivity studies are shown in Figures 5.4a and 5.4b as time series for the maximum displacement of a 1.5 mm-thick aortic wall in response to the physiological blood pressure fluctuations. The figures also show, for comparison purposes, the corresponding results obtained with a linear elastic model.

As expected, the maximum radial displacement of the aortic wall increases as the Young's modulus decreases. As already observed when studying the straight artery, in section 3.3.6, the results are however not inversely proportional to the stiffness of the artery, especially for the more flexible models. This indicates that geometric nonlinearities play a significant role in the problem. The figures further show that the results with different variants of the Mooney-Rivlin materials are consistent with the corresponding deformations computed with a linear elastic model: they coincide almost perfectly during the initial 0.3 seconds during which the pressure loading is applied gradually and the displacement of the wall is small. The different models produce however different results in the more flexible models, when the radial displacement exceeds 3 mm (which is twice the initial thickness of the aortic wall).

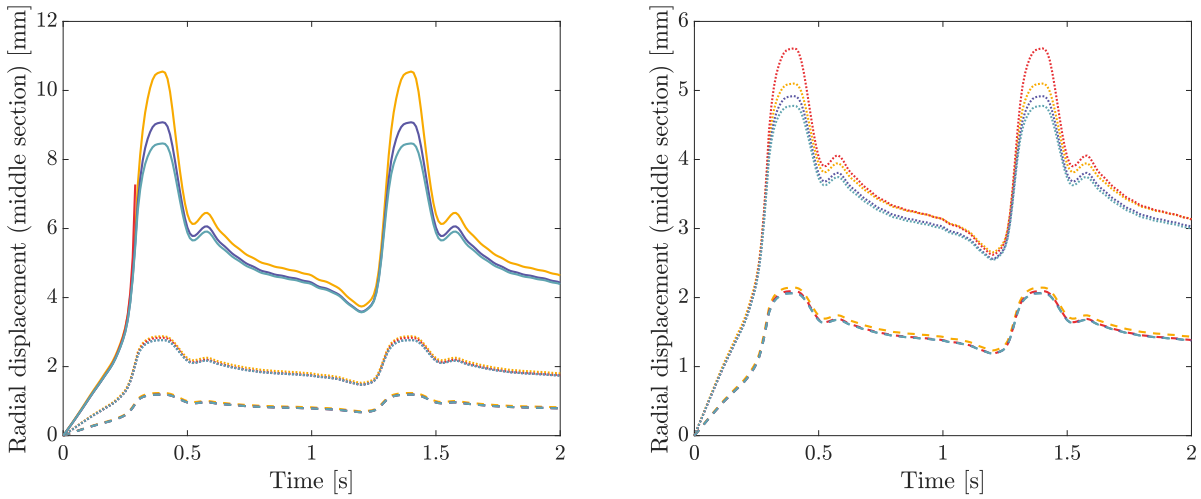

(a) $R = 2$ cm. (b) $R = 3$ cm.

FIGURE 5.4 – Influence of the constitutive law of the wall (of Table 5.2) on the aneurysm deformation during the cardiac cycle (linear elastic (——), Mooney-Rivlin M_1 (——), M_2 (——), and M_3 (——)) for different values of the Young's modulus (low (——), mid (·····), and high (- - -)). The curve for the Mooney-Rivlin model M_1 with the low Young's modulus (——) does not cover the two cardiac cycles. The simulation stopped due to unbounded deformation.

For the stiffest wall ($E = 2.7$ MPa), characteristic of the fully developed aneurysm, the Mooney-Rivlin model M_3 (- - -) yields maximum displacements that are only 3.5% and 3.8% smaller than that of the linear elastic model (- - -), respectively for $R = 2$ cm and $R = 3$ cm. They both produce deformations of about 1 mm, for the smaller aneurysm, and up to 2 mm for the 30 mm aneurysm that are in agreement with the results reported in the literature [155]. The small difference between the different results suggest that a linear elastic model may be sufficient here. The Mooney-Rivlin formulation will nevertheless be used in the following to account for possible effects of more complex stress-strain distributions than those considered in this simple example using a uniform loading of the aortic wall. The results suggest however that the precise choice of C_1 and C_2 has little influence, in spite of the large range of variation considered in this sensitivity study.

In addition to providing a sensitivity analysis to material parameters, the results presented in Figures 5.4a and 5.4b highlight some important particular aspects of aneurysm progression and resistance to rupture. The displacement varies more than proportionally with the aneurysm radius. Consequently, the more flexible aortic wall does not resist the physiological pressure range encountered in the artery if a large aneurysm is present. This is why Figure 5.4b does not present any result for the different models corresponding to $E = 0.675$ MPa. The simulations produce unbounded large deformations and stop rapidly. An aneurysm of this size would not be stable if its Young's Modulus was only 0.675 MPa. The large stiffness observed in developed aneurysms appears therefore not merely fortuitous or a negative side aspect of aneurysm formation. It is imperative to prevent rupture. More generally, our results suggest that the stability of an aneurysm depends upon the interplay between its radius and the aortic wall rigidity. From a dynamic point of view, they suggest that it is necessary for the wall material to develop a sufficiently rapid biological response to the development of the aneurysm by replacing the softer elastin by stiffer collagen to avoid larger deformations and rupture. Fortunately, an aneurysm with a Young's modulus of 2.7 MPa can grow safely up to a radius of 3 cm, at least if no other singularity nor abnormal stress occur.

5.2.2 About the boundary and initial conditions.

The simulation of flow in the aneurysm requires both appropriate initial and boundary conditions to describe the cardiac cycle. Some of the routines necessary for a proper handling of these are however not available in the current implementation of PFEM3D, which asks for some tricks to get the simulation running.

First of all, the simulation requires an appropriate initialization procedure. To avoid instabilities and spurious oscillations, the simulation must start from velocity and pressure fields that are nearly in equilibrium. Since the numerical model does not include any option to restart a simulation from previously computed fields, other than those that can be described as analytic functions of the space coordinates, the flow simulation is initiated with zero pressure and velocity fields. A constant non zero pressure field would be appropriate for the flow model but not for the aortic wall since this would be hit by a sudden and discontinuous in time pressure wave where a progressive application of the loading is required.

The initialization of the simulation of the flow through the aorta from homogeneous initial conditions has two aspects. First, one must gradually increase the background pressure from 0 to the level of 70-115 mmHg. This can easily be done with a ramp function applied to the pressure field prescribed at the downstream boundary. Because of the amplitude of the jump required to reach the physiological level, the transition time must be large to ensure a smooth start of the simulation. In practice, a transition time of 0.4 s is considered. The model is run for two cardiac cycles with the results extracted from the second heartbeat.

Most importantly, however, one must also ensure that progressive pressure and velocity waves develop in the artery. This second aspect of the initialization is intimately linked with the boundary conditions at the upstream and downstream boundaries of the aorta segment. Even if the time series of the inlet velocity and outlet pressure are obtained from accurate in vivo observation, *i.e.,* are real data, they must not only be compatible with each other but also with the dynamics computed by the model to produce meaningful results that are not blurred by numerical artifacts. If one tries to prescribe inconsistent upstream and downstream boundary conditions, pressure waves will be generated and bounce from one boundary to the other. This problem is particularly significant if dissipation mechanisms are too small to provide a natural/physical damping of these waves. Such oscillations can already be seen with small amplitude in Figure 3.22 in the straight artery results but are amplified with the current geometry because of the increased discrepancy between the observation data and the dynamics of the model (Figure 5.5). The oscillations exhibit here a period of 0.089 s, which appears as an eigenfrequency of the system. Attempts to get rid of these spurious oscillations by shifting the signals prescribed at the inlet and outlet (from -0.005 s to +0.01 s) or to extend the model domain (by up to 6 cm) did not produce any improvement. Similar oscillations are also clearly present in the results presented by Scotti et al. [155] even five cycles after initializing the model. The proper solution to this problem requires the development of dedicated boundary algorithms allowing for the outward propagation of perturbations generated in the model domain, which would be the subject of a thesis on its own.

5.2.3 Flow in a 2.5 cm aneurysm.

We consider first a $R = 2.5$ cm aneurysm with a constant wall thickness of 1.5 mm. The fluid is Newtonian and the artery wall is described with a Mooney-Rivlin model. The material parameters are listed in Table 5.3.

The velocity field at three different moments of the cardiac cycle is depicted in Figure 5.6. As blood pulses in the artery [1], the peak velocity reaches 42 cm/s in the inlet and outlet segments that are not affected by the aneurysm (Remember that the boundary data plotted in Figure 3.14

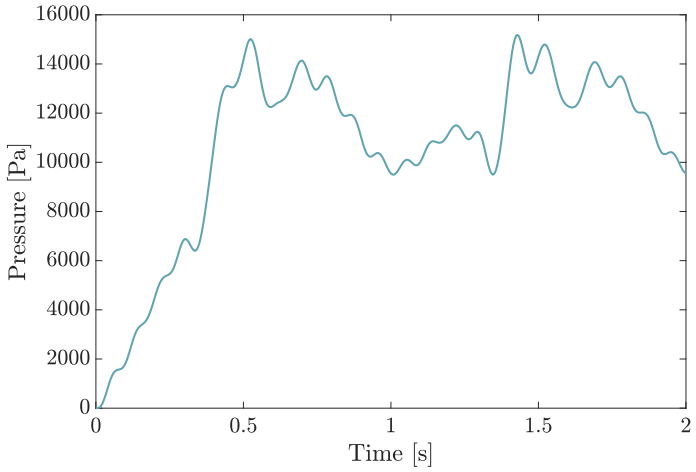

FIGURE 5.5 – Pressure evolution at the inlet of the artery during two consecutive cardiac cycles. The ramp during the initial 0.4 s is introduced to ensure a smooth start of the simulations with the progressive loading as pressure increases from zero to the physiological values. During the second cycle, after $t = 1$ s, the spurious oscillations are related to waves reflecting on the open boundaries of the model domain.

Parameters	*Values*	*Units*
Fluid density ρ^f	1050	kg/m^3
Dynamic viscosity μ	0.0038	Pa · s
Arterial wall density ρ^s	1200	kg/m^3
Arterial wall Young's modulus E	2.7	MPa
Mooney-Rivlin parameter C_1	0.584	MPa

TABLE 5.3 – Material parameters for the abdominal aortic aneurysm simulations.

are for the section averaged velocity.). By continuity, the velocity is much smaller in the aneurysm itself because of the increased cross section. The flow gently follows the contours of the artery and is essentially unidirectional. When the flow decreases, some weak vortices do however appear occasionally both in the entrance and exit cross sections of the aneurysm, where the wall curvature is greatest (2 and 3). A small counter-flow corresponding to the dicrotic notch is also observed at time $t' = t - T = 0.5$ s 2.

Wall stresses follow the evolution of pressure with time. The maximum values are therefore observed at the peak systolic pressure. The main effect of the internal pressure is to produce circumferential stresses and a smaller contribution to the longitudinal stresses. The maximum hoop stress reaches 2.49 10^5 Pa while the maximum von Mises equivalent stress is 2.23 10^5 Pa. The distribution (Figure 5.7) is symmetric around midsection with the maximum occurring around the inflection points of the wall, approximately one aneurysm radius away from the middle section. This pattern and the characteristic values closely align with the results of Scotti et al. [155] who study the same configuration and report a maximum equivalent von Mises stress of 2.38 10^5 Pa.

During the cardiac cycle the maximum displacement of the wall reaches 1.5 mm in the radial direction around the center of the aneurysm with little variation around this spot, which is also consistent with Scotti et al. [155] although their distribution shows the maximum displacement shortly off-centered.

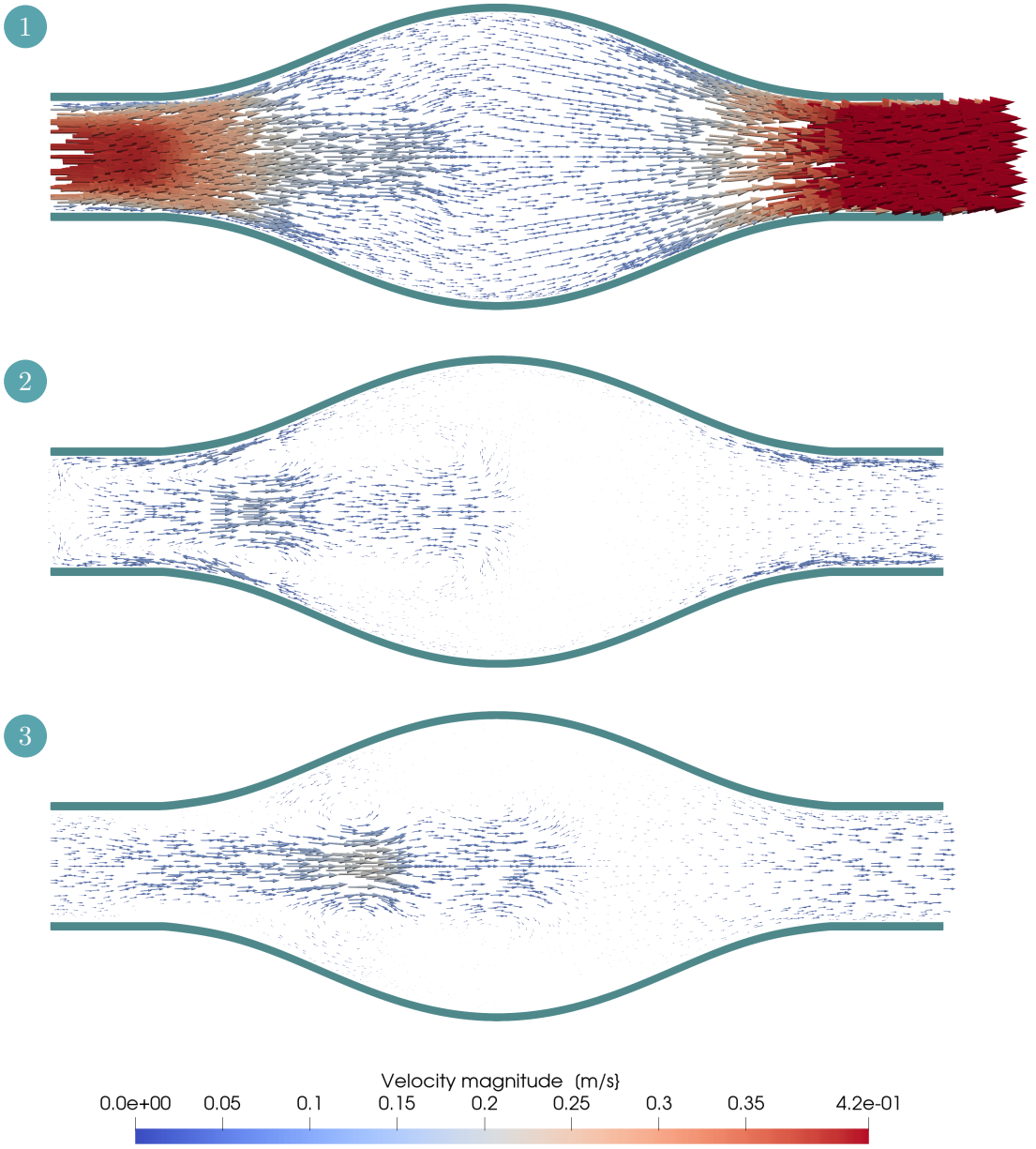

FIGURE 5.6 – Velocity field in the 2.5 cm aneurysm at the peak systolic flow (1 $t' = t - T = 0.32$ s) and two subsequent moments during diastole (2 $t' = 0.50$ s and 3 $t' = 0.70$ s).

5.2.4 Influence of the initial size of the aneurysm.

To go further with the analysis, we consider two other aneurysms with initial radii of 2 cm and 2.75 cm. All the other parameters are unchanged (thickness of the wall, boundary conditions, material parameters). The qualitative response is not modified so that we concentrate here on the quantitative differences between the different simulations. Results are shown in Figure 5.8.

Table 5.4 shows the maximum hoop stress, maximum equivalent von Mises stress, and the range of displacement at mid-aneurysm for the three sizes of the aneurysm. As expected, all the parameters increase with the size of the aneurysm.

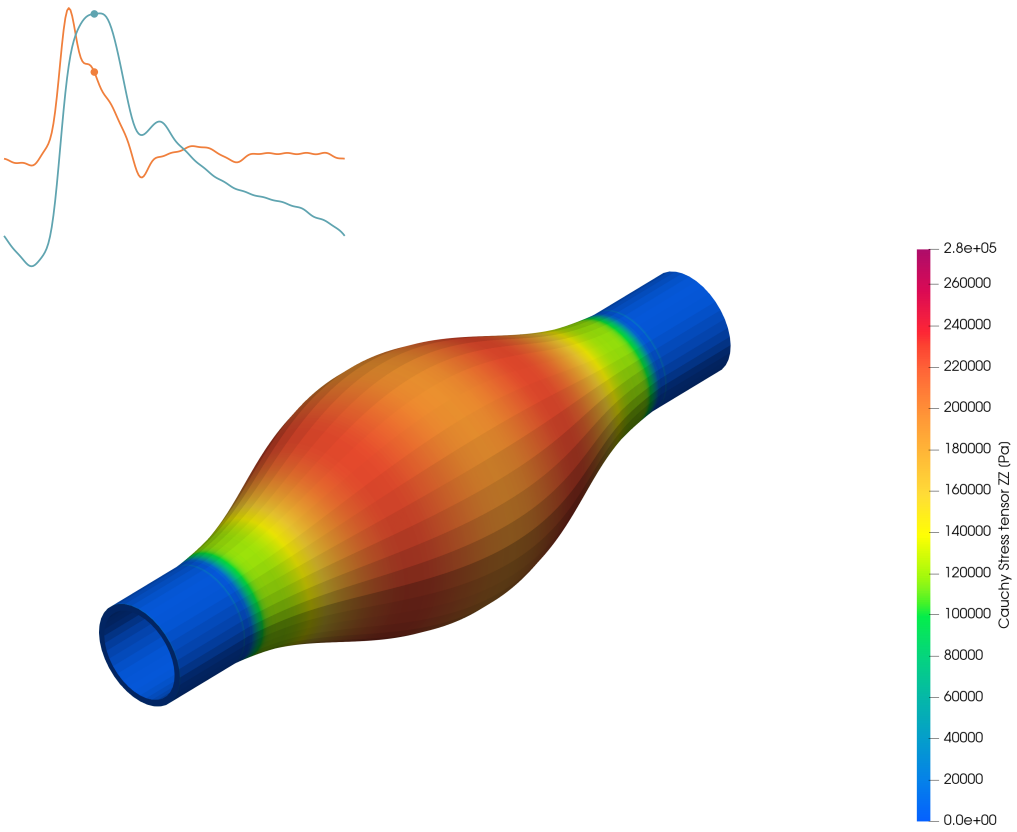

FIGURE 5.7 – Circumferential (hoop) stress at systolic pressure of the 2.5 cm aneurysm. The time of the snapshot is indicated on the inlet velocity (—) and outlet pressure (—) time series (Figures 3.14 and 3.15).

Initial radius R [cm]	σ_{zz} $[10^5 Pa]$	σ_{VM} $[10^5 Pa]$	Δr *[mm]*	
			min	max
2	2.02	1.799	0.72	1.12
2.5	2.49	2.230	0.89	1.50
2.75	2.77	2.496	1.02	1.66

TABLE 5.4 – Sensitivity of key parameters to the size of the aneurysm: maximum hoop stress (σ_{zz}), maximum equivalent von Mises stress (σ_{VM}), and displacement in the middle section of the aneurysm (Δr) (minimum displacement at diastolic pressure and maximum displacement at systolic pressure).

The increase in hoop stress and equivalent von Mises stresses with the radius of the aneurysm reflects the usual balance of forces in a cylindrical thin-walled vessel under pressure, *i.e.*,

$$\sigma_{hoop} = \frac{Rp}{t} \tag{5.4}$$

(where R is the radius of the vessel and t is the wall thickness). The aneurysm with the larger radius must resist a larger resultant force and is therefore the seat of large stresses. However, the stress grows slightly faster than the size of the aneurysm. This is most likely related to nonlinear geometric effects, including wall curvature in the radial plane, and the influence of fluid flow. This increase is potentially dangerous because it could induce greater deformation of the arterial

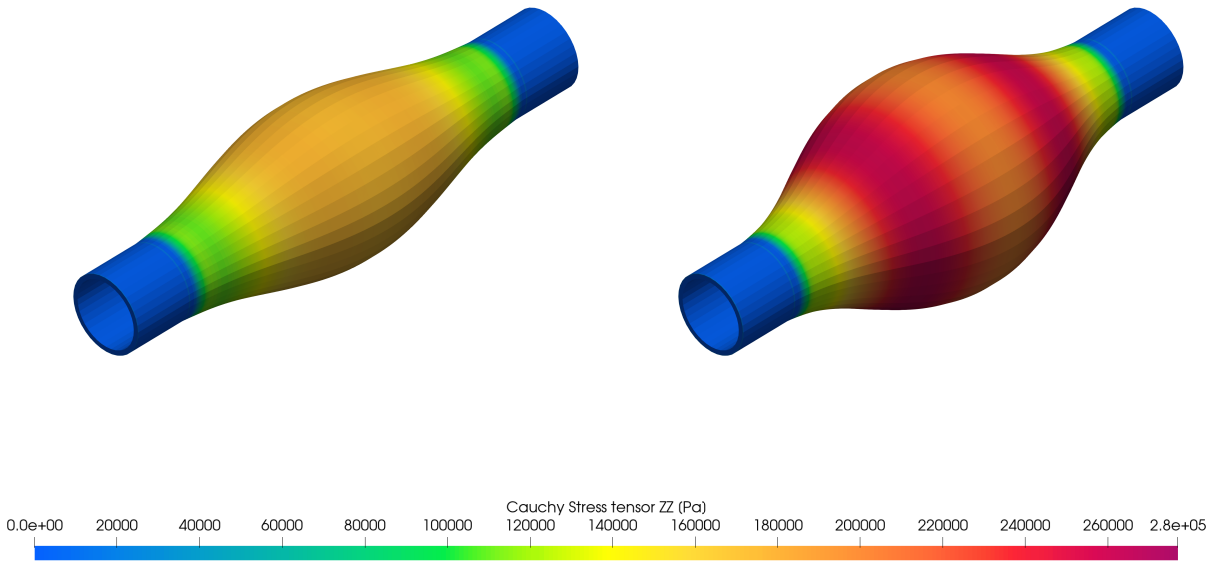

FIGURE 5.8 – Circumferential (hoop) stress at systolic pressure of the 2 cm aneurysm (left) and the 2.75 cm aneurysm (right).

wall, with even greater stresses. However, the maximum deformation in the middle section is seen to increase less than proportionally with the radius of the aneurysm, which ensures that the aneurysm remains stable, at least with the stiffness considered in the current simulations.

5.2.5 Three-layer model.

The wall of arteries and veins are essentially three-layer structures with each layer playing a distinct role in preserving vascular homeostasis and regulating the vascular response to stress or injury [168] (Figure 5.9). The inner layer, or intima, is formed of a thin layer of endothelium, which plays an important role in the regulation of blood pressure and substance transfer. It covers the luminal surface of blood vessels. The middle layer, or media, consists mainly of circumferentially aligned smooth muscle cells and elastic fibers and collagen. The outer layer, or adventitia, consist of an extracellular matrix scaffold of collagen fibers (oriented longitudinally as wavy bundles) with fibroblasts, nerve fibers, and immune cells. Tiny blood vessels (vasa vasorum) are also present in the wall of large vessels to nourish the wall cells [178]. The wall thickness and the proportion of the structural components in each layer vary among large, medium, and small-caliber arteries and veins. Large arteries (diameter $>$ 1 cm) contain a thick media layer and higher amount of elastin. Large arteries contain more elastin than collagen (1.5$\times$) tissue to stretch and recoil during the systole and diastole thereby propelling blood forward. The amount of elastin decreases in small arteries which in turn contain more smooth muscle cells [20].

Many studies simplified the aorta as a single-layer structure, with a uniform thickness and uniform material properties throughout the vessel. The three layers have however different mechanical properties and contribute thus differently to the vessel stiffness. We therefore refine the previous description of the artery wall by introducing a more realistic three-layer structure. The mechanical behaviors of the intima, media, and adventitia are described by the Mooney-Rivlin model but, following Simsek et al. [163], the Young's modulus of the three layers are assumed to be in the ratio 1/3/2. The thickness and model constants for the three layers are reported in Table 5.5.

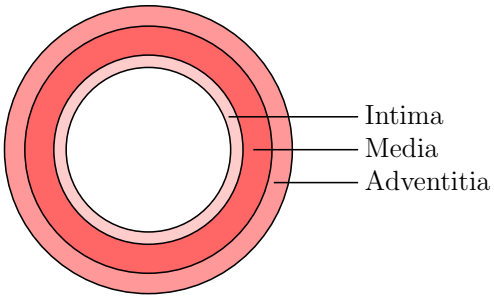

FIGURE 5.9 – Schematic view of the three layers of blood vessel wall.

Layer	*Relative thickness*	E MPa	C_1 MPa	C_2 MPa
Intima	0.20	1.174	0.254	-0.052
Media	0.47	3.522	0.762	-0.155
Adventitia	0.33	2.238	0.484	-0.098

TABLE 5.5 – Thickness, equivalent Young's modulus, and Mooney-Rivlin parameters for the three layers of the aneurysm wall.

The three layers deform together as a single solid and exhibit similar strains (ignoring the impact of geometric nonlinearities), *i.e.,* they work in parallel and the equivalent Young's modulus of the three-layer structure is the average of the individual moduli weighted by their relative thickness. The parameters listed in Table 5.5 ensure that the three-layer wall exhibits the same stiffness as the single-layer model considered initially. The main results of this three-layer model are reported in Table 5.6. They can be compared with the results of the single-layer model listed in Table 5.4.

Initial radius R [cm]	σ_{zz} $[10^5 Pa]$	σ_{VM} $[10^5 Pa]$	Δr *[mm]*	
			min	max
2	2.554	2.311	0.73	1.15
2.5	3.193	2.865	0.93	1.52
2.75	3.600	3.220	1.11	1.70

TABLE 5.6 – Key parameters of the tree-layer models of the aneurysm: maximum hoop stress (σ_{zz}), maximum equivalent von Mises stress (σ_{VM}), and displacement in the middle section of the aneurysm (Δr) (minimum displacement at diastolic pressure and maximum displacement at systolic pressure).

The refinement of the model does not influence the deformation of the aortic wall. The radial displacement in the midsection increases by less than 2% with the introduction of the three-layer structure, which is clearly not significant from physiological and mechanical points of view. The difference could also be linked to the increased spatial resolution used in the three-layer model.

The most interesting aspect of the refined model is related to the stress distribution. The results listed in Table 5.6 reveal much larger hoop stresses and equivalent von Mises stresses, about 25% larger, than in the model using only one layer.

A quick examination of a cross section through the middle of the arterial wall shows that the maximum hoop stress occurs in the thick and stiff media layer, which provides the greatest contribution to counteracting pressure forces (Figure 5.10). The intima, on the other hand, does not contribute significantly to the resistance of the wall. Its primary function is known to be the modulation of interactions between the blood and the artery wall, making its role more biological than mechanical.

Because of their different composition, the three layers exhibit different mechanical properties. In particular, the risk of rupture in each of these layers should be examined with respect to the ratio of the actual stress to the intrinsic ultimate stress of that layer.

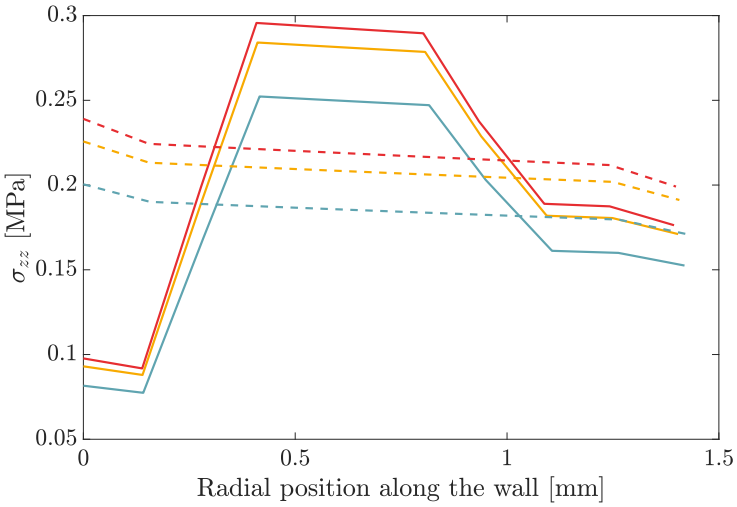

FIGURE 5.10 – Cauchy hoop stress (nodal values) variation along the wall for the 2 cm (——), 2.5 cm (——), and 2.75 cm (——) aneurysms. Data are taken in the radial direction, at the mid of the aneurysm sac, at the time of maximum hoop stress. Results correspond to the three-layer model (——) and single-layer model (- - -).

5.2.6 Aneurysm initiation and stability.

The dynamics of aneurysm proceeds at two different timescales. So far, we have considered the movements of the artery along the cardiac cycle. The initiation and progression of aneurysms proceed however with a longer timescale characterizing the biological transformations of the wall vessels. Aneurysms initiation can be caused by an initial weakness in the blood vessel wall, which may be present from birth in some cases, a high blood pressure also resulting in damage and weakening of blood vessels, atherosclerosis, or other diseases resulting in the weakening of the blood vessel wall [149]. The proper description of the corresponding mechanisms requires specific models of the evolution of the damage of the wall over periods of months and years.

There is a natural interplay between the models at the short and long timescales. Models of the cardiac cycle can describe the mechanical stress to which the cells of the artery walls are exposed, including the Wall Shear Stress (WSS) and the cycle of loading/unloading. These parameters are influenced by the geometry of the aneurysm and the stiffness of the artery wall. The latter are determined by the biological response occurring at the longer timescale.

In this section, we do not consider the longer timescales but touch upon two aspects of this two-timescale analysis. Figure 5.11 shows the Time-averaged Wall Shear Stress (T-WSS) and the maximum WSS computed in the three-layer model of the 2.75 cm aneurysm considered in the previous section. The results indicate a reduction of these parameters by a factor of three in the aneurysm with respect to the initial and terminal sections. The small values of the wall shear stress (T-WSS < 0.4 Pa) experienced by the endothelial cells in the sac of large scale aneurysms are known to create an environment that is favorable to the deposition of plaque and atherosclerosis [112]. This kind of result can be used as an input to a longer timescale model describing the evolution of atherosclerosis on the artery wall.

The information on wall shear stress provided by numerical models is valuable because wall shear stress cannot be measured in vivo. Most estimates rely indeed on Poiseuille's law to calculate wall shear stress from blood velocity measured by echo Doppler ultrasound. This is, of course, a crude approximation because it ignores local dynamic and geometric effects, and assumes a constant and fully developed flow.

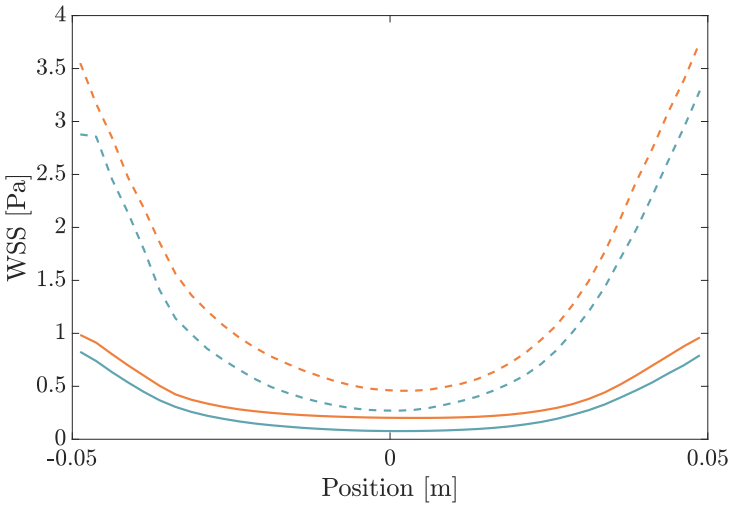

FIGURE 5.11 – Time-averaged wall shear stress (——) and maximum wall shear stress (- - -) along the artery segment (for the 2.75 cm three-layer aneurysm) computed using a Newtonian model (——) and a Casson (——) fluid model ($\tau_y = 0.0035$ Pa and $\mu_\infty = 0.0038$ Pa $\cdot$ s).

From a methodological point of view, the results also suggest that the constitutive equation used to describe the blood rheology matters. While the hoop stress and deformation of the aneurysm are insensitive to the choice between a Newtonian or a Casson fluid model, the time-averaged and maximum WSS values computed with the Casson fluid assumption are, respectively, 22% and 13% higher than the corresponding results computed with a Newtonian model. Given the clinical significance of WSS in atherosclerosis diagnosis, the use of the more realistic Casson fluid model is therefore recommended when assessing the stress acting on endothelial cells.

As already mentioned in section 5.2.1, we suggest that the stability of the aneurysm depends on the appropriate increase of the stiffness of the artery wall to compensate for the initial problem responsible for the creation of the aneurysm. To illustrate this claim, we first consider two sets of simulations of a straight artery with a spatially variable thickness of the wall.

The heterogeneity of the wall, especially its thickness, is known to be a significant factor in the risk of AAA rupture. Accurately assessing thickness in patient-specific CT images is challenging due to calcification, thrombus, and indistinct image definition between the inner and outer wall surfaces. However, experimental sampling of wall specimens has revealed that the wall is indeed non-uniform, thinning in response to pulsatility and the progressive expansion of the aneurysm sac [155, 192]. We consider here local thinning as a potential cause of aneurysm initiation.

In the first two models, the wall thickness is assumed to decrease from the nominal value of 1.5 mm at the two extremities of the aortic segment to a local minimum of 1 mm in its center section. The flow is then modeled as previously with either a 0.675 MPa Young's modulus, characteristic of the unperturbed artery wall, or with a higher value of 2.7 MPa that is generally measured in aneurysm walls.

The results shown in Figure 5.12 illustrate the impact of the stiffness of the artery wall on the initiation of the aneurysm. If the local thinning of the artery is not compensated by an increase of its Young's modulus, the artery wall experiences significant deformations. A maximum radial displacement of 4.20 mm is computed here. If, however, biological remodeling occurs and the Young's modulus increases thanks to the replacement of elastin by collagen, such large deformations can be avoided. Here, a maximum of only 0.52 mm is obtained with the stiffer

wall. The deformation not only decreases on account of this physiological adaptation but also the maximum hoop stress. In Figure 5.12, this stress component peaks at 0.17 MPa for the adapted artery while the hoop stress reaches 0.33 MPa in the more flexible aorta. These results clearly demonstrate the relevance of the adaptation of the stiffness of the artery to mitigate the influence of a local thinning.

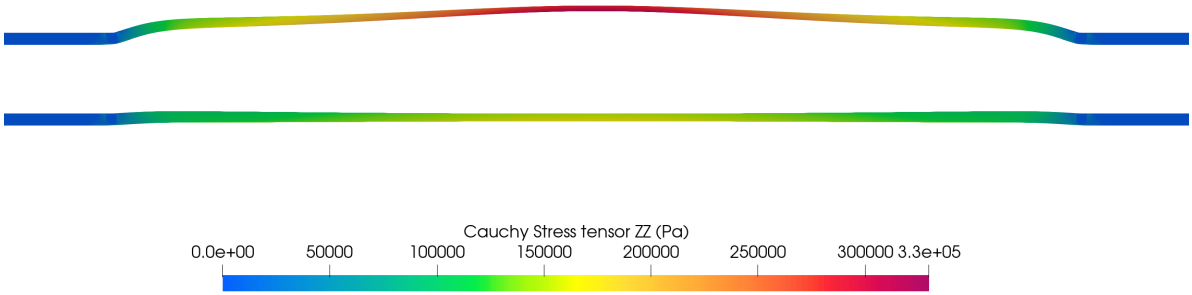

FIGURE 5.12 – Deformation and hoop stress in a straight artery segment with a local decreased thickness of 1 mm in the central section at the peak systolic pressure. The upper figure is computed with a Young's modulus of 0.675 MPa, while the lower one shows the behavior of the stiffer wall ($E = 2.7$ MPa).

Reducing the wall thickness to 0.75 mm in the central section leads to even more disastrous outcomes (Figure 5.13). A stiffer artery, with a modulus of elasticity $E = 2.7$ MPa, can withstand systolic blood pressure without pathological deformation or stress. However, a more flexible artery ($E = 0.675$ MPa) forms a significant bulge, experiencing both extensive deformation and stress. Owing to the Poisson effect, the wall thickness reduces even more, increasing the hoop stress and ultimately causing the aneurysm to rupture.

5.3 Rupture of aneurysms.

A comprehensive understanding of the different factors contributing to the propagation of the aneurysm is crucial for the appropriate clinical handling. The surgical criteria for elective AAA repair must carefully consider the risk of rupture against the risk of the repair procedure. Surgery presents indeed an in-hospital mortality rate of about 3–5 % for open repair and 1–2 % for endovascular repair [186]. Clinicians therefore face the challenge of determining when the risk of AAA rupture outweighs the risks associated with the repair.

The size of the aneurysm is a universally recognized factor to forecast rupture. For abdominal aortic aneurysms, the European Society for Vascular Surgery recommends surgery at a maximum aortic diameter of 55 mm for men and 50 mm for females and patients with increased probability of rupture [57, 121]. The American Heart Association identifies age, gender, hypertension, smoking, and family history as factors that must be considered when assessing the pertinence of a surgical operation [180].

Size is not the whole story: 13% of AAAs with a diameter smaller than 50 mm rupture while 60% of AAAs with a diameter greater than 50 mm remain stable during the patient's lifetime [38, 57]. Although easy to use in practice, these statistics suggest that the size of the aneurysm is probably not the sole useful criterion for risk of rupture.

In addition to the diameter, the expansion rate of an aneurysm is a significant factor in assessing the risk of rupture. An expansion rate exceeding 10 mm per year is considered critical for an abdominal aortic aneurysm. However, the expansion rate might not always be available for clinical assessment due to the requirement for historical patient data [57, 121]. Ideally, the decision

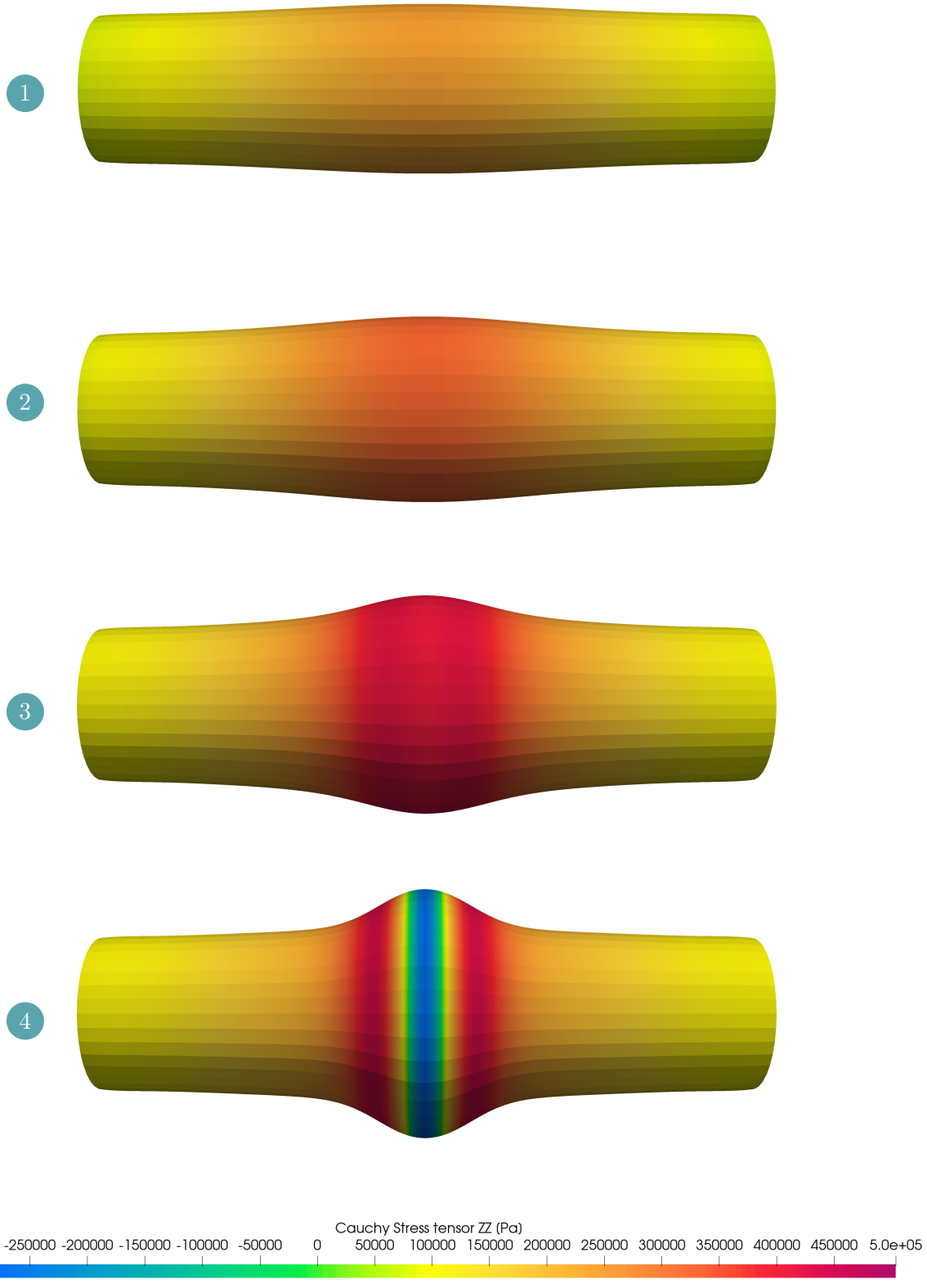

FIGURE 5.13 – Deformation and hoop stress in a straight artery segment with a local decreased thickness of 0.75 mm in the central section at four successive moments of the cardiac cycle: 1 $t = 0.395$ s, 2 $t = 0.445$ s, 3 $t = 0.465$ s, and 4 $t = 0.475$ s.

to repair an aneurysm should not be guided by maximum transversal dimension and expansion rate alone, but rather by a more reliable criterion associated with the actual rupture potential of the patient-specific artery. Although not directly measurable in vivo, stresses on the aneurysmal wall are believed to be a better rupture risk index and offers better data for surgical evaluation than size and growth rate [52, 70]. As illustrated in the previous section, the highest stress can indeed greatly vary despite identical maximum diameter and similar blood pressure. The wall of an aneurysm is a living and metabolizing structure, able to add and reinforce itself [163]. Enlargement does not necessarily imply increasing the risk of rupture.

The use of peak wall stress as a potential predictor of AAA rupture has been explored in several studies. Raghavan et al. [139], for example, found that the peak wall stress for AAAs which either ruptured or were symptomatic was significantly greater than the peak wall stress in electively repaired or asymptomatic AAAs. It is therefore a superior measure than maximum diameter for predicting patients with an unfavorable outcome. The authors also report that the location of peak wall stress is not the point of maximum diameter, but in the posterolateral part of the AAA, which coincides with the area of rupture in patients.

The actual risk of rupture depends on the ratio of wall stress to the estimated local wall strength, which defines the Peak Wall Rupture Index (PWRI) [164]. Wall strength does not only vary from patient to patient but also significantly within the same aneurysm. Therefore, wall strength must be carefully evaluated on a patient-specific basis to accurately predict the rupture potential of individual aneurysms [70, 190, 194]

Many numerical studies use the von Mises equivalent stress in the abdominal aneurysm as rupture criterion [155, 175]. However, the use of this comparison value seems to be dictated more by ease of use and simple adaptation of fracture criteria for metallic materials than by arguments linked to the mechanical study of biological tissues. The use of the peak principal stress seems to be much more appropriate to estimate where and when rupture will occur, as reported by many studies [52, 53, 195].

5.3.1 Numerical modeling.

The specific implementation of Metafor used in this work allows the definition of different rupture criteria and the explicit modeling of this rupture [137]. In Metafor, rupture can also be deemed to occur when any component of the stress tensor, its average value, the maximum value over all the Gauss points in the element, or at a single Gauss point is greater than a critical value. In line with the above discussion, rupture of the artery wall is assumed here to occur when the greatest principal component of the stress tensor in a given element exceeds a given threshold, on average over the different Gauss points of the considered element.

When the rupture criterion is reached, the corresponding element is simply deleted from the discretization and the deformation and stress fields are updated accordingly. The corresponding change in geometry is taken into account in coupled fluid-structure simulations by extending the FSI interface with the new external nodes created by deleting the ruptured solid finite elements. In the same move, the fluid elements that no longer have a solid counterpart are transformed into free surface elements. Then, it is checked which solid node doesn't have an equivalent on the fluid side and it is added on the fluid side. PFEM nodes can also be removed in this process.

In addition to the definition of the rupture criterion, the coupling code between the fluid and solid parts requires a couple of adjustments to account for rupture. First, for technical reasons, in the current implementation, the FSI interface must be adjusted to encompass the entire solid, since fluid-solid contact is no longer limited to the inner surface of the solid. Once the arterial wall is ruptured, blood can flow along the outer surface of the artery. Second, the simple mechanism

described in the previous paragraph asks for a complete matching between the fluid and solid elements along the FSI interface (Figure 5.14). The discretizations of the two subdomains must therefore be adapted. Thanks to the matching discretizations, the mapping of displacement and surface forces on the fluid and solid sides is straightforward.

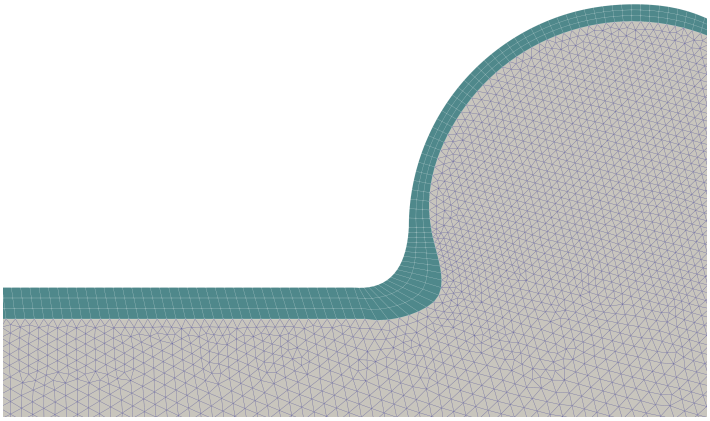

FIGURE 5.14 – Matching fluid and solid meshes. The fluid and solid meshes share the same set of nodes along their common boundary. Since consistent displacements are prescribed through the coupling algorithm, shared nodes move in a consistent way, which simplifies the interpolation.

It turns out that the most important factor for a successful fracture simulation is that the finite elements inside the solid should be approximately (in 2D) square elements with a side of the same order of magnitude as the characteristic size of the fluid elements. Since interior elements are likely to be exposed, the discretization of the fluid and the solid must match not only along the initial FSI boundary, but also within the two subdomains.

In this section, the feasibility of this methodology is demonstrated for two different geometries.

5.3.2 Rupture of a 2D cerebral aneurysm.

As a first demonstration of the capability of the code to model the rupture of a blood vessel, we consider the 2D plane strain model of a cerebral aneurysm schematized in Figure 5.15. The geometry describes a semi-circular aneurysm on the side of a cerebral vessel and is adapted from Sun et al. [172] (so called *cerebral berry aneurysm*). The real dimensions used by Sun et al. [172] are reported in Table 5.7.

Such a 2D model is greatly simplified as it fails to capture the real balance of forces present in 3D configurations. Specifically, it does not account for the dominant component of the stress tensor, the hoop stress, and how it varies with the local radius of a blood vessel. Consequently, this model should be regarded as a tool model to demonstrate the modeling of rupture. We therefore feel free to introduce more simplifications that make the model further depart from the real problem.

While it was advocated above that the rupture criterion should be based on the largest principal stress, the equivalent von Mises stress is considered here in this preliminary study. In practice, rupture of an element is assumed to occur when the average equivalent von Mises stress over the Gauss points exceeds 0.2 MPa.

No slip boundary conditions are applied on the straight outer boundary of the vessel and on the FSI interface (Figure 5.15). The fluid model is forced by prescribing the inlet velocity and the outlet pressure. Starting from rest, the flow is allowed to develop for 0.2 s until a velocity

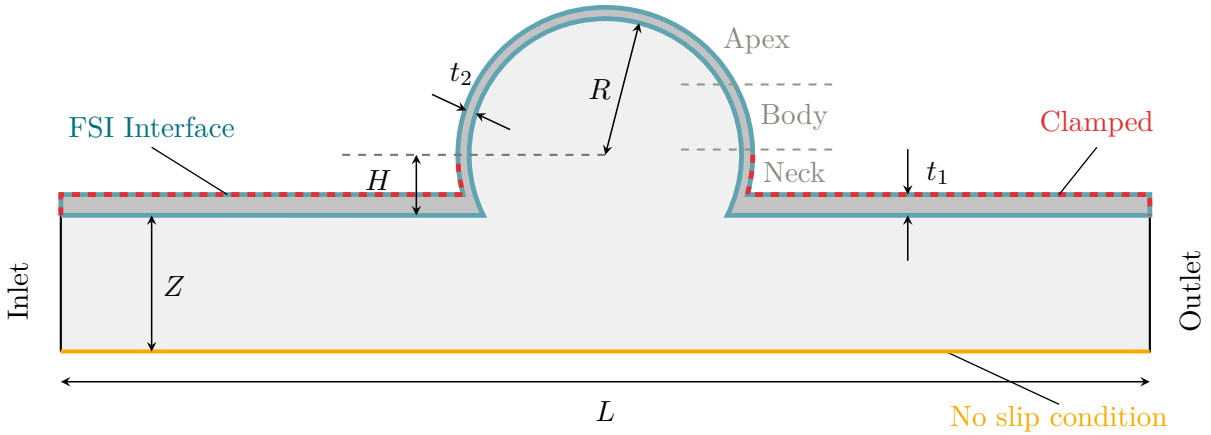

FIGURE 5.15 – Simplified cerebral berry aneurysm geometry with fluid domain ( ), solid domain (■), and boundary conditions (clamped (- - -), FSI interface (—), and no slip condition (—)).

Parameters	*Values*	*Units*
Length L	28.8	mm
Width Z	3.6	mm
Height H	1.6	mm
Wall thickness t_1	0.55	mm
Aneurysm thickness t_2	0.3	mm
Aneurysm radius R	3.6	mm

TABLE 5.7 – Geometrical parameters for the cerebral berry aneurysm simulations.

of 45 cm/s is reached in the main segment of the vessel. A linear increase of pressure is then prescribed via the outlet boundary condition. A peak of 100 mmHg is reached at time $t = 0.5$ s.

A hypoelastic linear model of the walls of the vessels is used with $E = 5$ MPa. Since the simplified 2D geometry does not allow for hoop stresses to balance the internal pressure, the non-dilated part of the vessel wall is fixed on its outer boundary. While the whole upper wall is considered in the solid model, only the aneurysm region is therefore allowed to deform under the internal pressure and flow.

The model lacks the right features to predict where rupture will occur. We therefore rely on the work of Crompton et al. [36], who analyzed the location of rupture in 289 cerebral aneurysms. In this work, the observed aneurysms are divided lengthwise from the origin to the top of the artery into three equal thirds. The proximal third adjacent to the parent artery is called the neck, the middle third is the body, and the distal third is the apex. Rupture has been observed to occur predominantly through the apex of cerebral aneurysms. Figure 5.16 shows the typical pattern of a ruptured cerebral aneurysm.

To ensure that the model describes the rupture of the aneurysm at a physiologically meaningful location and not in the regions where the fixed boundary conditions are applied to the solid, the wall thickness is increased along the straight part of the vessel and at the base of the aneurysm. In contrast, a local weakening of the aneurysm wall is simulated by introducing a 25% decrease in wall thickness where rupture is reported in clinical observations.

Figure 5.17 shows the results of the simulation. Figure 5.18 shows the initial flow in the blood vessel with a well developed flow in the straight part and a vortex flushing the aneurysm region. The reduced thickness around the apex can be seen to induce a local maximum of the equivalent

FIGURE 5.16 – Clinical observation of a ruptured cerebral aneurysm [71].

von Mises stress ❶. When blood pressure increases, the rupture threshold is first reached in the corresponding element, which is therefore deleted ❷. Blood is then accelerated through the hole in the vessel by the very large pressure gradient existing between the inner and outer regions. Blood is ejected at a very high velocity that quickly exceeds 5 m/s. At the same time, the stresses in the artery wall decrease sharply as the pressure inside the aneurysm drops ❸.

The steep pressure gradient between the ends of the vessel and the aneurysm causes a significant increase in flow velocity in the straight portion of the vessel. The boundary condition on the velocity imposed at the entrance of the cerebral artery limits the flow rate, so the blood rushes away from the downstream boundary toward the aneurysm and the hole in it.

The rupture of the aneurysm separates the two parts of the wall, which loses its stiffness and deforms significantly as the two parts move apart at approximately 3 m/s (see velocity field in Figure 5.19). This rapid movement creates significant stresses at the base of the aneurysm, resulting in a new, somewhat artificial rupture at this point in the last subfigure ❹.

5.3.3 Rupture of an axisymmetric abdominal aortic aneurysm.

Building on the success of the first rupture simulation described in the previous section, we return here to the modeling of the axisymmetric abdominal aneurysm described earlier in this chapter (Fig. 5.2).

Although real aneurysms often have a more complex, truly 3D geometry, the axisymmetric model provides a fair description of many of the features of real aneurysms [154]. However, axisymmetric rupture of an aneurysm is much less realistic because it implies that the two parts of the vessel are completely separated when rupture occurs. In general, rupture occurs around some weak point in the arterial wall.

Despite its inherent limitations, the axisymmetric model provides a much more realistic framework than the strictly two-dimensional model considered previously. Of particular significance is the ability of the model to represent the balance of forces by accounting for the dominant hoop stress in the artery wall and the dependency of this stress component on the radius of the deformed vessel. A 2 cm aneurysm with a uniform wall thickness and a Mooney-Rivlin model ($C_1 = 0.584$ MPa, $C_2 = -0.1185$ MPa, corresponding to $E = 2.7$ MPa) of the artery material is considered.

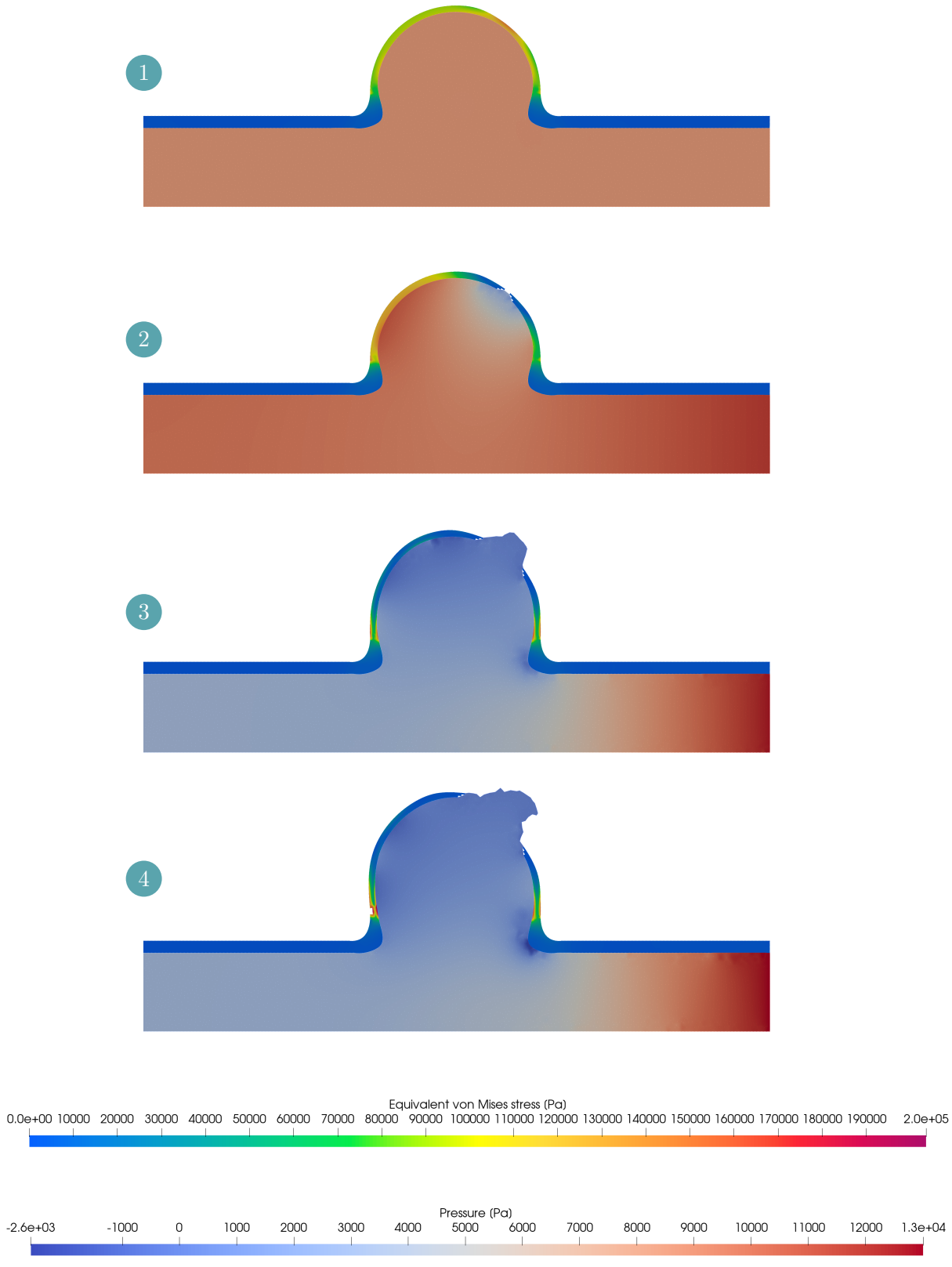

FIGURE 5.17 – Deformation and rupture of a cerebral berry aneurysm at four successive times: ❶ $t = 0.4780$ s, ❷ $t = 0.4785$ s, ❸ $t = 0.4910$ s, and ❹ $t = 0.4955$ s. Rupture occurs in the apex region of the aneurysm.

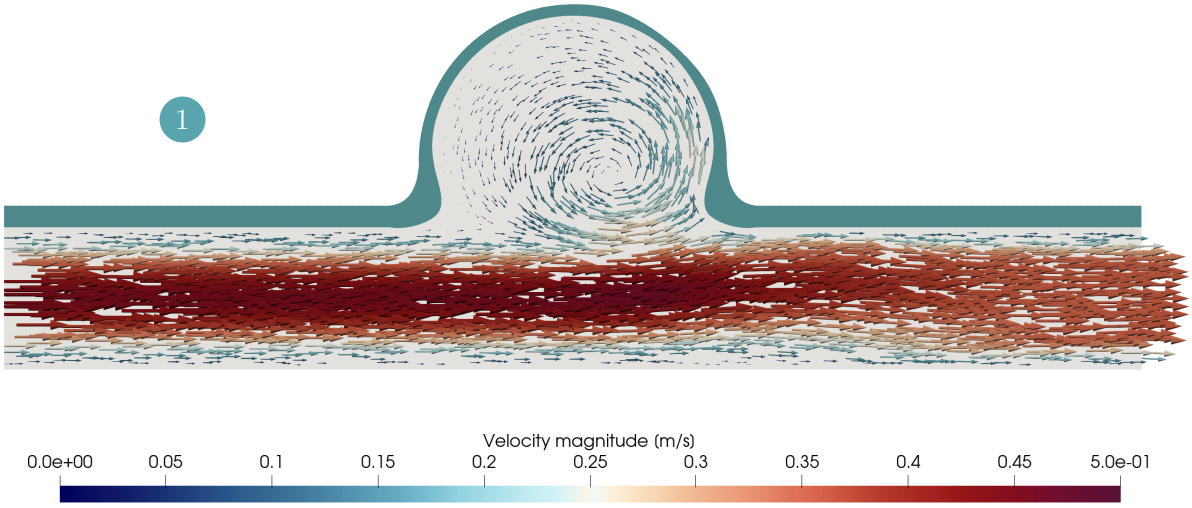

FIGURE 5.18 – Velocity field in a cerebral berry aneurysm at time $t = 0.4780$ s (subfigure 1 of Figure 5.17).

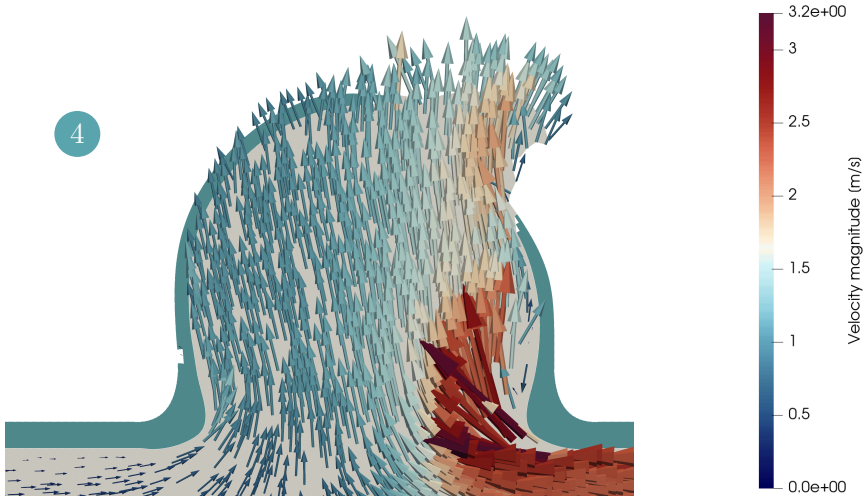

FIGURE 5.19 – Velocity field in a cerebral berry aneurysm at time $t = 0.4955$ s (zoom on the hole of subfigure 4 of Figure 5.17).

As indicated in section 5.2.3, the Cauchy stress tensor in an axisymmetric model comprises only the components σ_{xx}, σ_{yy}, σ_{xy}, and σ_{zz}, with the hoop stress σ_{zz} taking much larger values than the other components and acting out of plane with respect to the three other components. As a result, it is the greatest principal stress to be used in the rupture criterion. In this section, we consider that rupture occurs when the hoop stress reaches a value of 0.18 MPa on average over the integration points of an element. Note that this value does not have a true clinical meaning but is used here for demonstration purposes. In practice, the accurate modeling of rupture would require the knowledge of the wall strength, which as reported in the introduction to aneurysm rupture, must be evaluated on a patient-specific basis. This critical value is somewhat arbitrarily chosen for the sole purpose of highlighting the fracture phenomenon, but is nevertheless of the same order of magnitude as the peak stress threshold of 0.28 MPa reported by Vorp et al. [194]

Rupture of the axisymmetric aneurysm is illustrated in a dedicated simulation similar to the numerical experiment carried out with the cerebral aneurysm in the previous section. The flow is allowed to develop in the blood vessel during the initialization phase and pressure is increased gradually until rupture occurs. In order to improve one of the aspects of the cerebral aneurysm simulation, the boundary conditions are modified to avoid constraining the velocity in the inlet section and allow the corresponding inflow to increase when rupture occurs. The model is forced by imposing the evolution of pressure at both the inlet and the outlet. A pressure signal gradually increasing to a value of 100 mmHg is prescribed, but with a phase shift of 0.004 s between the inlet and outlet sections. This describes the propagation of a progressive wave along the artery.

The deformation, rupture, and outward bleeding of the aneurysm simulated under this forcing are shown in Figure 5.20. The second subfigure reveals that rupture does not occur where the diameter of the aneurysm is maximum, but around an inflection point of the aneurysm (2). This clearly reflects the stress distribution already observed in section 5.2.3 and in Figure 5.7. Contrary to the numerical experiment with the cerebral aneurysm, nothing is done here to trigger the rupture of the artery wall at this location. This provides an interesting validation of the model. The results are in agreement with the experimental study carried out by Doyle et al. [45]. By analyzing the location of the rupture of abdominal aortic aneurysms, they also observe that rupture occurs around an inflection point of the aneurysm sac and not in the middle section. This can also be observed in Figure 5.20.

The occurrence of rupture on the distal part, rather than the proximal part, indicates that while the stress distribution around the middle section is roughly symmetrical, it is not perfectly so, displaying a slight asymmetry due to the dynamics of blood flow within the artery.

The significant pressure difference across the artery wall causes blood to be ejected at approximately 3 m/s through the ruptured element (3). Concurrently, pressure within the artery near the leak decreases, and this pressure gradient relative to the inlet region causes a swift increase in blood flow within the artery. Approximately 3 ms post-rupture, the velocity at the inlet region doubles, surpassing 1 m/s, resulting in a rapid influx of blood from the upstream region into the aneurysm.

With the drop of blood pressure, the forces on the artery wall also decrease sharply, which can be observed on the hoop stress distribution. The later increase of the hoop stress observed in subfigure 4 while blood continues to be ejected through the hole is a numerical artifact (4). The sudden rupture of the artery wall creates a negative pressure wave that propagates through the model domain. Because the inlet pressure is prescribed by the boundary condition, the expansion wave bounces on this boundary and is reflected as a compression wave that affects the whole domain by artificially increasing pressure in the artery.

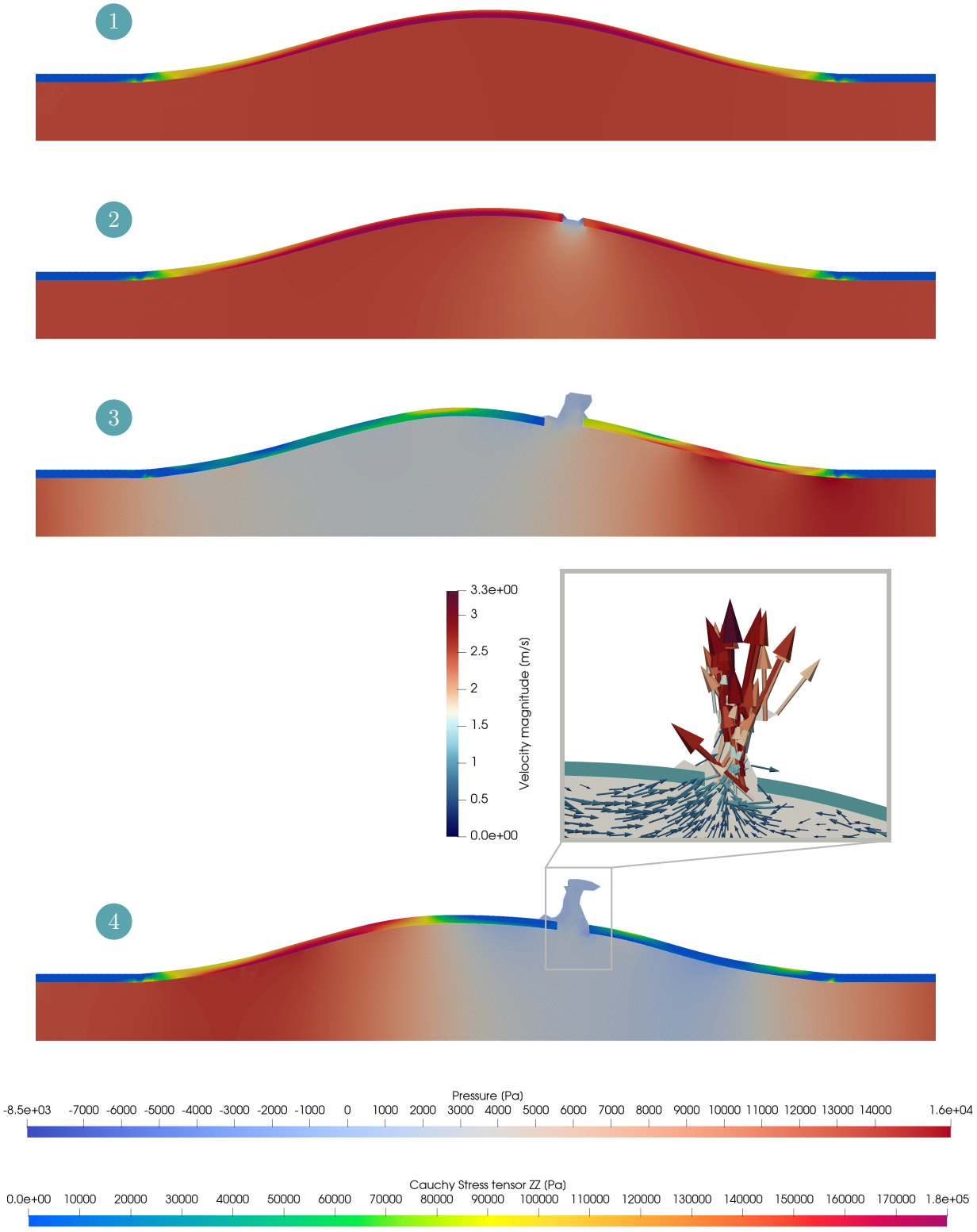

FIGURE 5.20 – Deformation and rupture of an axisymmetric abdominal aneurysm at four successive times: ❶ $t = 0.1085$ s, ❷ $t = 0.1090$ s, ❸ $t = 0.1120$ s, and ❹ $t = 0.1135$ s (with zoom on the hole with velocity field). Blood flows from left to right.

CONCLUSIONS AND PERSPECTIVES

Conclusions.

The aim of this work was to demonstrate the possibilities offered by the Particulate Finite Element Method (PFEM) and the modeling of fluid-structure interactions in the context of the study of the cardiovascular system. This objective is achieved by studying a series of problems ranging from blood ejection from the heart through the aortic valve, blood flow in healthy arteries and veins, and the dynamics of an abdominal aortic aneurysm including its ultimate rupture. From the author's knowledge, it is the first time that the PFEM is applied to problems of this kind.

While chapter 2 provides a stand-alone introduction to the PFEM3D and Metafor codes and their coupling strategy in the framework of FSPC, this work has deliberately attacked the problems not merely from a purely numerical point of view, but rather from an application point of view. This approach is indeed thought to provide more relevant insights into the real potential of the PFEM to aid the understanding of phenomena related to blood circulation.

The third chapter provides an extensive analysis of the constitutive equations used to describe the rheology of blood and the mechanics of artery walls. On the one hand, the chapter shows how the non-Newtonian behavior of blood (with shear thinning and yield stress) can be taken into account using a Casson model. The capabilities of PFEM3D have been augmented by the implementation and verification of this model. On the other hand, the various constitutive laws used in the literature to describe the complex mechanical behavior of artery walls are also presented in this chapter.

After an initial demonstration of the ability of the coupled model to describe the propagation of a pressure pulse in an axisymmetric elastic artery and its verification against the Moens-Korteweg equation, the pertinence and influence of the different relevant constitutive laws available in the codes were investigated. A realistic pulsatile flow in a straight artery of 2 cm diameter was studied and used for this purpose.

The results show that blood in large arteries behaves as a Newtonian fluid and that there is no need to resort to a Casson-type constitutive equation for such flow. This result is due to two reasons. The high shear rates encountered in this type of flow mean that the apparent viscosity is virtually constant. The non-stationary and even pulsatile nature of these flows also implies that viscosity plays a relatively minor part. Simulations of the flow in the much less dynamic inferior vena cava show however that the Casson model has a significant influence when the shear rate and the Womersley number are small.

The choice between a Hookean, Neo-Hookean, or Mooney-Rivlin model of the arterial wall also proved to have little effect on the displacement of the wall. However, the results suggest that

modeling the elastic behavior of the wall could have an influence on the wall shear stress exerted by the fluid, which is known to be a very relevant parameter for the onset and propagation of atherosclerosis.

The fourth chapter focuses on the modeling of a two-dimensional plane strain aortic valve. While the simplification of the geometry associated with the 2D model comes with an important modification of the dynamics of the valve, the model succeeds in reproducing the qualitative behavior of the ejection of blood from the left ventricle and the opening and closing of the aortic valve as a result of the pressure difference between the left ventricle and the aorta. The effect of calcification has been introduced in the model by increasing the thickness of the leaflets. The results of the corresponding simulations show a good qualitative agreement with previous studies. Calcification impacts the heart ability to pump blood throughout the body by decreasing the opening of the valve and the duration of the ejection phase, which has a significant impact on the stroke volume.

The dynamics of the abdominal aortic aneurysm is addressed in chapter five. Models of increasing complexity are considered, using either a simple linear elastic model or a Mooney-Rivlin constitutive equation of the aortic wall, with uniform or space varying properties of the wall. In spite of the limitations of the axisymmetric approach, this study provides very valuable information about the necessary adaptation of the properties of the aortic wall to compensate for the occurrence of a local defect. The local thinning of the wall can trigger an instability of a straight artery segment, with large deformations and, ultimately, rupture of the aneurysm if the Young's modulus of the arterial wall does not increase to compensate for the initial defect. There is a clear nonlinear geometrical effect behind this instability. Any increase of the local radius of the artery goes with an increase of the hoop stress, which triggers further elongation of the artery wall. Such large deformations and instability can be avoided if biological remodeling occurs, and the Young's modulus increases thanks to the replacement of elastin by collagen. These findings, along with the identification of regions susceptible to atherosclerosis, hold great promise for accurately assessing the risk of aneurysm rupture and making decisions regarding the always risky surgical interventions.

Finally, the ability of the code to describe the rupture of an aneurysm has been demonstrated with two different geometries. In particular, we modeled the rupture of a cerebral aneurysm at its apex and showed that, in line with clinical and experimental results, the axisymmetric abdominal aneurysm is more likely to rupture around an inflection point.

Perspectives.

The various models developed in this study highlight the potential of PFEM3D and Metafor, and of their coupling in the FSPC framework, to enhance our understanding of hemodynamics and biomechanical processes. This offers significant promise for diagnosing cardiovascular conditions and developing new therapeutic methods that could improve patient care. However, there are still numerous limitations that constrain the pertinence of the results and the practical application of these numerical tools in a clinical setting.

A first set of useful or necessary improvements are related to the numerical tool itself.

- As illustrated by the simulation of the opening of the aortic valve, some physiological flows are turbulent and therefore require a proper modeling of the corresponding phenomena.

  Simple zero-equation models are unsuitable due to the extensive separated regions and significant curvature effects present in turbulent blood flow modeling. Although it will require

more computational time, incorporating a two-equation $k - \epsilon$ model into PFEM3D would enhance the model versatility.

Alternatively, considering that blood flows are only weakly turbulent, a shift towards Large Eddy Simulations (LES) might be considered. This approach would demand higher spatial and temporal resolutions, along with the adoption of Smagorinsky-type modeling for subgrid scales.

- The different simulations also emphasize the need to improve handling of boundary conditions. Most of the developments and applications of PFEM3D addressed either very viscous flows or flows that were not driven by the boundary conditions. Blood flows represent a completely different framework in which open boundary conditions play a significant part in the dynamics.

  The ability of the code to cope with signal propagating through the model domain and radiating to the outside is of particular importance. A first objective, therefore, should be to implement radiation boundary conditions allowing disturbances generated in the model domain to leave the region of interest without bouncing on the boundaries and spoiling the computed solution. There is a vast literature about such treatments in many application fields of fluid mechanics and electromagnetism. Some of the solutions developed in these contexts (*e.g.,* sponge layer with a local artificial increase of the viscosity to damp outgoing signals [82]) should be implemented in PFEM3D.

  A second objective is to give the user more flexibility in the treatment and definition of boundary conditions. The flow in the aorta, for instance, is not limited to a simple progressive wave but is also influenced by reflection occurring downstream. It would therefore be interesting to couple PFEM3D to simplified models of the rest of the circulatory system. A common strategy reported in several studies is to couple the boundary condition with a Windkessel model, *i.e.,* a lumped model of the circulation [195]. The implementation of Windkessel model as downstream boundary conditions in artery modeling has demonstrated the possibility to reproduce patient-specific flow data. By adding resistance and compliance at the distal vasculature, aorta models equipped with a Windkessel model can prevent backflow, especially during diastole when the ventricle is relaxed and there is no pressure driving the blood flow [67, 123].

- Blood flow simulations can run for hours, even in 2D, and a significant part of the computation time must be invested in the initialization of the model. In this context, it would be very beneficial to provide the whole model system (PFEM3D, Metafor, and their coupling through FSPC) with an option to restart a simulation and not to start every simulation from zero or from initial conditions that can be expressed analytically.

Considering their large numerical cost, 3D simulations have not been carried out in this work. While no specific difficulties are anticipated, except the computational load, three-dimensional models of the aortic valve, of arteries and aneurysms would of course allow to increase the fidelity of the simulations with the real physiology and open the way for the practical use of numerical simulations by the clinician.

Three-dimensional models would include the real geometry of blood vessels, with their tortuosity, curvature, details of branching, and local variations of the material properties of their wall that have been found to impact physiologically relevant parameters like the wall shear stress. In the future, simple 3D models and, even more preferably, actual patient-specific geometries reconstructed from imaging data should also be considered.

Such next generation models should also take into account the anisotropic behavior of the biological tissues of the cardiovascular system. In order to account for the realistic material properties of the aortic wall, aneurysmal tissue, and aortic leaflet tissue, the use of a nonlinear, anisotropic, viscoelastic material property should be investigated. This means modeling and taking into account the non-collagenous matrix with embedded collagen fibers.

Most importantly however, the model should be extensively validated against experimental data before being applied to tackle real patients issues. Such data are for instance particularly necessary to validate the constitutive laws of biological tissues and the corresponding rupture criteria. When numerical aspects of the codes are validated and robust models are available, an interdisciplinary approach with engineers and physicians must therefore be set up to address the relevance of the results and make further progress.

APPENDIX A

MANUAL

This appendix provides a brief and pragmatic guide to set up the PFEM3D parameters in the framework of FSPC, the environment for flow-structure interaction problems. While it aligns with the May 2024 version, please be aware that the codes and the corresponding parameters may be subject to change. This guide is also not exhaustive.

PFEM3D requires a `.msh` as input file with the geometry and the initial set of fluid nodes. This file can be generated using Gmsh [62].

The input parameters of PFEM3D, the initial conditions, and the boundary conditions must be provided in a .lua file that can be structured as follows.

PFEM3D **Problem parameters.**

- *Problem.verboseOutput* = `true / false`

  Controls the output of the solver. Can be used to get detailed information about the operations carried out by the solver (iterations, remeshing, residues, ...).

- *Problem.autoRemeshing* = `false`

  Controls whether remeshing is performed by PFEM3D. Must be set to false for FSI problems since remeshing is controlled by FSPC and not by PFEM3D.

- *Problem.simulationTime* = `value`[1]

  Duration of the simulation.

- *Problem.id* = `IncompNewtonNoT / Boussinesq / IncompNewtonT / Conduction / Bingham / Casson / WCompNewtonNoT / WCBoussinesq / WCConduction`

  Selection of the fluid model: incompressible Newtonian fluid, incompressible Newtonian fluid with thermal effects under Boussinesq assumption, incompressible Newtonian fluid with thermal effects, heat equation only (no movement equation), incompressible Bingham fluid, incompressible Casson fluid, weakly compressible Newtonian fluid, weakly compressible Newtonian fluid with thermal effects under Boussinesq assumption, and weakly compressible with heat equation only.

[1] With FSPC, any value can be used here without affecting the simulation. This parameter is controlled by FSPC through the `main.py` file. A common practice is to set this parameter to `math.huge`.

- *Problem.axiSymmetric* = `true / false`

  Defines a 2D axisymmetric problem if set to `true`.

Mesh parameters.

- *Problem.Mesh.remeshAlgo* = `CGAL / CGAL_Edge / GMSH / GMSH_Edge / CGALConstrainedChew`

  Sets the algorithm used for remeshing. `GMSH_Edge` and `CGALConstrainedChew` are slower.

- *Problem.Mesh.boundingBox* = $\{x_{min}, y_{min}, x_{max}, y_{max}\}$

  Defines the bounding box containing the region in which the flow is modeled. PFEM nodes outside the bounding box are deleted at run time. In 3D, a third coordinate must be added.

- *Problem.Mesh.exclusionZones* = $\{x_{min}, y_{min}, x_{max}, y_{max}\}$

  Defines one or more exclusion zones. PFEM nodes inside the boxes are deleted at run time. In 3D, a third coordinate must be added.

- *Problem.Mesh.alpha* = `value`

  α parameter of the α-shape algorithm. Generally chosen in the range from 1.0 to 1.3. A small value of α will tend to separate weakly connected parts while a large value can artificially link subdomains that should be treated as separate.

- *Problem.Mesh.omega* = `value`

  ω parameter controlling the introduction of new nodes where elements become too large. Generally chosen in the range 0.7-0.9. Decreasing ω will tend to introduce more new nodes where the mesh size becomes large.

- *Problem.Mesh.gamma* = `value`

  γ parameter controlling the suppression of nodes where nodes get too close to each other. Should not be greater than 0.5. Increasing γ will tend to delete more nodes.

- *Problem.Mesh.gammaFS* = `value`

  Same as γ but for deleting nodes on free surfaces. A smaller value than γ is expected to keep more nodes on free surfaces. Parameter is not relevant if the flow has no free surface.

- *Problem.Mesh.addOnFS* = `true / false`

  Allows nodes to be added on a free surface. Tends to create mass conservation issues.

- *Problem.Mesh.hchar* = `value`

  Characteristic size of the mesh. Should be similar to the characteristic size of the initial mesh. If `hchar` is too large, many nodes will be deleted at the first iteration and the initial node density will be lost.

- *Problem.Mesh.Problem.Mesh.localHcharGroups* = list of physical groups (optional)

  List of physical groups used to control local variations of the characteristic size of the `hchar` parameter when a non-uniform mesh is used. When used, a `computeHcharFromDistance` function must be provided to define the rules for local adjustment of `hchar`.

- *function Problem.Mesh.computeHcharFromDistance(x,y,z,t,dist)*

  User-defined function used for the local adjustment of `hchar` and the generation of non-uniform mesh. This function should return the value `hchar` as a function of the nominal value and the distance `dist` to the physical groups listed in the `localHcharGroups`.

- *Problem.Mesh.minHeightFactor* = `value`

  Minimum size of elements deleted between solid parts come close to each other. Avoids creation of (near) flat triangles by Delaunay triangulation.

- *Problem.Mesh.keepFluidElements* = `true / false`

  Prevents/allows deleting elements in the core of the fluid domain.

- *Problem.Mesh.deleteFlyingNodes* = `true / false`

  Prevents/allows deleting "flying nodes", *i.e.,* nodes ejected from the fluid through the free surface that are not connected to any element.

- *Problem.Mesh.deleteBoundElements* = `true / false`

  Prevents/allows deleting elements with all their nodes on a boundary. Should be set to `true` only for incompressible flows, to prevent elements with all nodes with constrained movements to block the structure.

Extractors.

- *Problem.Extractors[i].kind* = `GMSH / Global / Point / MinMax`

  Defines extractor number `i` to write intermediate results on disk. Possible choices are `GMSH` to save the whole field, `Point` for the value of a field at a set of points, `Global` for global information, and `MinMax` to store the minimum/maximum value over the whole domain.

- *Problem.Extractors[i].whatToWrite* = `p / u / v / w / velocity / magV / mass / volume / ke`

  Defines the field or set of fields to be extracted by extractor `i`, *i.e.,* pressure, one or more velocity components, velocity vector, magnitude of the velocity, total mass, total volume, total kinetic energy (total parameters to be used with `Global` extractor only).

- *Problem.Extractors[i].timeBetweenWriting* = `value`[1]

  Time between writing of intermediate results.

- *Problem.Extractors[i].outputFile* = `name`

  Name of file on disk (`.msh` or `.txt` file according to the type of extractor to save results).

- *Problem.Extractors[i].writeAs* = `NodesElements`

  Sets `GMSH` type extractors to store results as nodal values.

- *Problem.Extractors[i].minMax* = `min / max`

  For `MinMax` type extractor, indicates whether to return maximum or minimum of the selected field.

- *Problem.Extractors[i].points* = `{x, y}`

  For `Point` type extractor, lists the coordinates of the points at which the value of the field is extracted.

Material parameters.

- Incompressible Newtonian fluid: `mu` (dynamic viscosity), `rho` (density), `gamma` (surface tension).
- Incompressible Casson fluid: `mu` (dynamic viscosity), `rho` (density), `gamma` (surface tension), `tau0` (yield stress), `mReg` (coefficient of regularization of the constitutive law).
- Incompressible Bingham fluid: `mu` (dynamic viscosity), `rho` (density), `gamma` (surface tension), `tau0` (yield stress), `mReg` (coefficient of regularization of the constitutive law).
- Weakly compressible Newtonian fluid: `mu` (dynamic viscosity), `rhoStar` (density), `gamma` (surface tension), `K0` and `K0p` (constants of the Tait-Murnaghan equation).

Solver parameters.

- *Problem.id* = `PSPG / FracStep`

  Selects solver for incompressible fluid: `Pressure Stabilizing Petrov Galerkin` is a monolithic solver (it has a unique matrix for velocity and pressure). `Fractional step` considers two different matrices (one for pressure and one for velocity) and it adapts one with respect to the other. The second is quicker but lacks the stability of `PSPG`.

- *Problem.Solver.adaptDT* = `true / false`

  Allows/prevents an adaptive time step. Should always be set to `true`, except for testing.

- *Problem.Solver.maxDT* = `value`[1]
  Problem.Solver.initialDT = `value`[1]

  Maximum and initial time steps of integration.

- *Problem.Solver.coeffDTDecrease* = `value`
  Problem.Solver.coeffDTIncrease = `value`

  Coefficients by which the time step is decreased (resp. increased) after an unsuccessful (resp. successful) iteration. Recommended values are 2 and 1, respectively.

Momentum and continuity equations[2].

- *Problem.Solver.MomContEq.nlAlgo* = `Picard / NR / quasiNR / quasiNRAprox`

  Selects the iterative algorithm for solving the nonlinear system of momentum and continuity equations. `NR` (Newton-Raphson) is more robust but more demanding than `Picard`.

- *Problem.Solver.MomContEq.residual* = `Ax_f / U_P`

  Selects the type of residual for convergence. `Ax_f` is based on the convergence of the force while `U_P` is based on the convergence of the velocity. `Ax_f` is not available for `FracStep` solver.

- *Problem.Solver.MomContEq.sparseSolverLib* = `MKL / MKL_Pardiso / Eigen / Pastix / Amgcl / CUDA_GPU`

  Selects the sparse solver to be used.

[2]In the context of this thesis, only the momentum and continuity equations were solved (therefore the manual does not contain information about the heat equation).

- *Problem.Solver.MomContEq.tolerance* = `value`

  Algorithm relative tolerance used by some sparse solvers. Should be set between 1e-12 and 1e-6.

- *Problem.Solver.MomContEq.maxIter* = `value`

  Maximum number of iterations allowed at each time step before the time step is considered unsuccessful.

- *Problem.Solver.MomContEq.minRes* = `value`

  Minimum residual of momentum and continuity equations. Values between 1e-8 and 1e-6 are typically recommended.

- *Problem.Solver.MomContEq.BC['FSInterfaceVExt']* = `true / false`

  Tells PFEM3D to use Metafor displacement data at the FSI interface and not to search for user-defined boundary functions. Must be set to `true` for coupled simulations.

Boundary (BC) and initial (IC) conditions.

- *function Problem.IC.initStates(x,y,z)*

  User-defined function returning the velocity and pressure fields at the initial time.

- *function Problem.Solver.MomContEq.BC.NameVEuler(x,y,z,t)* (optional)

  User-defined function returning the velocity field to be prescribed on the physical group `Name`. An Eulerian velocity is imposed, *i.e.,* the velocity is prescribed at the boundary, and not as a moving node.

- *Problem.Solver.MomContEq.BC['NameFreeSlipEuler']* = `true` (optional)
  Problem.Solver.MomContEq.oneEpsFreeSlip = `value`

  Defines physical group as free-slip boundary and sets penalty for normal velocity component.

- *function Problem.Solver.MomContEq.BC.NameP(x,y,z)* (optional)

  User-defined function returning the pressure field to be prescribed on physical group `Name`.

FSPC Main file.

A series of parameters related to the FSPC coupling between PFEM3D and Metafor are defined in the `main.py` file as follows.

- *solver = FSPC.init_solver(path_F, path_S)*

  Sets the `inputF.lua` and `inputS.py` files with the parameters of the simulation related to PFEM3D and Metafor and defines the `solver` variable.

- *algorithm = FSPC.algorithm.*`XXX`*(*`val`*)*
  FSPC.set_algorithm(algorithm)

  Defines `XXX` as the iterative algorithm to solve the coupling problem. Possible choices of `XXX` are the Block Gauss Seidel `BGS`, Quasi-Newton with inverse least-square `ILS`, and Multi-Vector Jacobian `MVJ`. The latter is deemed to be more efficient but cannot be used when the number of nodes on the solid side of the interface changes with time (*e.g.,* rupture).

  The maximum number of iterations is set to `val` (recommended value = 25).

- *interpolator = FSPC.interpolator.*`YYY`*(param)*
  FSPC.set_interpolator(interpolator)

  Sets the interpolation method between the fluid and solid domains along the FSI interface. Possible choices of `YYY` are

  - `FSPC.interpolator.RBF(fun)`: Radial Basis Function with interpolating function `fun` (to be defined by the user);
  - `FSPC.interpolator.LEP`: Linear Element Projection method (using the shape functions to interpolate nodal data between the fluid and solid domains).

- *step = FSPC.general.TimeStep*(`t1, t2`)
  FSPC.set_time_step(step)

  Defines the initial integration time step `t1` and the time between writing of intermediate results `t2`. The time step should be small enough to avoid remeshing problems.

- *residual = FSPC.general.Residual*(`val`)
  FSPC.set_mechanical_res(residual)

  Sets to `val` the mechanical residual controlling convergence of the iterations between the fluid and solid models.

- *algorithm.simulate*(`val`)

  Sets to `val` the total duration of the simulation.

APPENDIX B

WALL SHEAR STRESS

The wall shear stress is a parameter of great physiological importance. However, it is not directly accessible in the results of the coupled models. This appendix provides a description of how the computation of wall shear stress is implemented in this work, and a verification of the approach.

Implementation.

In coupled simulations, the stresses exerted by the fluid are applied to the solid which deforms under these loadings applied as a Neumann boundary condition. The movement of the solid is imposed on the fluid as a Dirichlet boundary condition. Stresses are therefore continuous between the fluid and the solid. The Wall Shear Stress (WSS) can be evaluated either in the solid domain (Metafor) or in the fluid domain (PFEM3D).

On the solid side, one has the advantage of having direct access to the Cauchy stress tensor (at least at the Gauss points). Surface tractions can be obtained by projecting the Cauchy stress tensor onto the normal. The tangential component of the surface tractions is the WSS. However, inaccuracies arise from the presence of a pressure component in the surface tractions, which can be several orders of magnitude higher than the tangential component. Small errors in the orientation of the normal leads therefore to large errors on the WSS when projecting the surface tractions.

The alternative is to calculate the WSS on the fluid side, taking advantage of the natural separation between viscous forces ($\boldsymbol{\tau}$) and pressure (p), *i.e.,*

$$\boldsymbol{\sigma} = -p\mathbf{I} + \boldsymbol{\tau} \tag{B.1}$$

However, since viscous stresses are not directly accessible through appropriate extractors of the PFEM3D code, the components of $\boldsymbol{\tau}$ must be recalculated from the velocity field $\mathbf{v}$ during post-processing of the results using

$$\boldsymbol{\tau} = 2\mu\mathbf{D} \tag{B.2}$$

where the strain rate tensor is given by

$$D_{ij} = \frac{1}{2}\left(\frac{\partial u_i}{\partial x_j} + \frac{\partial u_j}{\partial x_i}\right) \tag{B.3}$$

This particular procedure for calculating the wall shear stress is not affected by the large values of p.

The same procedure can also be used to compute the shear rate

$$\dot{\gamma} = \sqrt{2\mathbf{D} : \mathbf{D}} \tag{B.4}$$

which is an important parameter affecting the rheology of whole blood. It is also required to evaluate the viscosity of the fluid when a Casson model is used.

In practice, the computation of the WSS (and the shear rate) along the boundary of the fluid domain from a 2D gmsh file generated by PFEM3D is carried out using the following procedure implemented in a stand-alone MATLAB code.

- The structure of `.msh` files[1] is exploited to read and reconstruct the list of fluid nodes with their coordinates and the list of nodal values of the velocity. In addition, the list of 1D boundary elements and the list of 2D fluid elements (triangles) are also extracted from the `.msh` file together with the tags of their nodes.

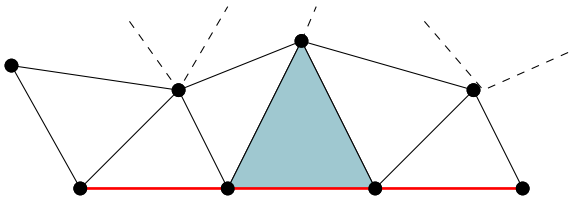

FIGURE B.1 – Schematic representation of the nodes (●), 1D elements (—), and 2D elements of the PFEM mesh (■).

- An ordered list of consecutive 1D elements that connect to each other is built, which defines the boundary contour of the fluid domain. The unit normal and tangent vectors, along with the curvilinear abscissa, are computed from the coordinates of the successive nodes along the contour.
- The tag of the single 2D element to which each 1D element belongs is found by comparing the list of nodes defining the 1D and 2D elements. The 2D element corresponding to a given 1D element is the one that is built on the two nodes of the 1D element.
- Using the nodal values at the three vertices of each triangular 2D element, a linear representation of the velocity field coherent with the interpolation used in PFEM3D is used to compute the components of the strain rate tensor $\mathbf{D}$, the shear rate, and the components of the tensor of viscous stresses $\boldsymbol{\tau}$.
- For each 1D element of the boundary curve, surface tractions are computed by projecting $\boldsymbol{\tau}$ onto the unit normal. The wall shear stress is computed by a new projection onto the tangent vector. The results are assigned to the barycenter of the 1D boundary element.

Verification.

To verify the approach, the code is applied to a simple case with a known analytical solution: a 2D pipe or blood vessel of radius R, length L, and at an angle ϕ with respect to the axes, with a fully developed Poiseuille profile described by

$$u_\xi = 0 \tag{B.5}$$

$$u_\eta = V_{max}\left[1 - \left(\frac{\xi}{R}\right)^2\right] \tag{B.6}$$

in the coordinate system attached to the pipe (Figure B.2). The corresponding wall shear stress is therefore given by

$$\tau = \mu\frac{\partial u_\eta}{\partial \xi} = \mu V_{max}\left[1 - \frac{2\xi}{R^2}\right] \tag{B.7}$$

[1] See `https://gmsh.info/doc/texinfo/gmsh.html#Gmsh-file-formats`.

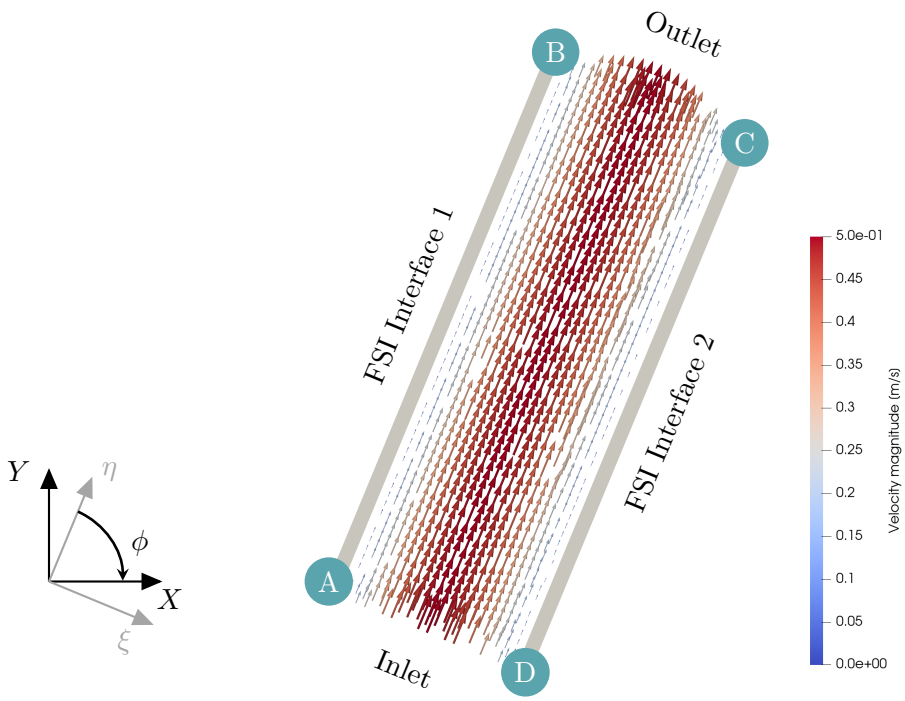

FIGURE B.2 – Velocity profile in a vessel of radius R, length L, and inclination ϕ.

The parabolic velocity profile obtained using PFEM3D with a discretization of 20 points across the pipe is shown in Figure B.2.

The `.msh` file with the results of PFEM3D describing the Poiseuille flow is used as an input to the procedure described above. Figure B.3 shows the wall shear stress computed in this way and the comparison with the analytical values. The reconstructed values nicely compare with the theoretical ones. The difference is less than 4% and is not associated with the inaccuracy of the method but is related to the limited spatial resolution to approximate the Poiseuille profile.

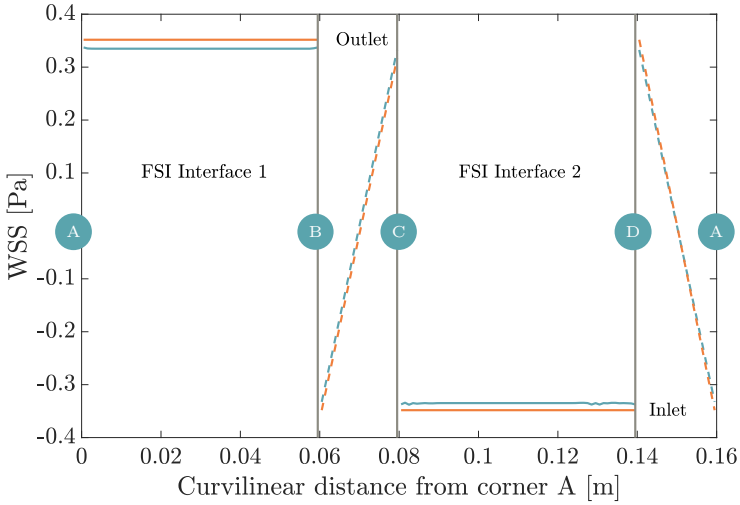

FIGURE B.3 – Wall shear stress along the different boundaries (numerical (——) and analytical (——) results). The curvilinear distance starts at corner A. (See Figure B.2 for the location of the nodes A, B, C, and D.)

Note that the shear stresses on the solid boundaries and in the inlet/outlet sections do not have the same meaning. In the inlet and outlet sections, the shear stress is along $\mathbf{e}_\xi$ while shear stresses on the two interfaces refer to stresses along $\mathbf{e}_\eta$.

The procedure is further verified by comparing the shear rate $\dot{\gamma}$ with an independent estimate computed using the `Paraview` post-processing software. A special filter of `Paraview` allows indeed the direct computation of the velocity gradient tensor and the strain rate tensor. Figure B.4 shows a zoom of the shear rate distribution in the vicinity of one of the solid boundaries. This figure illustrates the fact that the linear interpolation of the velocity field results in a constant shear rate (and shear stress) at each triangular element. The maximum value of 97.2 s^{-1} reported along the wall corresponds exactly to the 0.34 Pa shear stress computed from the approximate Poiseuille profile with the procedure described in this section, since in the simple setup considered here, the wall shear stress is equal to the product of the shear rate and the viscosity $\mu = 0.0035$ Pa $\cdot$ s of the fluid.

This completes the verification of the procedure and of the corresponding code introduced to extract the wall shear stress from the model results.

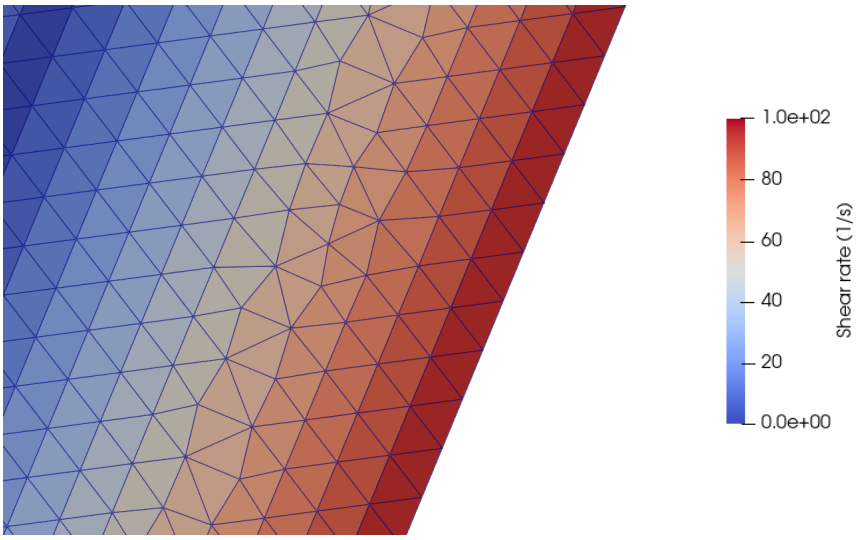

FIGURE B.4 – Zoom of the shear rate computed with `Paraview`.

BIBLIOGRAPHY

[1] S. Abbas, M. Nasif and R. Al-Waked, *State-of-the-art numerical fluid–structure interaction methods for aortic and mitral heart valves simulations: A review*, Simulation, 98 (2021), p. 003754972110235. doi:10.1177/00375497211023573.

[2] A. Amindari, L. Saltik, K. Kirkkopru, M. Yacoub and H. C. Yalcin, *Assessment of calcified aortic valve leaflet deformations and blood flow dynamics using fluid-structure interaction modeling*, Informatics in Medicine Unlocked, 9 (2017), pp. 191–199. doi:10.1016/j.imu.2017.09.001.

[3] M. Ariane, M. H. Allouche, M. Bussone, F. Giacosa, F. Bernard, M. Barigou and A. Alexiadis, *Discrete multi-physics: A mesh-free model of blood flow in flexible biological valve including solid aggregate formation*, PLoS ONE, 12 (2017), p. e0174795. doi:10.1371/journal.pone.0174795.

[4] A. Arslan and H. Salman, *Effect of Intraluminal Thrombus Burden on the Risk of Abdominal Aortic Aneurysm Rupture*, Journal of Cardiovascular Development and Disease, 10 (2023), p. 233. doi:10.3390/jcdd10060233.

[5] A. Athani, N. N. N. Ghazali, I. A. Badruddin, S. Kamangar, A. E. Anqi and A. Algahtani, *Investigation of two-way fluid-structure interaction of blood flow in a patient-specific left coronary artery*, Bio-Medical Materials and Engineering, 33 (2022), pp. 13–30. doi:10.3233/BME-201171.

[6] K. I. Aycock, R. L. Campbell, F. C. Lynch, K. B. Manning and B. A. Craven, *The Importance of Hemorheology and Patient Anatomy on the Hemodynamics in the Inferior Vena Cava*, Annals of Biomedical Engineering, 44 (2016), pp. 3568–3582. doi:10.1007/s10439-016-1663-x.

[7] M. Bagheri, M. Mohammadi and M. Riazi, *A review of smoothed particle hydrodynamics*, Computational Particle Mechanics, (2023). doi:10.1007/s40571-023-00679-7.

[8] D. Balzani, A. Heinlein, A. Klawonn, O. Rheinbach and J. Schröder, *Comparison of arterial wall models in fluid–structure interaction simulations*, Computational Mechanics, 72 (2023), pp. 949–965. doi:10.1007/s00466-023-02321-y.

[9] G. O. Barnett, A. J. Mallos and A. Shapiro, *Relationship of aortic pressure and diameter in the dog*, Journal of Applied Physiology, 16 (1961), pp. 545–548. Publisher: American Physiological Society. doi:10.1152/jappl.1961.16.3.545.

[10] A. M. Bavo, G. Rocatello, F. Iannaccone, J. Degroote, J. Vierendeels and P. Segers, *Fluid-Structure Interaction Simulation of Prosthetic Aortic Valves: Comparison between Immersed Boundary and Arbitrary Lagrangian-Eulerian Techniques for the Mesh Representation*, PloS One, 11 (2016), p. e0154517. doi:10.1371/journal.pone.0154517.

[11] B. T. Baxter, G. S. McGee, V. P. Shively, I. A. Drummond, S. N. Dixit, M. Yamauchi and W. H. Pearce, *Elastin content, cross-links, and mRNA in normal and aneurysmal human aorta*, Journal of Vascular Surgery, 16 (1992), pp. 192–200.

[12] T. Belytschko, Y. Guo, W. Kam Liu and S. Ping Xiao, *A unified stability analysis of meshless particle methods*, International Journal for Numerical Methods in Engineering, 48 (2000), pp. 1359–1400. doi:10.1002/1097-0207(20000730)48:9<1359::AID-NME829>3.0.CO;2-U.

[13] N. Bessonov, A. Sequeira, S. Simakov, Y. Vassilevskii and V. Volpert, *Methods of Blood Flow Modelling*, Mathematical Modelling of Natural Phenomena, 11 (2016), pp. 1–25. Number: 1 Publisher: EDP Sciences. doi:10.1051/mmnp/201611101.

[14] A. Bilotta, *Solid Mechanics - A first course on solid mechanics*, 2024, https://antoniobilotta-structuralengineer.github.io/MyWebSite/SMbook_en/solid_mechanics_book_en.html (Accessed: 2024-05-14).

[15] BioNinja, *Heart Structure*, https://old-ib.bioninja.com.au/standard-level/topic-6-human-physiology/62-the-blood-system/heart-structure.html (Accessed: 2024-02-19).

[16] J. Bonet and R. D. Wood, *Nonlinear Continuum Mechanics for Finite Element Analysis*, Cambridge University Press, Cambridge, 2 ed., 2008. doi:10.1017/CBO9780511755446.

[17] K. Bäumler, V. Vedula, A. M. Sailer, J. Seo, P. Chiu, G. Mistelbauer, F. P. Chan, M. P. Fischbein, A. L. Marsden and D. Fleischmann, *Fluid-structure interaction simulations of patient-specific aortic dissection*, Biomechanics and Modeling in Mechanobiology, 19 (2020), pp. 1607–1628. doi:10.1007/s10237-020-01294-8.

[18] A. Caballero, W. Mao, L. Liang, J. Oshinski, C. Primiano, R. McKay, S. Kodali and W. Sun, *Modeling Left Ventricular Blood Flow Using Smoothed Particle Hydrodynamics*, Cardiovascular Engineering and Technology, 8 (2017), pp. 465–479. doi:10.1007/s13239-017-0324-z.

[19] L. Cai, Y. Hao, P. Ma, G. Zhu, X. Luo and H. Gao, *Fluid-structure interaction simulation of calcified aortic valve stenosis*, Mathematical biosciences and engineering: MBE, 19 (2022), pp. 13172–13192. doi:10.3934/mbe.2022616.

[20] D. B. Camasão and D. Mantovani, *The mechanical characterization of blood vessels and their substitutes in the continuous quest for physiological-relevant performances. A critical review*, Materials Today Bio, 10 (2021), p. 100106. doi:10.1016/j.mtbio.2021.100106.

[21] L. Campo-Deaño, M. S. N. Oliveira and F. T. Pinho, *A Review of Computational Hemodynamics in Middle Cerebral Aneurysms and Rheological Models for Blood Flow*, Applied Mechanics Reviews, 67 (2015), p. 030801. doi:10.1115/1.4028946.

[22] R. Campobasso, F. Condemi, M. Viallon, P. Croisille, S. Campisi and S. Avril, *Evaluation of Peak Wall Stress in an Ascending Thoracic Aortic Aneurysm Using FSI Simulations: Effects of Aortic Stiffness and Peripheral Resistance*, Cardiovascular Engineering and Technology, 9 (2018), pp. 707–722. doi:10.1007/s13239-018-00385-z.

[23] T. Canchi, A. Saxena, E. Ng, E. C. Pwee and S. Narayanan, *Application of Fluid–Structure Interaction Methods to Estimate the Mechanics of Rupture in Asian Abdominal Aortic Aneurysms*, BioNanoScience, 8 (2018), pp. 1035–1044. doi:10.1007/s12668-018-0554-z.

[24] K. Cao, S. K. Atkins, A. McNally, J. Liu and P. Sucosky, *Simulations of morphotype-dependent hemodynamics in non-dilated bicuspid aortic valve aortas*, Journal of Biomechanics, 50 (2017), pp. 63–70. doi:10.1016/j.jbiomech.2016.11.024.

[25] K. Cao and P. Sucosky, *Aortic valve leaflet wall shear stress characterization revisited: impact of coronary flow*, Computer Methods in Biomechanics and Biomedical Engineering, (2017). Publisher: Taylor & Francis.

[26] E. Cecchi, C. Giglioli, S. Valente, C. Lazzeri, G. F. Gensini, R. Abbate and L. Mannini, *Role of hemodynamic shear stress in cardiovascular disease*, Atherosclerosis, 214 (2011), pp. 249–256. doi:10.1016/j.atherosclerosis.2010.09.008.

[27] M. L. Cerquaglia, *Development of a fully-partitioned PFEM-FEM approach for fluid-structure interaction problems characterized by free surfaces, large solid deformations, and strong added-mass effects*, (2019). Publisher: ULiège - Université de Liège.

[28] A. Cetin and M. Sahin, *A monolithic fluid-structure interaction framework applied to red blood cells*, International Journal for Numerical Methods in Biomedical Engineering, 35 (2019), p. e3171. doi:10.1002/cnm.3171.

[29] E. I. Charitos and H.-H. Sievers, *Anatomy of the aortic root: implications for valve-sparing surgery*, Annals of Cardiothoracic Surgery, 2 (2013), pp. 53–56. doi:10.3978/j.issn.2225-319X.2012.11.18.

[30] Y. S. Chatzizisis, A. U. Coskun, M. Jonas, E. R. Edelman, C. L. Feldman and P. H. Stone, *Role of endothelial shear stress in the natural history of coronary atherosclerosis and vascular remodeling: molecular, cellular, and vascular behavior*, Journal of the American College of Cardiology, 49 (2007), pp. 2379–2393. doi:10.1016/j.jacc.2007.02.059.

[31] C. P. Cheng, R. J. Herfkens and C. A. Taylor, *Inferior vena caval hemodynamics quantified in vivo at rest and during cycling exercise using magnetic resonance imaging*, American Journal of Physiology. Heart and Circulatory Physiology, 284 (2003), pp. H1161–1167. doi:10.1152/ajpheart.00641.2002.

[32] H.-L. Chien, B.-W. Huang and J.-H. Kuang, *The Ogden Model for Coronary Artery Mechanical Behaviors*, Life Science Journal, 8 (2011), pp. 430–437.

[33] S. Chien, S. Usami, H. M. Taylor, J. L. Lundberg and M. I. Gregersen, *Effects of hematocrit and plasma proteins on human blood rheology at low shear rates*, Journal of Applied Physiology, 21 (1966), pp. 81–87. doi:10.1152/jappl.1966.21.1.81.

[34] M. Cremonesi, A. Franci, S. Idelsohn and E. Oñate, *A State of the Art Review of the Particle Finite Element Method (PFEM)*, Archives of Computational Methods in Engineering, 27 (2020), pp. 1709–1735. doi:10.1007/s11831-020-09468-4.

[35] M. Cremonesi, A. Frangi and U. Perego, *A Lagrangian finite element approach for the simulation of water-waves induced by landslides*, Computers & Structures, 89 (2011), pp. 1086–1093. doi:10.1016/j.compstruc.2010.12.005.

[36] M. R. Crompton, *Mechanism of Growth and Rupture in Cerebral Berry Aneurysms*, British Medical Journal, 1 (1966), pp. 1138–1142.

[37] Y. Dabiri, J. Ronsky, I. Ali, A. Basha, A. Bhanji and K. Narine, *Effects of Leaflet Design on Transvalvular Gradients of Bioprosthetic Heart Valves*, Cardiovascular Engineering and Technology, 7 (2016), pp. 363–373. doi:10.1007/s13239-016-0279-5.

[38] R. C. Darling, C. R. Messina, D. C. Brewster and L. W. Ottinger, *Autopsy study of unoperated abdominal aortic aneurysms. The case for early resection*, Circulation, 56 (1977), pp. II161–164.

[39] J. De Hart, G. W. Peters, P. J. Schreurs and F. P. Baaijens, *A two-dimensional fluid-structure interaction model of the aortic valve [correction of value]*, Journal of Biomechanics, 33 (2000), pp. 1079–1088. doi:10.1016/s0021-9290(00)00068-3.

[40] R. De Paulis and A. Salica, *Surgical anatomy of the aortic valve and root-implications for valve repair*, Annals of Cardiothoracic Surgery, 8 (2019), pp. 313–321. doi:10.21037/acs.2019.04.16.

[41] E. S. Di Martino, G. Guadagni, A. Fumero, G. Ballerini, R. Spirito, P. Biglioli and A. Redaelli, *Fluid–structure interaction within realistic three-dimensional models of the aneurysmatic aorta as a guidance to assess the risk of rupture of the aneurysm*, Medical Engineering & Physics, 23 (2001), pp. 647–655. doi:10.1016/S1350-4533(01)00093-5.

[42] M. Domanin, D. Bissacco, D. Le Van and C. Vergara, *Computational fluid dynamic comparison between patch-based and primary closure techniques after carotid endarterectomy*, Journal of Vascular Surgery, 67 (2018), pp. 887–897. doi:10.1016/j.jvs.2017.08.094.

[43] J. Donéa and A. Huerta, *Finite element methods for flow problems*, Wiley, Chichester ; Hoboken, NJ, 2003. OCLC: ocm48025024.

[44] J. Donéa, A. Huerta, J.-P. Ponthot and A. Rodríguez-Ferran, *Arbitrary Lagrangian–Eulerian Methods*, in Encyclopedia of Computational Mechanics Second Edition, John Wiley & Sons, Ltd, 2017, pp. 1–23.

[45] B. J. Doyle, T. J. Corbett, A. Callanan, M. T. Walsh, D. A. Vorp and T. M. McGloughlin, *An Experimental and Numerical Comparison of the Rupture Locations of an Abdominal Aortic Aneurysm*, Journal of Endovascular Therapy, 16 (2009), pp. 322–335. doi:10.1583/09-2697.1.

[46] C. J. Drewe, L. P. Parker, L. J. Kelsey, P. E. Norman, J. T. Powell and B. J. Doyle, *Haemodynamics and stresses in abdominal aortic aneurysms: A fluid-structure interaction study into the effect of proximal neck and iliac bifurcation angle*, Journal of Biomechanics, 60 (2017), pp. 150–156. doi:10.1016/j.jbiomech.2017.06.029.

[47] H. Edelsbrunner and E. P. Mücke, *Three-dimensional alpha shapes*, ACM Transactions on Graphics, 13 (1994), pp. 43–72. doi:10.1145/174462.156635.

[48] D. R. Einstein, F. Del Pin, X. Jiao, A. P. Kuprat, J. P. Carson, K. S. Kunzelman, R. P. Cochran, J. M. Guccione and M. B. Ratcliffe, *Fluid-Structure Interactions of the Mitral Valve and Left Heart: Comprehensive Strategies, Past, Present and Future*, International Journal for Numerical Methods in Engineering, 26 (2010), pp. 348–380. doi:10.1002/cnm.1280.

[49] E. W. Errill, *Rheology of blood*, Physiological Reviews, 49 (1969), pp. 863–888. Publisher: American Physiological Society. doi:10.1152/physrev.1969.49.4.863.

[50] R. Falla, B.-J. Bobach, R. Boman, J.-P. Ponthot and V. E. Terrapon, *Mesh adaption for two-dimensional bounded and free-surface flows with the particle finite element method*, Computational Particle Mechanics, 10 (2023), pp. 1049–1076. doi:10.1007/s40571-022-00541-2.

[51] M. Fedele, E. Faggiano, L. Dedè and A. Quarteroni, *A patient-specific aortic valve model based on moving resistive immersed implicit surfaces*, Biomechanics and Modeling in Mechanobiology, 16 (2017), pp. 1779–1803. doi:10.1007/s10237-017-0919-1.

[52] M. F. Fillinger, S. P. Marra, M. L. Raghavan and F. E. Kennedy, *Prediction of rupture risk in abdominal aortic aneurysm during observation: wall stress versus diameter*, Journal of Vascular Surgery, 37 (2003), pp. 724–732. doi:10.1067/mva.2003.213.

[53] M. F. Fillinger, M. L. Raghavan, S. P. Marra, J. L. Cronenwett and F. E. Kennedy, *In vivo analysis of mechanical wall stress and abdominal aortic aneurysm rupture risk*, Journal of Vascular Surgery, 36 (2002), pp. 589–597. doi:10.1067/mva.2002.125478.

[54] E. A. Finol and C. H. Amon, *Flow-induced wall shear stress in abdominal aortic aneurysms: Part I–steady flow hemodynamics*, Computer Methods in Biomechanics and Biomedical Engineering, 5 (2002), pp. 309–318. doi:10.1080/1025584021000009742.

[55] L. Formaggia, J. F. Gerbeau, F. Nobile and A. Quarteroni, *On the coupling of 3D and 1D Navier–Stokes equations for flow problems in compliant vessels*, Computer Methods in Applied Mechanics and Engineering, 191 (2001), pp. 561–582. doi:10.1016/S0045-7825(01)00302-4.

[56] A. Franci, M. Cremonesi, U. Perego and E. Oñate, *A Lagrangian nodal integration method for free-surface fluid flows*, Computer Methods in Applied Mechanics and Engineering, 361 (2020), p. 112816. doi:10.1016/j.cma.2019.112816.

[57] J. Friesen, J. Bergner, M. I. A. Khan, S. Triess, A. Zoll, P. F. Pelz and F. Adili, *Comparison of existing aneurysm models and their path forward*, Computer Methods and Programs in Biomedicine Update, 1 (2021), p. 100019. doi:10.1016/j.cmpbup.2021.100019.

[58] Y.-C. Fung, *Biomechanics*, Springer, New York, NY, 1993. doi:10.1007/978-1-4757-2257-4.

[59] Y.-C. Fung, K. Fronek and P. Patitucci, *Pseudoelasticity of arteries and the choice of its mathematical expression*, The American Journal of Physiology, 237 (1979), pp. H620–631. doi:10.1152/ajpheart.1979.237.5.H620.

[60] S. Février, *Master's thesis : Development of a compressible flow solver for PFEM fluid simulations*, 2020. http://hdl.handle.net/2268.2/9010.

[61] H. Gao, L. Feng, N. Qi, C. Berry, B. E. Griffith and X. Luo, *A coupled mitral valve—left ventricle model with fluid–structure interaction*, Medical Engineering & Physics, 47 (2017), pp. 128–136. doi:10.1016/j.medengphy.2017.06.042.

[62] C. Geuzaine and J.-F. Remacle, *Gmsh: A 3-D finite element mesh generator with built-in pre- and post-processing facilities*, International Journal for Numerical Methods in Engineering, 79 (2009), pp. 1309–1331. doi:10.1002/nme.2579.

[63] S. H. Gharaie, B. Mosadegh and Y. Morsi, *In Vitro Validation of a Numerical Simulation of Leaflet Kinematics in a Polymeric Aortic Valve Under Physiological Conditions*,

Cardiovascular Engineering and Technology, 9 (2018), pp. 42–52. doi:10.1007/s13239-018-0340-7.

[64] M. J. Ghasemi Pour, K. Hassani, M. Khayat and S. Etemadi Haghighi, *Modeling of aortic valve stenosis using fluid-structure interaction method*, Perfusion, 37 (2022), pp. 367–376. doi:10.1177/0267659121998549.

[65] J. B. Grotberg, *Biofluid Mechanics | Biomedical engineering*, Cambridge Text in Biomedical Engineering, Cambridge University Press, 2021.

[66] A. Grytsan, P. N. Watton and G. A. Holzapfel, *A thick-walled fluid-solid-growth model of abdominal aortic aneurysm evolution: application to a patient-specific geometry*, Journal of Biomechanical Engineering, 137 (2015). doi:10.1115/1.4029279.

[67] D. Guan, F. Liang and P. A. Gremaud, *Comparison of the Windkessel model and structured-tree model applied to prescribe outflow boundary conditions for a one-dimensional arterial tree model*, Journal of Biomechanics, 49 (2016), pp. 1583–1592. doi:10.1016/j.jbiomech.2016.03.037.

[68] K. Hajirayat, S.-S. Gholampour, I. Sharifi and D. Bizari, *Biomechanical Simulation to Compare the Blood Hemodynamics and Cerebral Aneurysm Rupture Risk in Patients with Different Aneurysm Necks*, Journal of Applied Mechanics and Technical Physics, 58 (2017), pp. 968–974. doi:10.1134/S0021894417060025.

[69] R. Halevi, A. Hamdan, G. Marom, K. Lavon, S. Ben-Zekry, E. Raanani, D. Bluestein and R. Haj-Ali, *Fluid-structure interaction modeling of calcific aortic valve disease using patient-specific three-dimensional calcification scans*, Medical & Biological Engineering & Computing, 54 (2016), pp. 1683–1694. doi:10.1007/s11517-016-1458-0.

[70] S. J. Haller, A. F. Azarbal and S. Rugonyi, *Predictors of Abdominal Aortic Aneurysm Risks*, Bioengineering, 7 (2020), p. 79. doi:10.3390/bioengineering7030079.

[71] H. Handa, N. Hashimoto, I. Nagata and F. Hazama, *Saccular cerebral aneurysms in rats: a newly developed animal model of the disease.*, Stroke, (1983). doi:10.1161/01.STR.14.6.857.

[72] A. Hasan, E. M. Kolahdouz, A. Enquobahrie, T. G. Caranasos, J. P. Vavalle and B. E. Griffith, *Image-based immersed boundary model of the aortic root*, Medical Engineering & Physics, 47 (2017), pp. 72–84. doi:10.1016/j.medengphy.2017.05.007.

[73] A. Hasan, K. Ragaert, W. Swieszkowski, S. Selimović, A. Paul, G. Camci-Unal, M. R. K. Mofrad and A. Khademhosseini, *Biomechanical properties of native and tissue engineered heart valve constructs*, Journal of Biomechanics, 47 (2014), pp. 1949–1963. doi:10.1016/j.jbiomech.2013.09.023.

[74] H. Hatoum and L. P. Dasi, *Spatiotemporal complexity of the aortic sinus vortex as a function of leaflet calcification*, Annals of biomedical engineering, 47 (2019), pp. 1116–1128. doi:10.1007/s10439-019-02224-1.

[75] M. Hedayat and I. Borazjani, *Comparison of platelet activation through hinge vs bulk flow in bileaflet mechanical heart valves*, Journal of Biomechanics, 83 (2019), pp. 280–290. doi:10.1016/j.jbiomech.2018.12.003.

[76] J. H. G. Helthuis, S. Bhat, T. P. C. van Doormaal, R. K. Kumar and A. van der Zwan, *Proximal and Distal Occlusion of Complex Cerebral Aneurysms-Implications of Flow*

Modeling by Fluid-Structure Interaction Analysis, Operative Neurosurgery (Hagerstown, Md.), 15 (2018), pp. 217–230. doi:10.1093/ons/opx236.

[77] M. Hirschhorn, V. Tchantchaleishvili, R. Stevens, J. Rossano and A. Throckmorton, *Fluid-structure interaction modeling in cardiovascular medicine - A systematic review 2017-2019*, Medical Engineering & Physics, 78 (2020), pp. 1–13. doi:10.1016/j.medengphy.2020.01.008.

[78] G. A. Holzapfel, R. Eberlein, P. Wriggers and H. W. Weizsäcker, *Large strain analysis of soft biological membranes: Formulation and finite element analysis*, Computer Methods in Applied Mechanics and Engineering, 132 (1996), pp. 45–61. doi:10.1016/0045-7825(96)00999-1.

[79] G. A. Holzapfel, G. Sommer, C. T. Gasser and P. Regitnig, *Determination of layer-specific mechanical properties of human coronary arteries with nonatherosclerotic intimal thickening and related constitutive modeling*, American Journal of Physiology. Heart and Circulatory Physiology, 289 (2005), pp. H2048–2058. doi:10.1152/ajpheart.00934.2004.

[80] P. R. Hoskins, P. V. Lawford and B. J. Doyle, eds., *Cardiovascular Biomechanics*, Springer International Publishing, Cham, 2017. doi:10.1007/978-3-319-46407-7.

[81] M.-C. Hsu, D. Kamensky, Y. Bazilevs, M. S. Sacks and T. J. R. Hughes, *Fluid–structure interaction analysis of bioprosthetic heart valves: Significance of arterial wall deformation*, Computational mechanics, 54 (2014), pp. 1055–1071. doi:10.1007/s00466-014-1059-4.

[82] F. Q. Hu, *Development of PML absorbing boundary conditions for computational aeroacoustics: A progress review*, Computers & Fluids, 37 (2008), pp. 336–348. doi:10.1016/j.compfluid.2007.02.012.

[83] W.-X. Huang and F.-B. Tian, *Recent trends and progress in the immersed boundary method*, Proceedings of the Institution of Mechanical Engineers, Part C: Journal of Mechanical Engineering Science, 233 (2019), pp. 7617–7636. Publisher: IMECHE. doi:10.1177/0954406219842606.

[84] T. J. R. Hughes, L. P. Franca and M. Balestra, *A new finite element formulation for computational fluid dynamics: V. Circumventing the Babuška-Brezzi condition: a stable Petrov-Galerkin formulation of the stokes problem accommodating equal-order interpolations*, Computer Methods in Applied Mechanics and Engineering, 59 (1986), pp. 85–99. doi:10.1016/0045-7825(86)90025-3.

[85] J. D. Humphrey and G. A. Holzapfel, *Mechanics, mechanobiology, and modeling of human abdominal aorta and aneurysms*, Journal of Biomechanics, 45 (2012), pp. 805–814. doi:10.1016/j.jbiomech.2011.11.021.

[86] J. D. Humphrey and C. A. Taylor, *Intracranial and abdominal aortic aneurysms: similarities, differences, and need for a new class of computational models*, Annual Review of Biomedical Engineering, 10 (2008), pp. 221–246. doi:10.1146/annurev.bioeng.10.061807.160439.

[87] Hôpital Universitaire de Bruxelles, *Vers un plan national des maladies cardiovasculaires, l'une des premières causes de décès en Belgique*, 2023, https://www.hubruxelles.be/fr/vers-un-plan-national-des-maladies-cardiovasculaires-lune-des-premieres-causes-de-deces-en-0 (Accessed: 2024-02-24).

[88] S. R. Idelsohn, J. Marti, A. Limache and E. Oñate, *Unified Lagrangian formulation for elastic solids and incompressible fluids: Application to fluid–structure interaction problems via the PFEM*, Computer Methods in Applied Mechanics and Engineering, 197 (2008), pp. 1762–1776. doi:10.1016/j.cma.2007.06.004.

[89] S. R. Idelsohn and E. Oñate, *To mesh or not to mesh. That is the question...*, Computer Methods in Applied Mechanics and Engineering, 195 (2006), pp. 4681–4696. doi:10.1016/j.cma.2005.11.006.

[90] R. Jayendiran, B. Nour and A. Ruimi, *Fluid-structure interaction (FSI) analysis of stent-graft for aortic endovascular aneurysm repair (EVAR): Material and structural considerations*, Journal of the Mechanical Behavior of Biomedical Materials, 87 (2018), pp. 95–110. doi:10.1016/j.jmbbm.2018.07.020.

[91] N. Johari, M. Hamady and X. Xu, *A computational study of the effect of stent design on local hemodynamic factors at the carotid artery bifurcation*, Artery Research, 26 (2020), pp. 161–169. doi:10.2991/ARTRES.K.200603.001.

[92] A. D. Kaiser, N. Schiavone, J. Eaton and A. Marsden, *Validation of Immersed Boundary Simulations of Heart Valve Hemodynamics against In Vitro 4D Flow MRI Data*, 2021.

[93] L. Kallekar, C. Viswanath and M. Anand, *Effect of Wall Flexibility on the Deformation during Flow in a Stenosed Coronary Artery*, Fluids, 2 (2017), p. 16. Number: 2 Publisher: Multidisciplinary Digital Publishing Institute. doi:10.3390/fluids2020016.

[94] D. Kamensky, M.-C. Hsu, D. Schillinger, J. A. Evans, A. Aggarwal, Y. Bazilevs, M. S. Sacks and T. J. R. Hughes, *An immersogeometric variational framework for fluid–structure interaction: application to bioprosthetic heart valves*, Computer methods in applied mechanics and engineering, 284 (2015), pp. 1005–1053. doi:10.1016/j.cma.2014.10.040.

[95] K. M. Khanafer, J. L. Bull and R. Berguer, *Fluid–structure interaction of turbulent pulsatile flow within a flexible wall axisymmetric aortic aneurysm model*, European Journal of Mechanics - B/Fluids, 28 (2009), pp. 88–102. doi:10.1016/j.euromechflu.2007.12.003.

[96] W. Kim and H. Choi, *Immersed boundary methods for fluid-structure interaction: A review*, International Journal of Heat and Fluid Flow, 75 (2019), pp. 301–309. doi:10.1016/j.ijheatfluidflow.2019.01.010.

[97] A. R. Kivi, N. Sedaghatizadeh, B. S. Cazzolato, A. C. Zander, A. J. Nelson, R. Roberts-Thomson, A. Yoganathan and M. Arjomandi, *Hemodynamics of a stenosed aortic valve: Effects of the geometry of the sinuses and the positions of the coronary ostia*, International Journal of Mechanical Sciences, 188 (2020), p. 106015. doi:10.1016/j.ijmecsci.2020.106015.

[98] A. G. Kuchumov, V. Vedeneev, V. Samartsev, A. Khairulin and O. Ivanov, *Patient-specific fluid-structure interaction model of bile flow: comparison between 1-way and 2-way algorithms*, Computer Methods in Biomechanics and Biomedical Engineering, 24 (2021), pp. 1693–1717. doi:10.1080/10255842.2021.1910942.

[99] N. Kumar, R. Pai, M. S. Manjunath, A. Ganesha and S. M. Abdul Khader, *Effect of linear and Mooney–Rivlin material model on carotid artery hemodynamics*, Journal

of the Brazilian Society of Mechanical Sciences and Engineering, 43 (2021), p. 395. doi:10.1007/s40430-021-03110-5.

[100] B. R. Kwak, M. Bäck, M.-L. Bochaton-Piallat, G. Caligiuri, M. J. A. P. Daemen, P. F. Davies, I. E. Hoefer, P. Holvoet, H. Jo, R. Krams, S. Lehoux, C. Monaco, S. Steffens, R. Virmani, C. Weber, J. J. Wentzel and P. C. Evans, *Biomechanical factors in atherosclerosis: mechanisms and clinical implications*, European Heart Journal, 35 (2014), pp. 3013–3020, 3020a–3020d. doi:10.1093/eurheartj/ehu353.

[101] M. Lacroix, S. Février, E. Fernández, L. Papeleux, R. Boman and J.-P. Ponthot, *A comparative study of interpolation algorithms on non-matching meshes for PFEM-FEM fluid-structure interactions*, Computers & Mathematics with Applications, 155 (2024), pp. 51–65. doi:10.1016/j.camwa.2023.11.045.

[102] A. Larese, R. Rossi, E. Oñate and S. Idelsohn, *Validation of the particle finite element method (PFEM) for simulation of free surface flows*, Engineering Computations, 25 (2008), pp. 385–425. Publisher: Emerald Group Publishing Limited. doi:10.1108/02644400810874976.

[103] M. Laudato, R. Mosca and M. Mihaescu, *Buckling critical pressures in collapsible tubes relevant for biomedical flows*, Scientific Reports, 13 (2023), p. 9298. Number: 1 Publisher: Nature Publishing Group. doi:10.1038/s41598-023-36513-6.

[104] J. H. Lee and B. E. Griffith, *On the Lagrangian-Eulerian Coupling in the Immersed Finite Element/Difference Method*, Journal of Computational Physics, 457 (2022), p. 111042. doi:10.1016/j.jcp.2022.111042.

[105] J. D. Lemmon and A. P. Yoganathan, *Three-dimensional computational model of left heart diastolic function with fluid-structure interaction*, Journal of Biomechanical Engineering, 122 (2000), pp. 109–117. doi:10.1115/1.429648.

[106] S. J. Lind, B. D. Rogers and P. K. Stansby, *Review of smoothed particle hydrodynamics: towards converged Lagrangian flow modelling*, Proceedings. Mathematical, Physical, and Engineering Sciences, 476 (2020), p. 20190801. doi:10.1098/rspa.2019.0801.

[107] S. N. Lipp, E. E. Niedert, H. L. Cebull, T. C. Diorio, J. L. Ma, S. M. Rothenberger, K. A. Stevens Boster and C. J. Goergen, *Computational Hemodynamic Modeling of Arterial Aneurysms: A Mini-Review*, Frontiers in Physiology, 11 (2020), p. 454. doi:10.3389/fphys.2020.00454.

[108] D. Lopes, R. Agujetas, H. Puga, J. Teixeira, R. Lima, J. P. Alejo and C. Ferrera, *Analysis of finite element and finite volume methods for fluid-structure interaction simulation of blood flow in a real stenosed artery*, International Journal of Mechanical Sciences, 207 (2021), p. 106650. doi:10.1016/j.ijmecsci.2021.106650.

[109] D. Lopes, H. Puga, J. Teixeira and R. Lima, *Blood flow simulations in patient-specific geometries of the carotid artery: A systematic review*, Journal of Biomechanics, 111 (2020), p. 110019. doi:10.1016/j.jbiomech.2020.110019.

[110] MacDonald and J. Ross, *Some Simple Isothermal Equations of State*, Reviews of Modern Physics, 38 (1966), pp. 669–679. Publisher: American Physical Society. doi:10.1103/RevModPhys.38.669.

[111] K. Maganti, V. H. Rigolin, M. E. Sarano and R. O. Bonow, *Valvular Heart Disease: Diagnosis and Management*, Mayo Clinic Proceedings, 85 (2010), pp. 483–500. doi:10.4065/mcp.2009.0706.

[112] A. M. Malek, S. L. Alper and S. Izumo, *Hemodynamic shear stress and its role in atherosclerosis*, JAMA, 282 (1999), pp. 2035–2042. doi:10.1001/jama.282.21.2035.

[113] A. H. Malkawi, R. J. Hinchliffe, Y. Xu, P. J. Holt, I. M. Loftus and M. M. Thompson, *Patient-specific biomechanical profiling in abdominal aortic aneurysm development and rupture*, Journal of Vascular Surgery, 52 (2010), pp. 480–488. doi:10.1016/j.jvs.2010.01.029.

[114] W. Mao, A. Caballero, R. McKay, C. Primiano and W. Sun, *Fully-coupled fluid-structure interaction simulation of the aortic and mitral valves in a realistic 3D left ventricle model*, PloS One, 12 (2017), p. e0184729. doi:10.1371/journal.pone.0184729.

[115] C. Massonet and S. Cescotto, *Mécanique des matériaux*, De Boeck Supérieur, Oct. 1994. Google-Books-ID: awKIStQGKzEC.

[116] A. A. Mercadante and A. Raja, *Anatomy, Arteries*, in StatPearls, StatPearls Publishing, Treasure Island (FL), 2024.

[117] Y. Mesri, H. Niazmand and A. Deyranlou, *Numerical Study on Fluid-Structure Interaction in a Patient-Specific Abdominal Aortic Aneurysm for Evaluating Wall Heterogeneity and Material Model Effects on its Rupture*, Journal of Applied Fluid Mechanics, 10 (2017), pp. 1699–1709. doi:10.29252/jafm.73.245.27678.

[118] C. J. Mills, I. T. Gabe, J. H. Gault, D. T. Mason, J. Ross, E. Braunwald and J. P. Shillingford, *Pressure-flow relationships and vascular impedance in man*, Cardiovascular Research, 4 (1970), pp. 405–417. doi:10.1093/cvr/4.4.405.

[119] A. M. Moerman, S. Korteland, K. Dilba, K. van Gaalen, D. H. J. Poot, A. van Der Lugt, H. J. M. Verhagen, J. J. Wentzel, A. F. W. van Der Steen, F. J. H. Gijsen and K. Van der Heiden, *The Correlation Between Wall Shear Stress and Plaque Composition in Advanced Human Carotid Atherosclerosis*, Frontiers in Bioengineering and Biotechnology, 9 (2022). Publisher: Frontiers. doi:10.3389/fbioe.2021.828577.

[120] H. Mohammadi and K. Mequanint, *Prosthetic aortic heart valves: modeling and design*, Medical Engineering & Physics, 33 (2011), pp. 131–147. doi:10.1016/j.medengphy.2010.09.017.

[121] F. L. Moll, J. T. Powell, G. Fraedrich, F. Verzini, S. Haulon, M. Waltham, J. A. van Herwaarden, P. J. E. Holt, J. W. van Keulen, B. Rantner, F. J. V. Schlösser, F. Setacci, J.-B. Ricco and European Society for Vascular Surgery, *Management of abdominal aortic aneurysms clinical practice guidelines of the European society for vascular surgery*, European Journal of Vascular and Endovascular Surgery: The Official Journal of the European Society for Vascular Surgery, 41 Suppl 1 (2011), pp. S1–S58. doi:10.1016/j.ejvs.2010.09.011.

[122] B. L. Moore and L. P. Dasi, *Coronary Flow Impacts Aortic Leaflet Mechanics and Aortic Sinus Hemodynamics*, Annals of biomedical engineering, 43 (2015), pp. 2231–2241. doi:10.1007/s10439-015-1260-4.

[123] U. Morbiducci, D. Gallo, D. Massai, F. Consolo, R. Ponzini, L. Antiga, C. Bignardi, M. A. Deriu and A. Redaelli, *Outflow conditions for image-based hemodynamic models of the carotid bifurcation: implications for indicators of abnormal flow*, Journal of Biomechanical Engineering, 132 (2010), p. 091005. doi:10.1115/1.4001886.

[124] J. P. Morris, *A Study of the Stability Properties of Smooth Particle Hydrodynamics*, Publications of the Astronomical Society of Australia, 13 (1996), pp. 97–102. doi:10.1017/S1323358000020610.

[125] E. Nader, S. Skinner, M. Romana, R. Fort, N. Lemonne, N. Guillot, A. Gauthier, S. Antoine-Jonville, C. Renoux, M.-D. Hardy-Dessources, E. Stauffer, P. Joly, Y. Bertrand and P. Connes, *Blood Rheology: Key Parameters, Impact on Blood Flow, Role in Sickle Cell Disease and Effects of Exercise*, Frontiers in Physiology, 10 (2019). Publisher: Frontiers. doi:10.3389/fphys.2019.01329.

[126] P. Nagpal, M. D. Agrawal, S. S. Saboo, S. Hedgire, S. Priya and M. L. Steigner, *Imaging of the aortic root on high-pitch non-gated and ECG-gated CT: awareness is the key!*, Insights into Imaging, 11 (2020), p. 51. doi:10.1186/s13244-020-00855-w.

[127] P. Nigro, J.-i. Abe and B. C. Berk, *Flow Shear Stress and Atherosclerosis: A Matter of Site Specificity*, Antioxidants & Redox Signaling, 15 (2011), pp. 1405–1414. doi:10.1089/ars.2010.3679.

[128] S. Nobari, R. Mongrain, R. Leask and R. Cartier, *The effect of aortic wall and aortic leaflet stiffening on coronary hemodynamic: a fluid-structure interaction study*, Medical & Biological Engineering & Computing, 51 (2013), pp. 923–936. doi:10.1007/s11517-013-1066-1.

[129] C. W. Ong, I. Wee, N. Syn, S. Ng, H. L. Leo, A. M. Richards and A. M. T. L. Choong, *Computational Fluid Dynamics Modeling of Hemodynamic Parameters in the Human Diseased Aorta: A Systematic Review*, Annals of Vascular Surgery, 63 (2020), pp. 336–381. doi:10.1016/j.avsg.2019.04.032.

[130] C. M. Otto, J. Kuusisto, D. D. Reichenbach, A. M. Gown and K. D. O'Brien, *Characterization of the early lesion of 'degenerative' valvular aortic stenosis. Histological and immunohistochemical studies*, Circulation, 90 (1994), pp. 844–853. doi:10.1161/01.cir.90.2.844.

[131] B. Owen, N. Bojdo, A. Jivkov, B. Keavney and A. Revell, *Structural modelling of the cardiovascular system*, Biomechanics and Modeling in Mechanobiology, 17 (2018), pp. 1217–1242. doi:10.1007/s10237-018-1024-9.

[132] R. Pahwa and I. Jialal, *Atherosclerosis*, in StatPearls, StatPearls Publishing, Treasure Island (FL), 2024.

[133] D. V. Parshin, A. I. Lipovka, A. S. Yunoshev, K. S. Ovsyannikov, A. V. Dubovoy and A. P. Chupakhin, *On the optimal choice of a hyperelastic model of ruptured and unruptured cerebral aneurysm*, Scientific Reports, 9 (2019), p. 15865. doi:10.1038/s41598-019-52229-y.

[134] C. S. Peskin, *Numerical analysis of blood flow in the heart*, Journal of Computational Physics, 25 (1977), pp. 220–252. doi:10.1016/0021-9991(77)90100-0.

[135] J.-P. Ponthot, *Metafor*, http://metafor.ltas.ulg.ac.be/dokuwiki/ (Accessed: 2024-02-24).

[136] J.-P. Ponthot, *Traitement unifié de la Mécanique des Milieux Continus Solides en Grandes Transformations par la Méthode des Eléments Finis*, PhD thesis, 1995. Publisher: Collection des publications de la faculté des Sciences Appliquées N° 159, Université de Liège.

[137] J.-P. Ponthot, R. Boman, P.-P. Jeunechamps, L. Papeleux and G. Deliege, *An Implicit Erosion Algorithm for the Numerical Simulation of Metallic and Composite Materials Submitted to High Strain Rates*, Proceedings of the Indian National Science Academy, 79 (2013), p. 519. doi:10.16943/ptinsa/2013/v79i4/47987.

[138] G. A. M. Pop, D. J. Duncker, M. Gardien, P. Vranckx, S. Versluis, D. Hasan and C. J. Slager, *The clinical significance of whole blood viscosity in (cardio)vascular medicine*, Netherlands Heart Journal: Monthly Journal of the Netherlands Society of Cardiology and the Netherlands Heart Foundation, 10 (2002), pp. 512–516.

[139] M. L. Raghavan and D. A. Vorp, *Toward a biomechanical tool to evaluate rupture potential of abdominal aortic aneurysm: identification of a finite strain constitutive model and evaluation of its applicability*, Journal of Biomechanics, 33 (2000), pp. 475–482. doi:10.1016/s0021-9290(99)00201-8.

[140] S. Rahmani, A. Jarrahi, B. Saed, M. Navidbakhsh, H. Farjpour and M. Alizadeh, *Three-dimensional modeling of Marfan syndrome with elastic and hyperelastic materials assumptions using fluid-structure interaction*, Bio-Medical Materials and Engineering, 30 (2019), pp. 255–266. doi:10.3233/BME-191049.

[141] S. S. Raut, A. Jana, V. De Oliveira, S. C. Muluk and E. A. Finol, *The Importance of Patient-Specific Regionally Varying Wall Thickness in Abdominal Aortic Aneurysm Biomechanics*, Journal of Biomechanical Engineering, 135 (2013), pp. 0810101–08101010. doi:10.1115/1.4024578.

[142] D. Reed, C. Reed, G. Stemmermann and T. Hayashi, *Are aortic aneurysms caused by atherosclerosis?*, Circulation, 85 (1992), pp. 205–211. doi:10.1161/01.cir.85.1.205.

[143] P. Rissland, J. Ricotta, D. Bluestein, Y. Alemu and S. Einav, *Abdominal Aortic Aneurysm Risk of Rupture: Patient-Specific FSI Simulations Using Anisotropic Model*, (2009). Accepted: 2017-05-09T00:31:47Z Publisher: The American Society of Mechanical Engineers (ASME). doi:10.1115/1.3005200.

[144] A. A. Rostam-Alilou, H. R. Jarrah, A. Zolfagharian and M. Bodaghi, *Fluid-structure interaction (FSI) simulation for studying the impact of atherosclerosis on hemodynamics, arterial tissue remodeling, and initiation risk of intracranial aneurysms*, Biomechanics and Modeling in Mechanobiology, 21 (2022), pp. 1393–1406. doi:10.1007/s10237-022-01597-y.

[145] M. S. Sacks and A. P. Yoganathan, *Heart valve function: a biomechanical perspective*, Philosophical Transactions of the Royal Society B: Biological Sciences, 362 (2007), pp. 1369–1391. doi:10.1098/rstb.2007.2122.

[146] F. Sadeghpour, N. Fatouraee and M. Navidbakhsh, *Haemodynamic of blood flow through stenotic aortic valve*, Journal of Medical Engineering & Technology, 41 (2017), pp. 108–114. doi:10.1080/03091902.2016.1226439.

[147] M. Saeedi, A. Shamloo and A. Mohammadi, *Fluid-Structure Interaction Simulation of Blood Flow and Cerebral Aneurysm: Effect of Partly Blocked Vessel*, Journal of Vascular Research, 56 (2019), pp. 296–307. doi:10.1159/000503786.

[148] N. Saikrishnan, C.-H. Yap, N. C. Milligan, N. V. Vasilyev and A. P. Yoganathan, *In vitro characterization of bicuspid aortic valve hemodynamics using particle image velocimetry*, Annals of Biomedical Engineering, 40 (2012), pp. 1760–1775. doi:10.1007/s10439-012-0527-2.

[149] N. Sakalihasan, R. Limet and O. D. Defawe, *Abdominal aortic aneurysm*, Lancet (London, England), 365 (2005), pp. 1577–1589. doi:10.1016/S0140-6736(05)66459-8.

[150] H. E. Salman, B. Ramazanli, M. M. Yavuz and H. C. Yalcin, *Biomechanical Investigation of Disturbed Hemodynamics-Induced Tissue Degeneration in Abdominal Aortic Aneurysms Using Computational and Experimental Techniques*, Frontiers in Bioengineering and Biotechnology, 7 (2019), p. 111. doi:10.3389/fbioe.2019.00111.

[151] P. Sarantides, A. Raptis, D. Mathioulakis, K. Moulakakis, J. Kakisis and C. Manopoulos, *Computational Study of Abdominal Aortic Aneurysm Walls Accounting for Patient-Specific Non-Uniform Intraluminal Thrombus Thickness and Distinct Material Models: A Pre- and Post-Rupture Case*, Bioengineering, 11 (2024), p. 144. Number: 2 Publisher: Multidisciplinary Digital Publishing Institute. doi:10.3390/bioengineering11020144.

[152] R. Savabi, M. Nabaei, S. Farajollahi and N. Fatouraee, *Fluid structure interaction modeling of aortic arch and carotid bifurcation as the location of baroreceptors*, International Journal of Mechanical Sciences, 165 (2020), p. 105222. doi:10.1016/j.ijmecsci.2019.105222.

[153] H. Schmid-Schönbein and R. E. Wells, *Rheological properties of human erythrocytes and their influence upon the "anomalous" viscosity of blood*, Ergebnisse Der Physiologie, Biologischen Chemie Und Experimentellen Pharmakologie, 63 (1971), pp. 146–219. doi:10.1007/BFb0047743.

[154] C. M. Scotti, J. Jimenez, S. C. Muluk and E. A. Finol, *Wall stress and flow dynamics in abdominal aortic aneurysms: finite element analysis vs. fluid-structure interaction*, Computer Methods in Biomechanics and Biomedical Engineering, 11 (2008), pp. 301–322. doi:10.1080/10255840701827412.

[155] C. M. Scotti, A. D. Shkolnik, S. C. Muluk and E. A. Finol, *Fluid-structure interaction in abdominal aortic aneurysms: effects of asymmetry and wall thickness*, Biomedical Engineering Online, 4 (2005), p. 64. doi:10.1186/1475-925X-4-64.

[156] E. Segarra, M. Cevallos and J. David, *Comparative analysis between native, stenotic and mechanical aortic valves using FSI (Fluid Structure Interaction) module*, 2017.

[157] S. Shahriari, L. Kadem, B. Rogers and I. Hassan, *Smoothed particle hydrodynamics method applied to pulsatile flow inside a rigid two-dimensional model of left heart cavity*, International Journal for Numerical Methods in Biomedical Engineering, 28 (2012), pp. 1121–1143. doi:10.1002/cnm.2482.

[158] S. Shahriari, H. Maleki, I. Hassan and L. Kadem, *Evaluation of shear stress accumulation on blood components in normal and dysfunctional bileaflet mechanical heart valves using smoothed particle hydrodynamics*, Journal of Biomechanics, 45 (2012), pp. 2637–2644. doi:10.1016/j.jbiomech.2012.08.009.

[159] H. Shahzad, X. Wang, A. Ghaffari, K. Iqbal, M. B. Hafeez, M. Krawczuk and W. Wojnicz, *Fluid structure interaction study of non-Newtonian Casson fluid in a bifurcated channel having stenosis with elastic walls*, Scientific Reports, 12 (2022), p. 12219. Number: 1 Publisher: Nature Publishing Group. doi:10.1038/s41598-022-16213-3.

[160] N. A. Shirwany and M.-h. Zou, *Arterial stiffness: a brief review*, Acta Pharmacologica Sinica, 31 (2010), pp. 1267–1276. doi:10.1038/aps.2010.123.

[161] E. Sigala, M. Kelesi, D. Terentes-Printzios, G. Vasilopoulos, T. Kapadohos, D. Papageorgiou, A. Tzatzou, C. Vlachopoulos and A. Stavropoulou, *Surgical Aortic Valve Replacement in Patients Aged 50 to 70 Years: Mechanical or Bioprosthetic Valve? A Systematic Review*, Healthcare, 11 (2023), p. 1771. doi:10.3390/healthcare11121771.

[162] B. R. Simon, M. V. Kaufmann, M. A. McAfee and A. L. Baldwin, *Finite element models for arterial wall mechanics*, Journal of Biomechanical Engineering, 115 (1993), pp. 489–496. doi:10.1115/1.2895529.

[163] F. G. Simsek and Y. W. Kwon, *Investigation of material modeling in fluid–structure interaction analysis of an idealized three-layered abdominal aorta: aneurysm initiation and fully developed aneurysms*, Journal of Biological Physics, 41 (2015), pp. 173–201. doi:10.1007/s10867-014-9372-x.

[164] T. P. Singh, J. V. Moxon, T. C. Gasser and J. Golledge, *Systematic Review and Meta-Analysis of Peak Wall Stress and Peak Wall Rupture Index in Ruptured and Asymptomatic Intact Abdominal Aortic Aneurysms*, Journal of the American Heart Association: Cardiovascular and Cerebrovascular Disease, 10 (2021), p. e019772. doi:10.1161/JAHA.120.019772.

[165] S. C. Siu and C. K. Silversides, *Bicuspid Aortic Valve Disease*, Journal of the American College of Cardiology, 55 (2010), pp. 2789–2800. doi:10.1016/j.jacc.2009.12.068.

[166] T. Sochi, *Non-Newtonian Rheology in Blood Circulation*, arXiv: Fluid Dynamics, (2013).

[167] M. Soleimani, R. Deo, B. Hudobivnik, R. Poyanmehr, A. Haverich and P. Wriggers, *Mathematical modeling and numerical simulation of arterial dissection based on a novel surgeon's view*, Biomechanics and Modeling in Mechanobiology, 22 (2023), pp. 2097–2116. doi:10.1007/s10237-023-01753-y.

[168] K. R. Stenmark, M. E. Yeager, K. C. El Kasmi, E. Nozik-Grayck, E. V. Gerasimovskaya, M. Li, S. R. Riddle and M. G. Frid, *The adventitia: essential regulator of vascular wall structure and function*, Annual Review of Physiology, 75 (2013), pp. 23–47. doi:10.1146/annurev-physiol-030212-183802.

[169] Y. G. Stergiou, A. G. Kanaris, A. A. Mouza and S. V. Paras, *Fluid-Structure Interaction in Abdominal Aortic Aneurysms: Effect of Haematocrit*, Fluids, 4 (2019), p. 11. Number: 1 Publisher: Multidisciplinary Digital Publishing Institute. doi:10.3390/fluids4010011.

[170] K. W. Stock, S. G. Wetzel, P. A. Lyrer and E. W. Radü, *Quantification of blood flow in the middle cerebral artery with phase-contrast MR imaging*, European Radiology, 10 (2000), pp. 1795–1800. doi:10.1007/s003300000378.

[171] S.-Y. Sun, H. Zhang, W. Fang, X. Chen, B. Li and X.-Q. Feng, *Chapter Three - Bio-chemo-mechanical coupling models of soft biological materials: A review*, in Advances in Applied Mechanics, S. P. A. Bordas, ed., vol. 55, Elsevier, Jan. 2022, pp. 309–392.

[172] W.-K. Sun, B. B. Yin, L.-W. Zhang and K. M. Liew, *Blood pressure-driven rupture of blood vessels*, Journal of the Mechanics and Physics of Solids, 174 (2023), p. 105274. doi:10.1016/j.jmps.2023.105274.

[173] F. Syed, S. Khan and M. Toma, *Modeling Dynamics of the Cardiovascular System Using Fluid-Structure Interaction Methods*, Biology, 12 (2023), p. 1026. Number: 7 Publisher: Multidisciplinary Digital Publishing Institute. doi:10.3390/biology12071026.

[174] C. A. Taylor, C. P. Cheng, L. A. Espinosa, B. T. Tang, D. Parker and R. J. Herfkens, *In vivo quantification of blood flow and wall shear stress in the human abdominal aorta during lower limb exercise*, Annals of Biomedical Engineering, 30 (2002), pp. 402–408. doi:10.1114/1.1476016.

[175] A. Teutelink, E. Cancrinus, D. van de Heuvel, F. Moll and J.-P. de Vries, *Preliminary intraobserver and interobserver variability in wall stress and rupture risk assessment of abdominal aortic aneurysms using a semiautomatic finite element model*, Journal of Vascular Surgery, 55 (2012), pp. 326–330. doi:10.1016/j.jvs.2011.08.012.

[176] T. E. Tezduyar, S. Mittal, S. E. Ray and R. Shih, *Incompressible flow computations with stabilized bilinear and linear equal-order-interpolation velocity-pressure elements*, Computer Methods in Applied Mechanics and Engineering, 95 (1992), pp. 221–242. doi:10.1016/0045-7825(92)90141-6.

[177] The CGAL Project, *CGAL User and Reference Manual*, CGAL Editorial Board, 5.6 ed., 2023.

[178] M. Thieret, *Biology and Mechanics of Blood Flows - Part I: Biology*, (2008). doi:10.1007/978-0-387-74847-4.

[179] D. Thomas, M. L. Cerquaglia, R. Boman, T. D. Economon, J. J. Alonso, G. Dimitriadis and V. E. Terrapon, *CUPyDO - An integrated Python environment for coupled fluid-structure simulations*, Advances in Engineering Software, 128 (2019), pp. 69–85. doi:10.1016/j.advengsoft.2018.05.007.

[180] B. G. Thompson, R. D. Brown, S. Amin-Hanjani, J. P. Broderick, K. M. Cockroft, E. S. Connolly, G. R. Duckwiler, C. C. Harris, V. J. Howard, S. C. C. Johnston, P. M. Meyers, A. Molyneux, C. S. Ogilvy, A. J. Ringer and J. Torner, *Guidelines for the Management of Patients With Unruptured Intracranial Aneurysms: A Guideline for Healthcare Professionals From the American Heart Association/American Stroke Association*, Stroke, 46 (2015), pp. 2368–2400. doi:10.1161/STR.0000000000000070.

[181] A. Tijsseling and A. Anderson, *A. Isebree Moens and D.J. Korteweg: On the speed of propagation of waves in elastic tubes*, Oct. 2012.

[182] M. Toma, R. Chan-Akeley, J. Arias, G. D. Kurgansky and W. Mao, *Fluid-Structure Interaction Analyses of Biological Systems Using Smoothed-Particle Hydrodynamics*, Biology, 10 (2021), p. 185. doi:10.3390/biology10030185.

[183] M. Toma, A. Krdey, S. Takagi and M. Oshima, *Strongly Coupled Fluid-Structure Interaction Cardiovascular Analysis with the Effect of Peripheral Network*, SEISAN-KENKYU, 63 (2011), pp. 339–344.

[184] M. Topalovic, A. Nikolic, V. Milovanovic, S. Vulovic and M. Ivanovic, *Smoothed particle hydrodynamics for blood flow analysis: development of particle lifecycle algorithm*, Computational Particle Mechanics, 9 (2022), pp. 1119–1135. doi:10.1007/s40571-021-00454-6.

[185] V. Tuncay, N. Prakken, P. M. A. van Ooijen, R. P. J. Budde, T. Leiner and M. Oudkerk, *Semiautomatic, Quantitative Measurement of Aortic Valve Area Using CTA: Validation and Comparison with Transthoracic Echocardiography*, BioMed Research International, 2015 (2015), p. 648283. doi:10.1155/2015/648283.

[186] United Kingdom EVAR Trial Investigators, R. M. Greenhalgh, L. C. Brown, J. T. Powell, S. G. Thompson, D. Epstein and M. J. Sculpher, *Endovascular versus open repair of abdominal aortic aneurysm*, The New England Journal of Medicine, 362 (2010), pp. 1863–1871. doi:10.1056/NEJMoa0909305.

[187] A. Updegrove, N. M. Wilson, J. Merkow, H. Lan, A. L. Marsden and S. C. Shadden, *SimVascular: An Open Source Pipeline for Cardiovascular Simulation*, Annals of Biomedical Engineering, 45 (2017), pp. 525–541. doi:10.1007/s10439-016-1762-8.

[188] A. Valencia, P. Burdiles, M. Ignat, J. Mura, E. Bravo, R. Rivera and J. Sordo, *Fluid structural analysis of human cerebral aneurysm using their own wall mechanical properties*, Computational and Mathematical Methods in Medicine, 2013 (2013), p. 293128. doi:10.1155/2013/293128.

[189] J. van Gijn and G. J. Rinkel, *Subarachnoid haemorrhage: diagnosis, causes and management*, Brain: A Journal of Neurology, 124 (2001), pp. 249–278. doi:10.1093/brain/124.2.249.

[190] J. P. Vande Geest, D. H. J. Wang, S. R. Wisniewski, M. S. Makaroun and D. A. Vorp, *Towards a noninvasive method for determination of patient-specific wall strength distribution in abdominal aortic aneurysms*, Annals of Biomedical Engineering, 34 (2006), pp. 1098–1106. doi:10.1007/s10439-006-9132-6.

[191] Y. Vassilevski, S. Simakov, V. Salamatova, Y. Ivanov and T. Dobroserdova, *Vessel Wall Models for Simulation of Atherosclerotic Vascular Networks*, Mathematical Modelling of Natural Phenomena, 6 (2011), pp. 82–99. Number: 7 Publisher: EDP Sciences. doi:10.1051/mmnp:20116707.

[192] A. K. Venkatasubramaniam, M. J. Fagan, T. Mehta, K. J. Mylankal, B. Ray, G. Kuhan, I. C. Chetter and P. T. McCollum, *A comparative study of aortic wall stress using finite element analysis for ruptured and non-ruptured abdominal aortic aneurysms*, European Journal of Vascular and Endovascular Surgery: The Official Journal of the European Society for Vascular Surgery, 28 (2004), pp. 168–176. doi:10.1016/j.ejvs.2004.03.029.

[193] C. Vlachopoulos, M. O'Rourke and W. W. Nichols, *McDonald's Blood Flow in Arteries: Theoretical, Experimental and Clinical Principles*, CRC Press, London, 6 ed., Dec. 2012. doi:10.1201/b13568.

[194] D. A. Vorp, *Biomechanics of abdominal aortic aneurysm*, Journal of biomechanics, 40 (2007), pp. 1887–1902. doi:10.1016/j.jbiomech.2006.09.003.

[195] X. Wang, M. H. Ghayesh, A. Kotousov, A. C. Zander, M. Amabili, J. A. Dawson and P. J. Psaltis, *Biomechanics of abdominal aortic aneurysm in the framework of Windkessel effect and fully-developed inflow velocity via two-way non-linear FSI*, International Journal of Non-Linear Mechanics, 157 (2023), p. 104517. doi:10.1016/j.ijnonlinmec.2023.104517.

[196] P. N. Watton, A. Selimovic, N. B. Raberger, P. Huang, G. A. Holzapfel and Y. Ventikos, *Modelling evolution and the evolving mechanical environment of saccular cerebral aneurysms*, Biomechanics and Modeling in Mechanobiology, 10 (2011), pp. 109–132. doi:10.1007/s10237-010-0221-y.

[197] K. K. L. Wong, P. Thavornpattanapong, S. C. P. Cheung and J. Tu, *Numerical stability of partitioned approach in fluid-structure interaction for a deformable thin-walled*

vessel, Computational and Mathematical Methods in Medicine, 2013 (2013), p. 638519. doi:10.1155/2013/638519.

[198] World Health Organization, *WHO Mortality Database*, https://www.who.int/data/data-collection-tools/who-mortality-database (Accessed: 2024-02-12).

[199] World Heart Federation, *World Heart Report 2023: Confronting the World's Number One Killer.*, 2023, https://world-heart-federation.org/wp-content/uploads/World-Heart-Report-2023.pdf.

[200] J. Wu, G. Liu, W. Huang, D. N. Ghista and K. K. L. Wong, *Transient blood flow in elastic coronary arteries with varying degrees of stenosis and dilatations: CFD modelling and parametric study*, Computer Methods in Biomechanics and Biomedical Engineering, 18 (2015), pp. 1835–1845. doi:10.1080/10255842.2014.976812.

[201] M. Xenos, S. H. Rambhia, Y. Alemu, S. Einav, N. Labropoulos, A. Tassiopoulos, J. J. Ricotta and D. Bluestein, *Patient-based abdominal aortic aneurysm rupture risk prediction with fluid structure interaction modeling*, Annals of Biomedical Engineering, 38 (2010), pp. 3323–3337. doi:10.1007/s10439-010-0094-3.

[202] J. Xiang, S. K. Natarajan, M. Tremmel, D. Ma, J. Mocco, L. N. Hopkins, A. H. Siddiqui, E. I. Levy and H. Meng, *Hemodynamic-morphologic discriminants for intracranial aneurysm rupture*, Stroke, 42 (2011), pp. 144–152. doi:10.1161/STROKEAHA.110.592923.

[203] J. Xiang, V. M. Tutino, K. V. Snyder and H. Meng, *CFD: computational fluid dynamics or confounding factor dissemination? The role of hemodynamics in intracranial aneurysm rupture risk assessment*, AJNR. American journal of neuroradiology, 35 (2014), pp. 1849–1857. doi:10.3174/ajnr.A3710.

[204] M. H. Yacoub and L. H. Cohn, *Novel approaches to cardiac valve repair: from structure to function: Part II*, Circulation, 109 (2004), pp. 1064–1072. doi:10.1161/01.CIR.0000115634.66549.4D.

[205] A. P. Yoganathan, Z. He and S. Casey Jones, *Fluid mechanics of heart valves*, Annual Review of Biomedical Engineering, 6 (2004), pp. 331–362. doi:10.1146/annurev.bioeng.6.040803.140111.

[206] N. K. Yoon, S. McNally, P. Taussky and M. S. Park, *Imaging of cerebral aneurysms: a clinical perspective*, Neurovascular Imaging, 2 (2016), p. 6. doi:10.1186/s40809-016-0016-3.

[207] M. Zakaria, F. Ismail, M. Tamagawa, A. Abdul Azi, S. Wiriadidjaya, A. Basri and K. Ahmad, *Computational fluid dynamics study of blood flow in aorta using OpenFOAM*, Journal of Advanced Research in Fluid Mechanics and Thermal Sciences, 43 (2018), pp. 81–89.

[208] X. Zhang, K. Krabbenhoft, D. M. Pedroso, A. V. Lyamin, D. Sheng, M. V. da Silva and D. Wang, *Particle finite element analysis of large deformation and granular flow problems*, Computers and Geotechnics, 54 (2013), pp. 133–142. doi:10.1016/j.compgeo.2013.07.001.

[209] M. Zhou, Y. Yu, R. Chen, X. Liu, Y. Hu, Z. Ma, L. Gao, W. Jian and L. Wang, *Wall shear stress and its role in atherosclerosis*, Frontiers in Cardiovascular Medicine, 10 (2023), p. 1083547. doi:10.3389/fcvm.2023.1083547.